Determination of the Gravity Field of Titan

Simulated Measurements and Estimation Prospects with Cassini Tracking Data

Alfonso Mateo Aguaron

September 19, 2022

TU Delft

Image credit: NASA/JPL-Caltech/Space Science Institute

Determination of the Gravity Field of Titan

Simulated Measurements and
Estimation Prospects with Cassini Tracking Data

Alfonso Mateo Aguaron

To obtain the degree of Master of Science
at the Delft University of Technology.

September 19, 2022.

TU Delft

Preface

First and foremost, I want to give special thanks to my supervisor Wouter van der Wal. This study has represented a real journey for me, full of pitfalls and roads leading to nowhere, but also filled with those tiny discoveries, after each step, which make research so rewarding. As I move forward to pursue a PhD, I will dive deeper, at least for some more time, into the academic world. This has been the longest and, for many reasons, most complex research project in which I have ever been involved, and I truly believe that I could not have wished for better guidance and assistance. Apart from his expertise, great ideas and suggestions in the topic relevant for this MSc thesis, he has given me a lot of lessons about how to properly do research and present findings. This knowledge is invaluable to me and gives me confidence for the new stage I am beginning. I am really grateful for his encouragement when things were frustrating and progress seemed to halt. I will miss our weekly meetings.

I would also like to thank Sander Goossens at NASA GSFC and Bob van Noort at TU Delft for their continuous help and advice regarding the GEODYN setup and the Cassini Doppler data. I want to especially thank them for their time spent in our regular meetings where we discussed results and they gave me insight as to whether I was going in the right direction. Without their contributions, prior to and during this research, this work would have not been possible. I also want to thank Sander for all the assistance he gave me for feeding simulated data into GEODYN, eliminating the relativistic corrections and more. I am also grateful for the advice and ideas provided by Dominic Dirkx and Marie Fayolle-Chambe from the Astrodynamics and Space Missions department at our faculty. Credit should be given as well to Pieter Visser, chairholder of that department, who helped me to find the right software I needed to preprocess the simulated data for the GEODYN setup. Last but not least, I would like to thank my family for all their love and support and María for encouraging me to apply for this thrilling master's studies program.

Contents

Preface iii

List of Figures vii

List of Tables ix

List of Abbreviations x

Abstract xi

1 Introduction 1
- 1.1 The Titan gravity determination problem . . . 1
- 1.2 Doppler measurements . . . 6
- 1.3 Research questions . . . 9

2 Estimation with real data 11
- 2.1 Issues with the estimation setup with GEODYN . . . 11
- 2.2 Inequality constraints . . . 15
- 2.3 Tests with inequality constraints . . . 16
- 2.4 Effect of empirical accelerations . . . 17
- 2.5 Effect of tidal lag estimation . . . 19

3 Verification with simulated data 22
- 3.1 Generation of simulated data . . . 22
  - 3.1.1 Simulated flybys . . . 22
  - 3.1.2 Magnitude characterisation of relativistic effects . . . 26
  - 3.1.3 Simulated gravity fields . . . 29
- 3.2 Verification tests . . . 32
  - 3.2.1 Empirical accelerations and measurement biases . . . 32
  - 3.2.2 Simulated fields and Titan reference frame . . . 36
  - 3.2.3 Correlation between parameters . . . 38
  - 3.2.4 Atmospheric effects . . . 40
  - 3.2.5 Propagation of the position of Titan . . . 41
  - 3.2.6 Relativistic effects . . . 42
  - 3.2.7 Ephemeris . . . 47
  - 3.2.8 Integration of the orbit of Cassini . . . 48

4 Simulated estimation with Tudat 55
- 4.1 Doppler measurement partials . . . 55
- 4.2 Noiseless estimation . . . 57
- 4.3 Estimation with noise . . . 60
- 4.4 Impact of unaccounted relativistic effects . . . 64
- 4.5 Effects of unaccounted timing bias . . . 66
- 4.6 Estimation prospects with real data . . . 69

5 Conclusion 72

Bibliography 75

List of Figures

1 Schematic of a three-way Doppler observation of a spacecraft's relative velocity. Figure taken from Weischede et al. (1999). 7

2 Doppler residuals for flyby T074 for **(a)** the case with null Love number k_2 and **(b)** unconstrained k_2. The shape and magnitude (9.431 mHz vs. 9.094 mHz RMS respectively) of the residuals is almost identical in both cases despite the large difference in estimated coefficients. Closest approach takes place at 16:04, February 18, 2011. 13

3 Correlation matrix for relevant gravity field parameters when **(a)** the Love number k_2 is not estimated and **(b)** k_2 is estimated. 14

4 Doppler residuals for flyby T074 for **(a)** the case with null Love number k_2 and **(b)** unconstrained k_2. The shape and magnitude (151.7 mHz vs. 151.8 mHz RMS respectively) of the residuals is almost identical in both cases despite the large difference in estimated coefficients. Closest approach takes place at 16:04, February 18, 2011. 19

5 Correlation matrix for relevant gravity field parameters when the empirical accelerations are removed and **(a)** the Love number k_2 is not estimated and **(b)** k_2 is estimated. 20

6 Ground tracks of the different simulated Cassini flybys with the point of closest approach and direction of the orbit. Twelve-hour long arcs are considered. The initial states were retrieved from the Cassini SPICE ephemeris and then the perturbed orbits propagated. 23

7 Received two-way Doppler shift signal for the different simulated flybys. 25

8 Comparative magnitude of different relativistic effects on one-way Doppler observables, computed as the difference between the nominal curve with all the effects and the signal without the respective ones. The line corresponding to the overall general relativistic effect is behind the drift curve. 26

9 Comparative magnitude of different relativistic effects on one-way Doppler observables, computed as the difference between the nominal curve with all the effects and bodies and the signal without the respective body. 27

10 Comparative magnitude of different relativistic effects on two-way Doppler observables, computed as the difference between the nominal curve with all the effects and the signal without the respective ones. 27

11 Comparative magnitude of different relativistic effects on two-way Doppler observables, computed as the difference between the nominal curve with all the effects and bodies and the signal without the respective body. 28

12 Difference in relative velocity and two-way Doppler data for different simulated gravity field coefficients and flybys T011 and T022. Changes in relative velocity and Doppler show the same curve shapes but with opposite signs. 30

13 Difference in two-way Doppler data for different simulated gravity field coefficients and flybys. 31

14 Doppler residuals for flyby T110 for the cases with empirical accelerations and **(a)** with measurement biases and **(b)** without them. The RMS of the residuals in this flyby for each case are 85.39 mHz vs. 724.5 mHz respectively. 34

15 Doppler residuals for flyby T110 for the cases without empirical accelerations and **(a)** with measurement biases and **(b)** without them. The RMS of the residuals in this flyby for each case are 179.8 mHz vs. 746.5 mHz respectively. 35

16 Correlation matrix for relevant gravity field parameters when estimating with the simulated null field and **(a)** with empirical accelerations and simple measurement biases and **(b)** without them. Differences between the two are small, but some correlations change sign. . . . 39
17 Doppler residuals for flyby T110 for the cases with **(a)** simulated data accounting for special relativity and **(b)** the data without relativistic effects (936.0 mHz vs. 335.1 mHz RMS respectively). All relativistic effects were stripped from the estimation processing chain. . . . 44
18 Doppler residuals for flyby T110 for the cases with **(a)** simulated data accounting for special relativity and **(b)** the data without relativistic effects (936.0 mHz vs. 335.1 mHz RMS respectively). Only Titan's gravitational parameter was estimated. All relativistic effects were stripped from the estimation processing chain. . . . 45
19 Doppler residuals for flyby T068 for the cases with **(a)** simulated data accounting for special relativity and **(b)** the data without relativistic effects (33.35 mHz vs. 129.0 mHz RMS respectively). Only Titan's gravitational parameter was estimated. All relativistic effects were stripped from the estimation processing chain. . . . 46
20 Difference in state (norm of position and velocity difference) between the Titan and Saturn ephemerides used in GEODYN and the ones extracted for the simulated data. The plots just show numerical rounding error. . . . 48
21 Norm of the difference in position and velocity between the orbit of flyby T033 computed by GEODYN and the one by Tudat for the simulated data. . . . 49
22 Norm and normalised components in the J2000 reference frame (Feissel & Mignard, 1998) of the difference in acceleration between the orbit of flyby T033 computed by GEODYN and the one by Tudat for the simulated data. . . . 50
23 Norm of the difference in position and velocity between the orbit of flyby T033 computed by GEODYN and the one by Tudat for the simulated data. The spherical harmonics of Saturn were omitted in both propagations of the orbit. . . . 51
24 Norm and normalised components in the J2000 reference frame of the difference in acceleration between the orbit of flyby T033 computed by GEODYN and the one by Tudat for the simulated data. The spherical harmonics of Saturn were omitted in both propagations of the orbit. . . . 51
25 Norm of the difference in position and velocity between the orbit of flyby T033 computed by GEODYN and the one by Tudat for the simulated data. The spherical harmonics of Saturn were omitted in both propagations of the orbit and the spherical harmonics of Titan were estimated by GEODYN. . . . 53
26 Norm and normalised components in the J2000 reference frame of the difference in acceleration between the orbit of flyby T033 computed by GEODYN and the one by Tudat for the simulated data. The spherical harmonics of Saturn were omitted in both propagations of the orbit and the spherical harmonics of Titan were estimated by GEODYN. . . . 53
27 Residual plots of flybys T022 and T074 from the noiseless test run. The different colours represent the combinations of transmitter and receiver antennae. In this case the residuals are dominated by numerical rounding error. . . . 58
28 Correlation matrix for the different Titan gravity field coefficients obtained in the noiseless test run. . . . 59
29 Residual plots of flybys T022 and T074 from the simulated estimation with Gaussian noise of constant 5 mHz standard deviation. The different colours represent the combinations of transmitter and receiver antennae. . . . 61
30 Correlation matrix for the different Titan gravity field coefficients obtained in the degree and order five simulated estimation analogous to the one performed by Durante et al. (2019). . . . 64
31 Residual plots of flybys T022 and T074 from the test where the relativistic effects were not accounted for and a point-mass gravity was considered for Titan. . . . 65

32 Correlation matrix for the different Titan gravity field coefficients obtained in the test where the relativistic effects were not accounted for and a point-mass gravity was considered for Titan. 66
33 Residual plots of flybys T022 and T074 from the test with a +1 s error in receiver timestamps, 5 mHz noise and a simulated point-mass gravity for Titan. 67
34 Correlation matrix for the different Titan gravity field coefficients obtained in the test with a +1 s error in receiver timestamps, 5 mHz noise and a simulated point-mass gravity for Titan. 68
35 Residual plots of flybys T022 and T074 when feeding the real data to the estimation setup and performing one iteration, so the orbit is not updated, with the point-mass gravity of Titan as initial guess. Timing bias of -50 s was applied to manually reduce the signal in T099. 70

List of Tables

1 Maximum magnitudes of the accelerations in the Solar System barycentric frame, associated to different sources, acting on the Cassini spacecraft during a close approach to Titan. The values have been roughly estimated using data from the sources indicated. The acceleration associated to the point mass term is denoted by μ, the one associated to the second degree tidal variations is denoted by k_2 and those associated to all of the l degree spherical harmonics terms combined are denoted by C_{li}. 4

2 Estimated values for the spherical harmonics coefficients of the gravity field of Titan and their 1-σ errors from the GEODYN model, with and without constraining the second degree Love number k_2, and from previous studies. 12

3 Estimated values for the spherical harmonics coefficients of the gravity field of Titan and their 1-σ errors from the GEODYN model with different inequality constraints in the Love number k_2. 17

4 Estimated values for the spherical harmonics coefficients of the gravity field of Titan and their 1-σ errors with and without constraining the second degree Love number k_2 and not including empirical accelerations in both cases. 18

5 Estimated values for the spherical harmonics coefficients of the gravity field of Titan and their 1-σ errors obtained at the tenth iteration when testing freeing the phase of the second degree love number. 20

6 Time, minimum altitude reached, latitude and longitude of the point where that close approach took place and Sun-Earth-Probe (SEP) angle for different Titan flyby arcs. Values taken from Durante et al. (2019) and van Noort (2021). 23

7 Estimated values for the spherical harmonics coefficients and their 1-σ errors when using simulated two-way Doppler data with a Titan point-mass gravity. Four cases were tested with and without empirical accelerations (EA) and measurement biases (MB). 33

8 Estimated values for the spherical harmonics coefficients of the simulated gravity field of Titan and their 1-σ errors when including empirical accelerations and measurement biases. The estimated coefficients for the non-null fields are expressed as the difference with respect to the null field. 36

9 Estimated values for the spherical harmonics coefficients of the simulated gravity field of Titan and their 1-σ errors when including empirical accelerations. The estimated coefficients for the non-null fields are expressed as the difference with respect to the null field. 37

10 Estimated values for the spherical harmonics coefficients of the simulated gravity field of Titan and their 1-σ errors when including measurement biases. The estimated coefficients for the non-null fields are expressed as the difference with respect to the null field. 37

11 Estimated values for the spherical harmonics coefficients of the simulated gravity field of Titan and their 1-σ errors when not including empirical accelerations or measurement biases. The estimated coefficients for the non-null fields are expressed as the difference with respect to the null field. 38

12 Estimated values of the simulated gravity field of Titan when not including empirical accelerations or measurement biases and only estimating the coefficient indicated (as well as μ). The *coefficient* column denotes the results using the field with the corresponding coefficient having the values used in previous tests ($\overline{C}_{20} = -10^{-5}$, $\overline{C}_{22} = 10^{-5}$, $\overline{C}_{30} = 10^{-5}$ and $k_2 = 0.6$). 40

13 Estimated values for the spherical harmonics coefficients of the simulated point-mass gravity field of Titan without ionospheric and tropospheric corrections due to the Earth's atmosphere and also without drag from Titan's atmosphere. No empirical accelerations or measurement biases were estimated. 41
14 Estimated values for the spherical harmonics coefficients of the simulated point-mass gravity field of Titan when extracting the state of Titan from the SPICE ephemeris. The difference with respect to the case where the position of Titan is propagated is also displayed. No empirical accelerations, measurement biases and atmospheric corrections where used. 42
15 Estimated values for the spherical harmonics coefficients of the simulated point-mass gravity field of Titan. The simulated data with only special relativistic effects (SR) and with no relativistic computations (NR) were tested in the GEODYN setup with the corrections turned off in the configuration files. Also simulations were run brute-forcing them to be zero in the software (SR full and NR full). 43
16 Estimated values for the spherical harmonics coefficients obtained from a verification test run of the new estimation setup without simulating noise in the measurements. The column on the right represents the error with respect to the parameters used for generating the observables. 58
17 Estimated values for the spherical harmonics coefficients and their 1-σ errors obtained from a simulated estimation with Gaussian noise of constant 5 mHz standard deviation. The column on the right represents the error with respect to the parameters used for generating the observables. 60
18 Estimated values for the spherical harmonics coefficients and their 1-σ errors obtained from simulated estimations with Gaussian noise of 2.5 mHz, 10 mHz, 25 mHz and 100 mHz standard deviation. 62
19 Estimated values for the spherical harmonics coefficients when simulating analogous estimations to the one performed by Durante et al. (2019). The gravity field from that study was used to generate the data and the 2.5 mHz RMS of residuals from that study was used for the noise. 63
20 Estimated values for the spherical harmonics coefficients obtained from simulated estimations where the relativistic effects were not accounted for and with 5 mHz noise. Different simulated gravity fields where tested and the variations in coefficients are presented with respect to the case with a point-mass gravity. 65
21 Estimated values for the spherical harmonics coefficients obtained from simulated estimations with a +1 s error in receiver timestamps and with 5 mHz noise. Various simulated gravity fields where tested and the changes in coefficients are presented with respect to the case with a point-mass gravity. Different seeds were used for the random number generator in each case. 67
22 Estimated values for the spherical harmonics coefficients obtained from simulated estimations with a +1 s error in receiver timestamps and with 5 mHz noise. Various simulated gravity fields where tested and the changes in coefficients are presented with respect to the case with a point-mass gravity. The same seeds were used for the random number generator in each case. 69
23 Estimated values for the spherical harmonics coefficients obtained from simulated estimations with 1 ms, 10 ms and 100 ms positive error in receiver timestamps, with 5 mHz noise and a simulated point-mass gravity field for Titan. 69

List of Abbreviations

CA Closest Approach
DSN Deep Space Network, NASA
DSS Deep Space Station, DSN
EA Empirical Accelerations
GPU Graphics Processing Unit
GEODYN II software for orbit determination and geodetic parameter estimation, GSFC
GSFC Goddard Space Flight Center, NASA
JPL Jet Propulsion Laboratory, NASA
MB Measurement Biases
NAIF Navigation and Ancillary Information Facility, JPL
NASA National Aeronautics and Space Administration, USA
PDS Planetary Data System, NASA
RMS Root Mean Square
RSW Radial, along-track, cross-track orbital frame of reference
NST Velocity-normal, velocity-tangent, cross-track frame of reference
RTG Radioisotope Thermoelectric Generator
SEP Sun-Earth-Probe (angle)
SPICE Spacecraft, Planet ephemeris, Instrument, C-matrix, Events software, NAIF
TUDAT TU Delft Astrodynamics Toolbox

Abstract

During its thirteen-year long mission in the Saturnian system, the Cassini spacecraft routinely used Titan, Saturn's largest moon, for performing its gravity assists. The problem of determining the gravity field of Titan by performing a precise fit of Cassini's orbit to the available Doppler tracking data was reviewed in this study. The knowledge of the gravity field of Titan can be used to constrain the moon's internal structure and composition, providing clues about its formation process and the properties of an internal ocean (Grasset et al., 2000). Previous solutions obtained by Durante et al. (2019) and van Noort (2021) were respectively found to have inconsistencies regarding the reported small uncertainties given the noise level of the Doppler measurements and the estimation of an unfeasible negative value for the second-degree Love number k_2. It was demonstrated in the present work that this last parameter should be estimable. Here, the data from the ten Titan flybys considered in those studies was analysed and emulated by using a relativistic model for Doppler measurements in search of ways of improving the accuracy of the gravity field solution. Both the GEODYN (McCarthy et al., 2015) software from NASA GSFC and Tudat libraries (see appendices in Dirkx et al., 2019) developed by the Astrodynamics and Space Missions department at TU Delft were used to investigate the nature of this gravity determination problem and compare the results against the previous solutions. A model mismatch in Doppler in the order of 10^2 mHz was found between the estimation setups with GEODYN and Tudat. In the search for the source of the mismodelling, it was tested that the empirical accelerations, measurement biases, measurement timing and the spherical harmonics of Saturn have a great influence on the solution and residuals. Thus, they should be reviewed with care for future estimation efforts. It was proven that the flyby geometry is not favourable for resolving the dipole field spherical harmonics coefficients, especially J_2, C_{22} and k_2, which reveal information about the tidal interactions from Saturn on Titan. They were found to be highly correlated and, when simulating equivalent noises to those found in the previous research, presented similar uncertainties to those obtained by van Noort (2021), but large in relation to the ones determined in Durante et al. (2019). Nevertheless, there are some prospects of estimating the dipole coefficients without the need of adding constraints on the solution, although the search for well grounded constraints is recommended and necessary when pursuing a more accurate solution. The power of fully simulated gravity field estimations as a means for addressing the quality of the available real data and verifying models and constrains, has been manifested throughout this study.

1 Introduction

The study of the gravity field of icy moons like Titan is a topic of great interest for the exploration of the Solar System because it can give clues about their interiors without the need of *in situ* measurements. Internal structures and composition can, in turn, also shed some light into questions about the moon's formation, and help to validate models about the formation of the Solar System. They can, as well, provide information about possible geological processes or interesting internal features like the presence of a core or a layer of liquid water.

Titan is a very interesting moon in many different aspects: it has a thick atmosphere (Yung et al., 1984), it presents large masses of liquid methane (Stofan et al., 2007) and signs of fluvial processes (Jaumann et al., 2008) discovered by the Cassini mission. As other icy moons, Titan is though to be home of a subsurface ocean, heated by tidal dissipation, radiogenic heating and/or internal heat flows (Grasset et al., 2000).

On September 2017 the Cassini probe met its end by plunging into Saturn's atmosphere. During the 13 years that it spend in the Saturnian system, it performed 126 Titan flybys (Andrade, 2018), among which nine where specifically devoted to the determination of the gravity field of Titan by pointing towards Earth with its high gain antenna (Durante et al., 2019). In this introductory chapter, the spherical harmonics approach for modelling the gravity of a planet or large moon is explained, followed by a brief description of the accelerations that perturbed the orbit of the Cassini spacecraft and an explanation of the linear estimation filter used for the determination of the gravity field coefficients of Titan from the available measurements of the Doppler shift experienced by the tracking radio signal. Because of its importance in this work, the measurement modelling behind the Doppler observables is described with more detail at the end of this chapter.

1.1 The Titan gravity determination problem

The gravity field produced by a body with spherical symmetry can be modelled as the one produced by all its mass concentrated at its center, but only outside the body. However, even though large astronomical bodies like planets and some moons tend to be spherical and layered, they present deviations from this symmetry that can be detected by orbiting spacecrafts. These deviations can arise from mass redistribution because of the rotation of the body and tidal interactions, but also from mass inhomogeneities in the interior and topographic features visible at the surface.

Titan, with a mass of $1.35 \cdot 10^{23}$ kg and a radius of 2575 km (De Pater & Lissauer, 2019), can be considered one of those bodies with small deviations from spherical symmetry. As such, its gravitational potential U can be modelled using the spherical harmonics series expansion in a body-fixed frame with the center of mass at the origin:

$$U(r,\phi,\theta) = -\frac{\mu}{r}\sum_{l=0}^{\infty}\sum_{m=0}^{l}\left(\frac{R}{r}\right)^{l} P_{lm}(\sin\phi)\left(C_{lm}\cos m\theta + S_{lm}\sin m\theta\right) \tag{1.1}$$

where r is the distance to the center, ϕ is the latitude, θ is the longitude (for Titan the prime merid-

ian is defined to be pointing towards Saturn at periapsis), μ is Titan's gravitational parameter, R is the reference radius, P_{lm} is the unnormalised Legendre polynomial of degree l and order m and C_{lm} and S_{lm} are the coefficients of the series expansion.

In this expansion, $C_{00} = 1$ (point mass gravity term) and, because the origin is set at the center of mass, all the degree one terms are equal to zero. Also, all $S_{l0} = 0$ by definition. It is common in literature to refer to the C_{l0} ($J_l = -C_{l0}$) coefficients as the zonal coefficients and the rest as the tesseral ones. It is also common to refer to the normalised spherical harmonics coefficients, defined as $\bar{C}_{lm} = C_{lm}/\bar{\mathcal{N}}_{lm}$ and $\bar{S}_{lm} = S_{lm}/\bar{\mathcal{N}}_{lm}$, where

$$\bar{\mathcal{N}}_{lm} = \sqrt{\frac{(2-\delta_{0m})(2l+1)(l-m)!}{(l+m)!}} \tag{1.2}$$

They are used when normalised Legendre polynomials $\bar{P}_{lm} = P_{lm}\bar{\mathcal{N}}_{lm}$ are applied in Eq. 1.1 instead of the unnormalised ones.

The magnitude of the higher degree spherical harmonics coefficients in rocky planets like Earth has been empirically observed to follow what is known as Kaula's rule (Kaula, 2013)

$$\sigma_l^2 = \sum_{m=0}^{l} \left(\bar{C}_{lm}^2 + \bar{S}_{lm}^2\right) \quad \sigma_l^2 \approx \frac{160 \cdot 10^{-12}}{l^3} \tag{1.3}$$

$$\sigma\left\{\bar{C}_{lm}, \bar{S}_{lm}\right\} = \frac{\sigma_l}{\sqrt{2l+1}} \approx \frac{10^{-5}}{l^2} \tag{1.4}$$

Eq. 1.4 is the form most commonly used of Kaula's rule, but Eq. 1.3 estimates better the low degree coefficients. It is possible that this empirical rule of thumb cannot be directly extrapolated to icy moons, and more general modified forms have been proposed (Ermakov et al., 2018).

Usually, the largest contributions to the deviations from the point mass gravity field are due to the body being shaped like an ellipsoid. This shape arises because of the rotational centrifugal accelerations and the tidal potential from close large bodies, in this case, Titan's parent planet Saturn. These perturbing forces do not have spherical symmetry and cause mass redistribution on the body during its formation and evolution. On a relatively large body like Titan, the rotational potential causes an increase in equatorial radius, making the ellipsoid oblate, while the main tidal contribution from Saturn gives rise to a bulge on the hemispheres of the moon facing towards and away from the planet, as Titan is tidally-locked, turning the ellipsoid prolate. This disturbing potential can be projected on to the Titan-centred spherical harmonics function space and assumed to cause a dependant and proportional response in Titan's gravity field (Mitrovica et al., 1994).

An approximation for the second degree average coefficients of the disturbing potential is given by Rappaport et al. (1997)

$$C^T_{20,\text{static}} = -\frac{5}{6}q \quad C_{22,\text{static}^T} = \frac{1}{4}q \quad q = \frac{\mu_S}{\mu}\left(\frac{R}{a}\right)^3 \tag{1.5}$$

The rest of the second degree terms are equal to zero by definition or because Titan's prime meridian is defined to be pointing towards Saturn at periapsis. These expressions only hold for a tidally-locked moon, where the rotational and tidal potential are not independent. In addition, the amplitude of the periodic variations of the perturbing potential dipole field coefficients corresponding to the fundamental orbital frequency can also be modelled as (Iess et al., 2007; Rappaport et al., 1997)

$$C^T_{20,\text{periodic}} = -\frac{3}{2}qe \quad C^T_{22,\text{periodic}} = \frac{3}{4}qe \quad S^T_{22,\text{periodic}} = qe \tag{1.6}$$

where e is the eccentricity of Titan's orbit.

If the physical assumption that Titan is in hydrostatic equilibrium is added, the static response potential to the tidal interactions arising from Titan can be taken as proportional to the average terms of the disturbing one by a single parameter, the fluid Love number k_f and the periodic one as proportional by the second-degree Love number k_2, such that

$$J_2(M) = -k_f C^T_{20,\text{static}} - k_2 C^T_{20,\text{periodic}} \cos(M + \chi_2) \tag{1.7}$$

$$C_{22}(M) = k_f C^T_{22,\text{static}} + k_2 C^T_{22,\text{periodic}} \cos(M + \chi_2) \tag{1.8}$$

$$S_{22}(M) = k_2 S^T_{22,\text{periodic}} \sin(M + \chi_2) \tag{1.9}$$

where M is the mean anomaly: $M = n(t - \tau)$ (τ is the time at which Titan passes through its periapsis) and χ_2 is the periodic tide phase lag. A tidal bulge phase lag discernible from zero at the 1-σ level has not yet been found in previous studies (Durante et al., 2019; Iess et al., 2012).

The k_f parameter is dependent on the interior structure of the fluid body and it can reach a maximum value of $k_f = 3/2$ for a homogeneous composition (Hubbard & Anderson, 1978; Love, 1906). The moon is said to be *fluid* in the sense that mass can flow over geological timescales, but it could be composed of solid material. This should be valid for a body with a strong enough gravity compared to the rigidity of the materials that compose it. This cannot be taken for granted in the case of Titan, which is partially composed of rock and ice (Hunten et al., 1984), so convection of large masses of ice could hypothetically take place (Rappaport et al., 1997). Dividing Eq. 1.7 by Eq. 1.8 the average $J_2/C_{22} = 10/3$ relationship can be derived. This ratio between coefficients is a well known necessary (but not sufficient) condition for hydrostatic equilibrium in a tidally-locked body.

Moving to the acceleration modelling of the orbit of the Cassini spacecraft, Table 1 provides a reference for the expected magnitudes of the different accelerations that are experienced by Cassini. It is very important to realise that these magnitudes can be sometimes misleading about the real scope of the effects they cause on the spacecraft's trajectory. For instance, the direction in which they take place, when their magnitude is the largest, as well as their temporal evolution can greatly influence the magnitude of their actual manifestation in the Doppler tracking signal. Usually, the accelerations in the along-track direction of the spacecraft (i.e. the direction parallel to its velocity) when it is closest to Titan will lead to the greatest differences in state. Thus, the orbit solution will tend to capture better the values of the parameters associated to these accelerations, while other parameters will be more susceptible to the noise from the measurement errors.

Another relevant aspect to take into account is that, because the accelerations in Tab. 1 are expressed in the Solar System barycentric frame and the position of Cassini would be numerically integrated in the frame of the Saturn system, the effective magnitude of some of the third body contributions, more specifically those from distant objects like the Sun and the planets, is smaller than that presented on the table. The reason for this is that they produce almost equal accelerations on both Cassini and Saturn. Thus, the perturbation experienced by Cassini in the Saturnian system frame is caused by the slight acceleration mismatch due to the difference in relative position with respect to the perturbing body over a large distance.

As it can be observed in Tab. 1, the most important accelerations acting on Cassini during a flyby will be those corresponding to the point mass gravity of Titan and Saturn. The rest of the accelerations arise from perturbations that are orders of magnitude smaller. Among the non-gravitational accelerations, atmospheric drag is, as expected, the most important one, because Cassini enters well into Titan's on its closest approaches (see Tab. 6 in Section 3.1.1). Drag is then followed by RTG emissions, which are three orders of magnitude smaller, and then solar radiation pressure, which is just a fraction of the thermal emissions. Nevertheless, the fact that the expected

Acceleration source			Magnitude (m/s^2)
Gravity	Titan	μ	$\sim 10^{-1}$ (Durante et al., 2019; Iess et al., 2010)
		C_{2i}	$\sim 10^{-6}$ (Durante et al., 2019; Iess et al., 2012)
		C_{3i}	$\sim 10^{-7}$ (Durante et al., 2019; Iess et al., 2012)
		C_{4i}	$\sim 10^{-7}$ (Eq. 1.4)
		C_{5i}	$\sim 10^{-8}$ (Eq. 1.4)
		k_2	$\sim 10^{-8}$ (Durante et al., 2019; Iess et al., 2012)
	Saturn	μ_S	$\sim 10^{-2}$ (Iess et al., 2019)
		$C_{2i,S}$	$\sim 10^{-5}$ (Iess et al., 2019)
	Rhea		$\sim 10^{-7}$ (De Pater & Lissauer, 2019)
	Sun		$\sim 10^{-5}$ (De Pater & Lissauer, 2019)
	Jupiter		$\sim 10^{-7}$ (De Pater & Lissauer, 2019)
	Earth		$\sim 10^{-10}$ (De Pater & Lissauer, 2019)
Atmospheric drag			$\sim 10^{-6}$ (Durante et al., 2019)
RTG emissions			$\sim 10^{-9}$ (Bertotti et al., 2003)
Radiation pressure			$\sim 10^{-10}$ (Bertotti et al., 2003)
Relativistic corrections	Schwarzschild		$\sim 10^{-11}$ (De Pater & Lissauer, 2019)
	Lense-Thirring		$\sim 10^{-12}$ (De Pater & Lissauer, 2019)
	de Sitter		$\sim 10^{-13}$ (De Pater & Lissauer, 2019)

Table 1: Maximum magnitudes of the accelerations in the Solar System barycentric frame, associated to different sources, acting on the Cassini spacecraft during a close approach to Titan. The values have been roughly estimated using data from the sources indicated. The acceleration associated to the point mass term is denoted by μ, the one associated to the second degree tidal variations is denoted by k_2 and those associated to all of the l degree spherical harmonics terms combined are denoted by C_{li}.

magnitude of the accelerations produced by Titan's spherical harmonics up to degree five is similar to those of several third body perturbations and some of the non-gravitational sources, serves to outline the necessity of a model as complete and accurate as possible if a meaningful solution for the gravity field is to be obtained. From Tab. 1 it can also be anticipated that the zonal spherical harmonics of Saturn should be incorporated into the model. An estimation of these zonal coefficients up to the eighth degree, as well as the mass of Saturn's rings, has been performed by Iess et al. (2019). Finally, post-Newtonian relativistic corrections on the orbit propagation are extremely small (although around just an order of magnitude under radiation pressure or the quadrupole field of Saturn), but they are usually relatively easy to incorporate into the dynamical model.

In order to determine the gravity field of Titan, the multi-dimensional dynamical model of the spacecraft's orbit has to be fitted to real velocity observations obtained through measuring the Doppler effect experienced by the radio tracking signal. The model can be fitted using the least squares method (Schutz et al., 2004), where the estimation problem can be formulated as an optimisation one:

$$\mathbf{y} = h(\mathbf{x}) + \boldsymbol{\epsilon} \quad J = \boldsymbol{\epsilon}^T P_y^{-1} \boldsymbol{\epsilon} \tag{1.10}$$

where $\mathbf{y}$ are the observations, $\mathbf{x}$ is the vector of problem parameters, $h(\mathbf{x})$ is the measurement and dynamical model, $\boldsymbol{\epsilon}$ are the residuals and J is the objective function to be minimised, which is a quadratic form of the residuals weighted by the inverse of the covariance matrix P_y of the

measurements.

In this gravity determination problem, the dynamics of the system and observation equations, defined within the multidimensional vector function $h(\mathbf{x})$, are non-linear. As such, the system can be linearised in order to solve the problem, such that

$$\mathbf{y} \approx h(\mathbf{x}_0) + \frac{\partial h}{\partial \mathbf{x}}(\mathbf{x}_0)(\mathbf{x} - \mathbf{x}_0) + \boldsymbol{\epsilon} \tag{1.11}$$

This linearisation can then be expressed in a incremental formulation where a correction $\Delta\mathbf{x}$ to the initial guess is to be estimated by taking the residuals from the initial guess as observations $\Delta\mathbf{y} = \mathbf{y} - h(\mathbf{x}_0)$, so

$$\Delta\mathbf{y} = H(\mathbf{x})\Delta\mathbf{x} + \boldsymbol{\epsilon} \tag{1.12}$$

Then the solution to the problem can be obtained iteratively:

$$\hat{\mathbf{x}}_{(n+1)} = \hat{\mathbf{x}}_{(n)} + \left(H^T(\hat{\mathbf{x}}_{(n)})P_y^{-1}H(\hat{\mathbf{x}}_{(n)})\right)^{-1} H^T(\hat{\mathbf{x}}_{(n)})P_y^{-1}\Delta\mathbf{y}_{(n)} \tag{1.13}$$

There are some important caveats to this method. Namely, this method only serves to find local minima of the cost function, and convergence cannot always be guaranteed for an arbitrary non-linear system. As a consequence, the selection of initial guesses can be very relevant and should be justified and handled with care, as the solution might converge to different values for different initial guesses or not converge at all.

The next step is to formulate how the differential changes in the initial state of the spacecraft and the force parameters translate into variations in the propagated state. These are known as the variational equations. Considering all the accelerations involved on the dynamical modelling of the orbit, the equations of motion governing the trajectory of Cassini can be expressed as

$$\frac{d\mathbf{X}(t)}{dt} = F(t, \mathbf{X}, \mathbf{p}) \quad \text{with} \quad \mathbf{X}(t_0) = \mathbf{X}_0 \tag{1.14}$$

where $\mathbf{X}$ is a vector containing the state of the spacecraft (in this case its position and velocity in the Titan body-fixed frame), $\mathbf{p}$ is a vector containing the force parameters and F is a vector function which models the spacecraft dynamics. The solution of the previous differential equation can be linearised for small changes in the initial conditions and force parameters as

$$\Delta\mathbf{X}(t) = \frac{\partial\mathbf{X}(t)}{\partial\mathbf{X}(t_0)}\Delta\mathbf{X}_0 + \frac{\partial\mathbf{X}(t)}{\partial\mathbf{p}}\Delta\mathbf{p} \tag{1.15}$$

From the previous equation, the state transition matrix Φ, as well as the sensitivity matrix S, can be defined as (Montenbruck & Gill, 2001)

$$\Phi(t, t_0) = \frac{\partial\mathbf{X}(t)}{\partial\mathbf{X}(t_0)} \quad S(t) = \frac{\partial\mathbf{X}(t)}{\partial\mathbf{p}} \tag{1.16}$$

The time dependence of these matrices can be determined by solving the following differential equations

$$\frac{d\Phi(t, t_0)}{dt} = \frac{\partial F(t, \mathbf{X}, \mathbf{p})}{\partial\mathbf{X}(t)}\Phi(t, t_0) \quad \text{with} \quad \Phi(t_0, t_0) = I \tag{1.17}$$

$$\frac{dS(t)}{dt} = \frac{\partial F(t, \mathbf{X}, \mathbf{p})}{\partial\mathbf{X}(t)}S(t) + \frac{\partial F(t, \mathbf{X}, \mathbf{p})}{\partial\mathbf{p}} \quad \text{with} \quad S(t_0) = 0 \tag{1.18}$$

in which I is the identity matrix and 0 is a matrix full of zeros, all sizes consistent with the number of state components and parameters. Eqs. 1.17 and 1.18 are derived from Eqs. 1.14 and 1.15.

The previous set of equations allows for the establishment of an incremental linear relationship, analogous to Eq. 1.12, between the observations, the initial state and the rest of the parameters:

$$\Delta \mathbf{y}_k = \tilde{H}_k \Delta \mathbf{X}(t_k) + \boldsymbol{\epsilon}_k = \tilde{H}_k \left(\Phi(t_k, t_0) \Delta \mathbf{X}_0 + S(t) \Delta \mathbf{p} \right) + \boldsymbol{\epsilon}_k \tag{1.19}$$

The matrix $\tilde{H}$ is known as the observation matrix and, as its name implies, it directly relates the state at a certain epoch with the available measurements. Finally, all the available measurements can be grouped into a single inversion problem for the entire flyby arc:

$$\Delta \mathbf{y} = \begin{bmatrix} \Delta \mathbf{y}_0 \\ \vdots \\ \Delta \mathbf{y}_k \\ \vdots \\ \Delta \mathbf{y}_f \end{bmatrix} = \begin{bmatrix} \tilde{H}_0 \Phi(t_0, t_0) & \tilde{H}_0 S(t_0) \\ \vdots & \vdots \\ \tilde{H}_k \Phi(t_k, t_k) & \tilde{H}_k S(t_k) \\ \vdots & \vdots \\ \tilde{H}_f \Phi(t_f, t_f) & \tilde{H}_f S(t_f) \end{bmatrix} \begin{bmatrix} \Delta \mathbf{X}_0 \\ \Delta \mathbf{p} \end{bmatrix} + \begin{bmatrix} \boldsymbol{\epsilon}_0 \\ \vdots \\ \boldsymbol{\epsilon}_k \\ \vdots \\ \boldsymbol{\epsilon}_f \end{bmatrix} = H \Delta \mathbf{x} + \boldsymbol{\epsilon} \tag{1.20}$$

The equations that have been presented so far are expressed for a single trajectory arc with its associated initial state to be estimated. However, in cases like this Titan gravity determination problem, where the Cassini data comes from several flybys over the moon that are distributed over a decade in time, the trajectory should be divided into multiple arcs, one for each flyby. As such, a distinction can be made between those parameters like the initial state that are specific to each flyby, the arc parameters, and those that are theoretically expected to be constant for all the flybys, like the coefficients gravity field model, which are referred as the global parameters. A particular and relevant set of arc parameters are te empirical accelerations (Schutz et al., 2004) which are usually defined in the RSW orbital reference frame (Vallado, 2001) and their purpose is to account for model mismatches.

To conclude, when considering a multi-arc solution, the linearised normal equations from all the flybys can be combined into a single iterative equation similar to Eq. 1.13 (van Noort, 2021):

$$\hat{\mathbf{x}}_{(n+1)} = \hat{\mathbf{x}}_{(n)} + \left(\sum_{i=1}^{N_{\text{flybys}}} H_i^T P_{y,i}^{-1} H_i + \bar{P}_x^{-1} \right)^{-1} \left(\sum_{i=1}^{N_{\text{flybys}}} H_i^T P_{y,i}^{-1} \Delta \mathbf{y}_{i,(n)} + \bar{P}_x^{-1} \Delta \bar{\mathbf{x}}_{(n)} \right) \tag{1.21}$$

In this equation, the additional terms correspond to the a priori constraints in the solution, with $\bar{P}_x$ being the covariance matrix (usually just a diagonal matrix with the variances of the a priori known values) and $\Delta \bar{\mathbf{x}}$ the difference between the parameter vector and the vector of a priori values. It can be proved how the approach of adding the normal matrices for each flyby presented in Eq. 1.21 is mathematically equivalent to stacking all the design matrices into a single one and then performing the least-squares inversion.

In this case, the a priori values for the parameters to be estimated will constrain the solution, conditioning its final value. This fact is in a sense a double-edged sword. On the one hand, as mentioned before, this additional restriction can be advantageous when the solution lacks stability. On the other hand, the selected a priori values can pollute the solution, not allowing for the appearance of the actual real values that might be hidden in the data signal. For that last reason, it is important that, when using a priori information about the parameters in the estimation process, these values are supported by reliable sources and the magnitude of their associated uncertainties is well defined by the $\bar{P}_x$ matrix.

1.2 Doppler measurements

The measurements used in this study for the determination of the gravity field of Titan are two-way and three way observables obtained from Cassini through the Deep Space Network (DSN).

In these kinds of measurements the transmitting ground station generates a signal with a certain frequency which is then received and re-emitted by the spacecraft so it can then be collected again by the receiver antennae back at the Earth. Two-way measurements refer to the case where the receiver and transmitter antennae are the same one while in three-way observables the transmitting and receiving stations are different ones (for reference, see Moyer, 2005). Because of the relative velocity between the spacecraft and the ground stations, a Doppler shift is experienced by the signal both during the uplink and the downlink, as depicted in Fig. 1, allowing for the precise tracking of the probe.

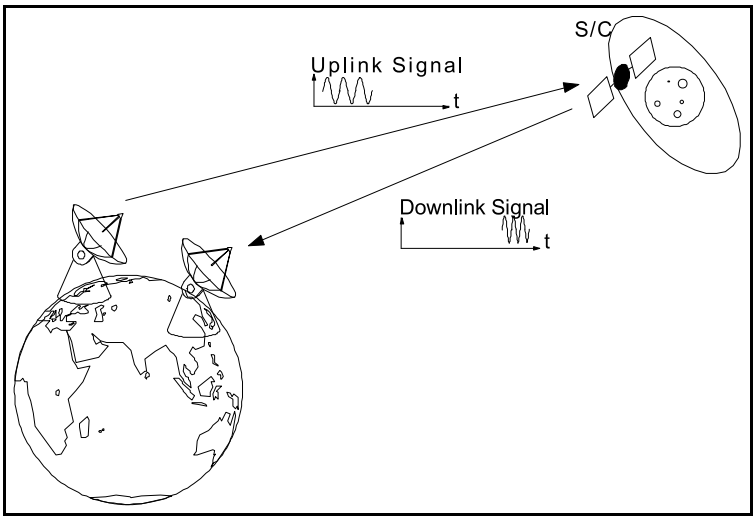

Figure 1: Schematic of a three-way Doppler observation of a spacecraft's relative velocity. Figure taken from Weischede et al. (1999).

In order to model the Doppler shift experienced by Cassini's radio tracking signal a relativistic version of the Doppler equation was used in this work which included the special relativity proper clock drift, as well as first-order approximations of the general relativistic effects, of gravitational redshift and the curved geodesics. The last ones affect the direction from which the relative velocity is perceived and also increase the light propagation distance, adding some time delay known as the Shapiro effect (Shapiro et al., 1971).

Here, the formulation presented in Bocanegra-Bahamón et al. (2018) and Kopeikin and Schäfer (1999) will be used. Considering a transmitter and a receiver at an interplanetary distance within the Solar System, if t_T and t_R are, respectively, the signal transmission and reception times and $\mathbf{r}_R = \mathbf{r}_R(t_R)$, $\mathbf{r}_T = \mathbf{r}_T(t_T)$, $\mathbf{v}_R = \mathbf{v}_R(t_R)$, $\mathbf{v}_T = \mathbf{v}_T(t_T)$ are the barycentric positions and velocities of the transmitter and receiver divided by the speed of light, then the relativistic Doppler equation can be approximated as

$$\nu_{R,T}(t_R) = \frac{f_R}{f_T} = \frac{1-\mathbf{k}\cdot\mathbf{v}_R}{1-\mathbf{k}\cdot\mathbf{v}_T}\left(\frac{1-v_T^2}{1-v_R^2}\right)^{1/2}\left(\frac{a_T(\boldsymbol{\tau}_T)}{a_R(\boldsymbol{\tau}_R)}\right)^{1/2}\frac{b_R(\boldsymbol{\tau}_R)}{b_T(\boldsymbol{\tau}_T)} \tag{1.22}$$

where the first term corresponds to the classical Doppler effect, the second one is the special relativistic correction and a_T, a_R, b_T and b_R are general relativistic terms associated to the gravitational redshift. The vector $\mathbf{k}$ is the light propagation vector (null geodesic to negative infinity, Eq. 1.26). The transmitted and received frequencies are denoted by f_T and f_R respectively. The vector of times $\boldsymbol{\tau}_S = (t_S, s_{S1}, \ldots, s_{SN})$, with $S \equiv R$ or T depending on whether they refer to reception or transmission (this notation will be used from now on), also includes the light times s_{Sa} from reception and transmission at which the massive body a (the Sun, planets, moons, N is the total number of bodies used for the general relativistic corrections) is. As the name implies, the light-time refers to the time it takes to travel the shortest distance between two points in space at the speed of light. In the interplanetary scale of the Cassini measurements (see again Fig. 1), light-times are quite significant, in the order of an hour.

The different times used for Eq. 1.22 are obtained with the following light time equations:

$$t_R - t_T = |\mathbf{r}_R - \mathbf{r}_T| + \Delta(\boldsymbol{\tau}_R, \boldsymbol{\tau}_T) \tag{1.23}$$

$$t_S - s_{Sa} = |\mathbf{r}_S(t_S) - \mathbf{r}_a(s_{Sa})| \tag{1.24}$$

These equations are implicit and, as such, to obtain the different times, $2N+1$ light time equations need to be solved numerically using the ephemeris for all the relevant bodies. For simplicity, in the following equations $\mathbf{d}_{Sa} = \mathbf{r}_S(t_S) - \mathbf{r}_a(s_{Sa})$.

The $\Delta(\boldsymbol{\tau}_R, \boldsymbol{\tau}_T)$ in Eq. 1.23 is the general relativistic time delay that was mentioned before caused by the space-time being curved by a massive body like the Sun. This delay can be calculated as

$$\Delta(\boldsymbol{\tau}_R, \boldsymbol{\tau}_T) = -2\sum_{a=1}^{N} m_a \left(\ln \frac{d_{Ra} - \mathbf{k}\cdot\mathbf{d}_{Ra}}{d_{Ta} - \mathbf{k}\cdot\mathbf{d}_{Ta}} - (\mathbf{k}\cdot\mathbf{v}_{Ra}) \ln(d_{Ra} - \mathbf{k}\cdot\mathbf{d}_{Ra}) + (\mathbf{k}\cdot\mathbf{v}_{Ta}) \ln(d_{Ta} - \mathbf{k}\cdot\mathbf{d}_{Ta}) \right) \tag{1.25}$$

where the reduced mass $m_a = GM_a/c^3$, being M_a the mass of body a, G the universal gravity constant and c the speed of light.

The relativistic propagation vector used for the Doppler equation can be calculated as

$$\mathbf{k} = -\frac{\mathbf{r}_R - \mathbf{r}_T}{|\mathbf{r}_R - \mathbf{r}_T|} - \boldsymbol{\beta}_R(\boldsymbol{\tau}_R) + \boldsymbol{\beta}_T(\boldsymbol{\tau}_T) \tag{1.26}$$

where the general relativistic terms correspond to

$$\boldsymbol{\beta}_S^i(\boldsymbol{\tau}_S) = -\frac{2}{|\mathbf{r}_R - \mathbf{r}_T|}\sum_{a=1}^{N} m_a \frac{1 - \mathbf{k}\cdot\mathbf{v}_{Sa}}{\sqrt{1 - v_{Sa}^2}} \frac{d_{Sa}^i - k^i(\mathbf{k}\cdot\mathbf{d}_{Sa})}{d_{Sa} - \mathbf{k}\cdot\mathbf{d}_{Sa}} - \frac{4}{|\mathbf{r}_R - \mathbf{r}_T|}\sum_{a=1}^{N} \frac{m_a}{\sqrt{1 - v_{Sa}^2}} (v_{Sa}^i - k^i(\mathbf{k}\cdot\mathbf{v}_{Sa})) \ln(d_{Sa} - \mathbf{k}\cdot\mathbf{d}_{Sa}) \tag{1.27}$$

Finally, the a and b terms for the general relativistic drift are obtained from the following expressions:

$$a_S(\boldsymbol{\tau}_S) = 1 + 2\sum_{a=1}^{N} \frac{m_a\sqrt{1 - v_{Sa}^2}}{d_{Sa} - \mathbf{v}_{Sa}\cdot\mathbf{d}_{Sa}} - \frac{4}{1 - v_S^2}\sum_{a=1}^{N} \frac{m_a}{\sqrt{1 - v_{Sa}^2}} \frac{(1 - \mathbf{v}_S\cdot\mathbf{v}_{Sa})^2}{d_{Sa} - \mathbf{v}_{Sa}\cdot\mathbf{d}_{Sa}} \tag{1.28}$$

$$b_S(\boldsymbol{\tau}_S) = 1 + 2\sum_{a=1}^{N} \frac{1 - \mathbf{k}\cdot\mathbf{v}_{Sa}}{d_{Sa} - \mathbf{v}_{Sa}\cdot\mathbf{d}_{Sa}} \left(\frac{(1 - \mathbf{k}\cdot\mathbf{v}_{Sa})(\mathbf{k}\times\mathbf{v}_S)\cdot(\mathbf{k}\times\mathbf{d}_{Sa})}{d_{Sa} - \mathbf{k}\cdot\mathbf{d}_{Sa}} - \frac{(\mathbf{k}\times\mathbf{v}_{Sa})\cdot(\mathbf{k}\times\mathbf{d}_{Sa})}{d_{Sa} - \mathbf{k}\cdot\mathbf{d}_{Sa}} + \mathbf{k}\cdot\mathbf{v}_{Sa} \right) \tag{1.29}$$

As just mentioned, the light time equations (Eqs. 1.23 and 1.24) are implicit and need to be solved iteratively. This can be dome for instance with a Newton-Raphson method:

$$F(\boldsymbol{\tau}) = \mathbf{0} \Rightarrow 0 = F^i(\boldsymbol{\tau}_{(n)}) + \frac{dF^i}{d\tau^i}(\boldsymbol{\tau}_{(n)})(\tau_{(n+1)}^i - \tau_{(n)}^i) \tag{1.30}$$

$$\frac{dF^i}{d\tau^i}(\boldsymbol{\tau}_{(n)}) = \frac{(\mathbf{x}_k(\tau^k_{(n)}) - \mathbf{x}_i(\tau^i_{(n)})) \cdot \mathbf{v}_i(\tau^i_{(n)})}{|\mathbf{x}_k(\tau^k_{(n)}) - \mathbf{x}_i(\tau^i_{(n)})|} \tag{1.31}$$

As suggested by the previous equation, it is not necessary to compute the derivative of the $\Delta(\boldsymbol{\tau}_R, \boldsymbol{\tau}_T)$ term of Eq. 1.23 in order to converge to the solution. In Section 3.1.2 it is checked that this term is indeed small in comparison to the classical light time. When dealing with a series of points that are close in time to each other, as is usually the case when dealing with spacecraft tracking data, a computationally efficient approach is to initialise the solver with t_R on the first Doppler point and then, for the next data points, use the light times from the previous point as an excellent initial guess.

When considering two and three-way observables, if now the subindex T refers to the transmitter (a DSN antenna), TR to the transceiver (in this case, the high-gain or low-gain antennae on board Cassini) and R the receiver (the same or another DSN station), the received frequency after the round-trip can be formulated using Eq. 1.22 as

$$f_R = \nu_{R,TR}(t_{TR}) f_{TR} = \nu_{R,TR}(t_{TR}(t_R))\nu_{TR,T}(t_R) M f_T \tag{1.32}$$

In this last equation, M represents the spacecraft's turnaround ratio, which is the ratio between the frequencies of the received uplink signal and the downlink signal transponded by the probe. The spacecraft multiplies the received frequency by this factor so it can transmit back the signal at different frequency. Although Cassini was also capable of using the Ka-band, only the X-band measurements were considered in this study, as it was not possible to use the Ka-band in both uplink and downlink because of a malfunction in the frequency translator (there is data available using mixed bands). For the Cassini mission, the turnaround ratio used was $M = 880/749$ and the nominal uplink frequency in the X-band was $f_T = 7.175$ GHz (Taylor et al., 2002).

Often in classical terms it is useful to use the following turnaround relationship where v is considered positive when the spacecraft is moving towards the observer (Moyer, 2005):

$$f_R = \frac{1 + v/c}{1 - v/c} M f_T \approx \left(1 + \frac{v}{c}\right) M f_T \Longrightarrow v = \frac{1}{2}\frac{c}{M f_T}\Delta f \tag{1.33}$$

where $\Delta f = f_R - f_T$. This expression will later be used in Chapter 3 to translate Doppler into relative velocity to feed simulated data to the GEODYN estimation software (see also Chapter 2).

1.3 Research questions

To finish this introductory chapter, the research questions that were addressed in this study are going to be formulated. The reason behind starting this investigation was the fact that the previous study conducted by van Noort (2021) attempted to replicate the results obtained by an earlier estimation of the gravity field of Titan by Durante et al. (2019) but achieved a different solution. In their work, Durante et al. (2019) present a spherical harmonics gravity field solution up to degree and order five. However, some concern can be raised about the small uncertainties they obtain for the coefficients given the underlying noise level in the measurements, especially as they only mention using an a priori constrain in the initial states and no reference is made about the use of empirical accelerations. Regarding the estimation performed by van Noort (2021), the very relevant second degree Love number k_2 could not be obtained as, when unconstrained, it would return unfeasible negative values. This behaviour was again observed and studied in this work. Given the current state-of-the-art, the principal research question for this study is set to be the following:

In which aspects can previous estimates of the gravity field of Titan with Cassini data be improved?

This question can be further developed into four sub-questions:

- *What are the effects of the empirical accelerations on the solution obtained with the setup for estimating with real data?*
- *How effective are the inequality constraints in stabilising the gravity solution and driving it away from an unfeasible negative value for the second degree Love number k_2?*
- *What are the causes for the large signal in the residuals in the fit obtained when feeding simulated data to the setup used to estimate with real data?*
- *In which aspects is the Titan gravity determination problem fundamentally susceptible to noise or modelling errors?*

The effort that was made to address these questions is reported in the following chapters. The first two correspond to Chapter 2 while the third and fourth ones are investigated in Chapters 3 and 4 respectively.

Lastly, a mention should be made of the tools that were used to answer these questions. They will be described in the next chapters, but they were mainly NASA GSFC's GEODYN II software (McCarthy et al., 2015) for performing arc estimations and calculating the variational equations, a version of the global inversion software used by van Noort (2021) for GEODYN (modified to include inequality constraints), NASA's SPICE Toolbox (Acton, 1996) for working with the ephemeris, a software implementation of the Doppler measurement model just described that was done during this study, the trajectory propagation and variational equations tools from the Tudat software developed at TU Delft (see appendices in Dirkx et al., 2019) and a custom global inversion software built over the functionality provided by Tudat.

2 Estimation with real data

The premise for the work carried out in this thesis was to continue and further expand the research performed by van Noort (2021), where one of the main issues reported was the inability to obtain a feasible value for the second degree Love number k_2. As such, the starting point for this project has been to test the setup from that previous study. As it will be seen, different modifications have been introduced to this preliminary model as a variety of concerning issues limiting the prospects of improving the previous solution have been found. This preceding estimation effort made use of the GEODYN II software tool developed at NASA's Goddard Space Flight Center (McCarthy et al., 2015) in combination with a global inversion software to achieve a multi-arc solution.

2.1 Issues with the estimation setup with GEODYN

The starting GEODYN model used in this study was configured with the same GEODYN setup files as those used by van Noort (2021) for his baseline model. The estimation of different arc and global parameters is requested in these files on an arc basis and, GEODYN being a capable and well established (decades-old) program for orbit determination and gravity field studies, there are a lot of options in terms of defining which parameters to estimate. In this case, the relevant global parameters include Titan's gravitational parameter, spherical harmonics and tide parameters (k_2 and its phase and k_3), along with Cassini's drag and radiation pressure coefficients. In the GEODYN model the tide parameters were constrained to be null, and the gravity field of Titan is only estimated up to degree and order three. The arc parameters consist of empirical accelerations, impulsive corrections for thruster firings, Cassini's initial state and simple measurement biases. It should be noted that the empirical accelerations were formulated as constant in the RSW reference system (Vallado, 2001) during eight-hour long intervals, resulting in around four sets of empirical acceleration vector components per flyby, depending on its duration.

It should also be mentioned that some modifications were already introduced directly into the GEODYN software for the study by van Noort (2021), namely the gravitational effect of Saturns's zonal spherical harmonics, its eight largest moons and its rings, as well as the direct propagation of Titan's position and ensuring the correct positioning of Saturn (to avoid placing the planet at the Saturnian System barycentre, as it would be done by default). This modified version of the program is also used for the tests that will follow, although some additional slight modifications were necessary for the tests described in Chapter 3.

What changes with respect to the estimation procedure in van Noort (2021) is the way global iterations are performed. In his work, after performing the arc iterations with GEODYN, an extra turnaround run of the program is performed, where the arc parameters that were estimated are taken as a priori values in order to check and ensure the stability of the solution. For the present study it has been decided to not perform those runs, which explains the small differences between the results for preliminary coefficients when the Love number is constrained and those estimated in van Noort (2021), as can be seen in Tab. 2. The rationale for skipping that step in this work is that constraining the arc parameters in that way to the previously estimated ones gives an unrealistic

stability to the solution. In order to verify and try to improve the solution, it is precisely the robustness of the original problem that generated the values for the local parameters in the first place what needs to be assessed, unmasked by the effects caused by this artificial relationship arising from the problem itself.

Case	$k_2 = 0$	Unconstrained k_2	Durante et al. (2019)	van Noort (2021)
μ (km^3/s^2)	8978.0285 ± 0.0130	8978.0247 ± 0.0130	8978.1383 ± 0.0003	8977.9810 ± 0.0130
k_2	-	-3.549 ± 0.666	0.616 ± 0.067	-
$J_2 \times 10^6$	30.383 ± 1.532	102.782 ± 13.639	33.089 ± 0.609	30.607 ± 1.536
$C_{21} \times 10^6$	-4.283 ± 0.796	-2.493 ± 0.862	0.513 ± 0.215	-4.411 ± 0.798
$S_{21} \times 10^6$	13.745 ± 1.225	9.668 ± 1.477	0.612 ± 0.359	12.042 ± 1.230
$C_{22} \times 10^6$	7.772 ± 0.501	42.728 ± 6.601	10.385 ± 0.084	8.331 ± 0.502
$S_{22} \times 10^6$	-1.706 ± 0.459	1.479 ± 0.742	-0.064 ± 0.066	-2.258 ± 0.459
$J_3 \times 10^6$	1.399 ± 2.201	-13.506 ± 3.389	-0.179 ± 0.720	1.143 ± 2.207
$C_{31} \times 10^6$	1.652 ± 0.630	0.206 ± 0.669	1.481 ± 0.254	1.419 ± 0.631
$S_{31} \times 10^6$	6.588 ± 1.107	11.139 ± 1.353	0.811 ± 0.402	6.160 ± 1.108
$C_{32} \times 10^6$	-1.414 ± 0.370	0.900 ± 0.550	0.183 ± 0.153	-1.251 ± 0.370
$S_{32} \times 10^6$	0.068 ± 0.261	-1.752 ± 0.424	-0.027 ± 0.099	-0.139 ± 0.261
$C_{33} \times 10^6$	-0.012 ± 0.090	-0.148 ± 0.093	-0.222 ± 0.017	0.018 ± 0.090
$S_{33} \times 10^6$	-0.646 ± 0.089	-0.516 ± 0.094	-0.226 ± 0.019	-0.611 ± 0.090
RMS residuals	5.209 mHz	5.110 mHz	-	-

Table 2: Estimated values for the spherical harmonics coefficients of the gravity field of Titan and their 1-σ errors from the GEODYN model, with and without constraining the second degree Love number k_2, and from previous studies.

Tab. 2 shows the results with this GEODYN model, as well as the results obtained by Durante et al. (2019) and van Noort (2021) for comparison. The values presented for the estimation tests for the current work (labelled as null and uncostrained k_2) were obtained after ten global iterations, which proves sufficient for reaching convergence (the number of arc iterations is controlled by GEODYN by checking the convergence of the arc solutions). It can be observed that the estimated parameters when $k_2 = 0$ are very similar to those from van Noort (2021) and the formal errors are practically the same. The later is to be expected as the same observation and constraint variances are used in both cases.

When comparing these solutions with the one from Durante et al. (2019) it can be observed clearly that they do not agree. Even though there is some similarity in J_2 and C_{22}, most relevant terms in the dipole field for their relation to the moon's hydrostatic equilibrium (or lack of) and tidal interactions, the GEODYN solution also shows high values for the other second-degree parameters, with S_{21} actually larger than C_{22}. This result would mean that there is no hydrostatic equilibrium, something physically unexpected for a moon with a suspected internal water layer (Grasset et al., 2000). Also, the large S_{22} suggests that the equilibrium tide bulge has a considerable deviation from pointing towards Saturn, another concerning result. Additionally, there is not really any agreement when considering the degree three coefficients, and they are larger in general in the model considered here. Nevertheless, it is a good sign that they are smaller relative to the dipole ones, consistent with what it is observed in other planetary bodies (Ermakov et al., 2018; Kaula, 2013; Lemoine et al., 2014). The formal errors are up to about one order of magnitude bigger compared to those given by Durante et al. (2019), which serves to point out a deeper disagreement between the models and how they process the data. Last but not least, de-

spite looking very similar, the differences observed in the estimated gravitational parameter are important when considering the fact that their associated difference in acceleration is in the order of magnitude of the acceleration from the J_2 term.

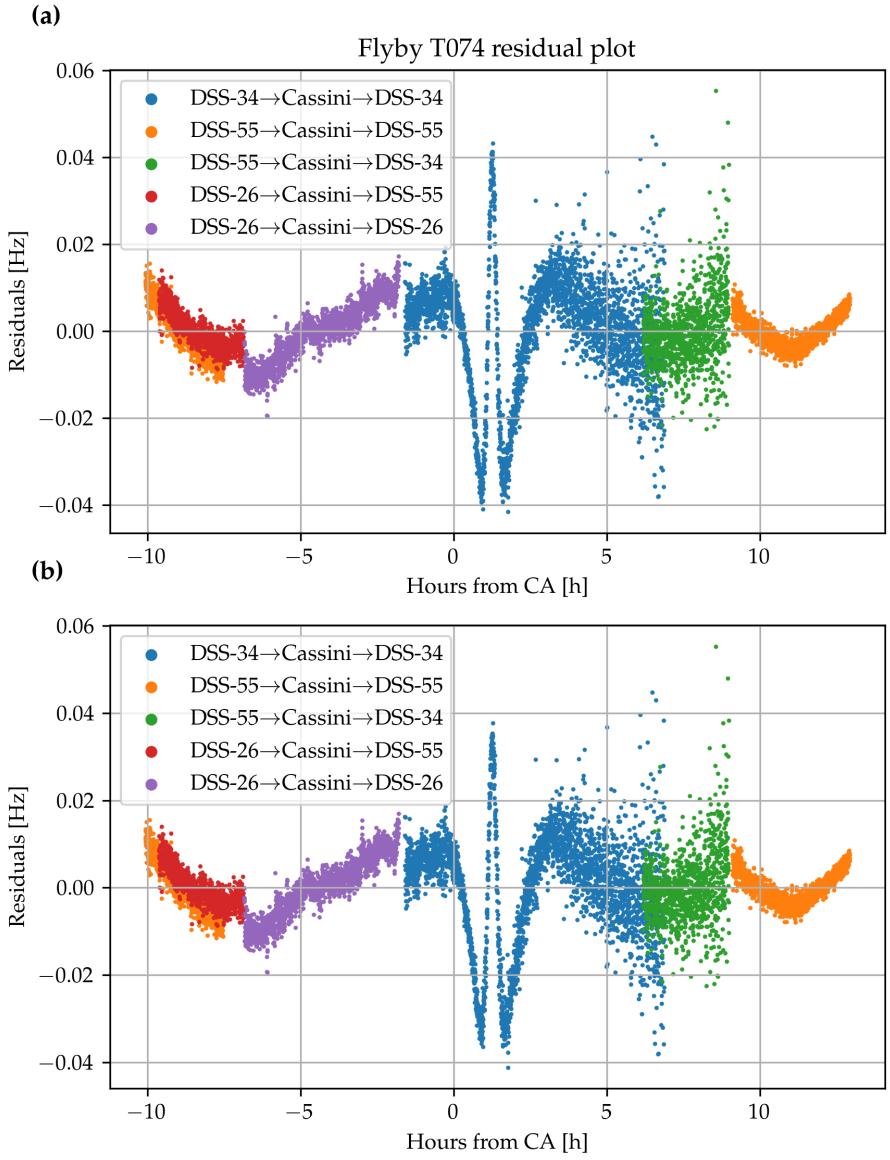

Figure 2: Doppler residuals for flyby T074 for **(a)** the case with null Love number k_2 and **(b)** unconstrained k_2. The shape and magnitude (9.431 mHz vs. 9.094 mHz RMS respectively) of the residuals is almost identical in both cases despite the large difference in estimated coefficients. Closest approach takes place at 16:04, February 18, 2011.

The reason why the Love number is not estimated in the GEODYN solution is because it strongly tends towards negative values. The estimated value in the unconstrained case is completely unphysical, as it would imply that the periodic variation of the tidal disturbing potential from Saturn due the eccentricity of Titan's orbit is repelling matter or, in other words, the periodic tidal bulge has a 90° phase offset with respect to the vector pointing towards Saturn (Eqs. 1.7-1.9).

Looking at the RMS of the residuals in Tab. 2 for the two cases that are being analised here,

it can be noticed that the fits are really similar in terms of residuals and that they are slightly smaller when k_2 is estimated. This last result is to be expected, as the unconstrained estimation, provided that it converges, has more freedom to minimise the residuals by having an extra free parameter. However, what is striking is that the two estimations produce the same global RMS despite converging to radically different spherical harmonics. With only that information, two hypotheses can be drawn about what it is happening: one possibility is that k_2 and some of the spherical harmonics coefficients are strongly correlated and their effects compensate for each other (discussed a bit later in this section and in Section 2.3), and the other one is that there are other parameters, like the empirical accelerations for instance, that dominate the fit's Doppler signal, in some sense overfitting the input data (see Section 2.4). These hypotheses are not mutually exclusive, and it could well be the case that both issues are affecting the solution.

These two guesses at the cause for the obtained estimation results are further supported by Fig. 2 showing the residuals for flyby T074. On the one hand, the residuals are reasonably small when compared to the expected effect on the Doppler signal that the different coefficients would have (about 9 mHz RMS when the expected contribution from spherical harmonics is in the order of hundreds of milihertzs, see Fig. 13 in Section 3.1). If no overfitting is taking place, then these small residuals and the different spherical harmonics solutions obtained by the different studies would be explained by the existence of a strong correlation between the gravity field parameters. On the other hand, there is still an unmodelled signal left that can be seen in the residuals, and this shape of the residuals is the same in both cases, with and without k_2. This result favours that idea that, if there is no strong correlation between the gravity coefficients and yet they are so different and the residuals so small and with the same shape, the fit is dominated by other parameters that mask any real estimation of the gravity field, with the empirical accelerations as the best candidates for this. It must be noted that T074 is shown here as an example, but the same behaviour described here can be observed in the residuals of all the flybys.

(a)

	μ	J_2	C_{22}	S_{22}	J_3
μ	1.0	-0.092	-0.149	0.183	0.007
J_2	-0.092	1.0	0.587	-0.053	0.122
C_{22}	-0.149	0.587	1.0	-0.305	-0.012
S_{22}	0.183	-0.053	-0.305	1.0	0.284
J_3	0.007	0.122	-0.012	0.284	1.0

(b)

	μ	J_2	C_{22}	S_{22}	J_3	k_2
μ	1.0	-0.044	-0.066	0.07	0.037	0.055
J_2	-0.044	1.0	0.986	0.785	-0.747	-0.994
C_{22}	-0.066	0.986	1.0	0.769	-0.757	-0.997
S_{22}	0.07	0.785	0.769	1.0	-0.711	-0.786
J_3	0.037	-0.747	-0.757	-0.711	1.0	0.76
k_2	0.055	-0.994	-0.997	-0.786	0.76	1.0

Figure 3: Correlation matrix for relevant gravity field parameters when **(a)** the Love number k_2 is not estimated and **(b)** k_2 is estimated.

The fact that there is a strong correlation between parameters can be assessed by looking at the correlation matrix of the estimated parameters. Fig. 3 displays the correlation matrices of the two cases studied here. As it can be seen, the existence of an intrinsic high correlation within the problem can be confirmed indeed. When no constraint is put on k_2, all parameters become

strongly correlated with each others except for the gravitational parameter μ. The correlation is especially important in the case of J_2, C_{22} and k_2, to the point that it could be said that these parameters are dependant on each other. This is what is being manifested in the unconstrained solution in Tab. 2, where the large and negative k_2 drives J_2 and C_{22} to positive values one order of magnitude larger. By looking at the correlation matrix in the constrained solution it becomes clear that it is k_2 what was mainly causing the coupling between parameters, as only a small significant correlation between J_2 and C_{22} can be found there.

In conclusion, the estimation setup using GEODYN presents an underlying strong correlation between parameters and a tendency towards an unphysical negative value for the second degree Love number. Constraining k_2 solves the correlation problem but then information is lost about such an important parameter. Not only that, but it would also leave unattended the unknown and concerning cause for the correlation and insensibility of the residuals to the gravity field parameters, as a non ill-defined problem should not display this behaviour. If the solution with a negative value for the Love number is just a local minimum, way to steer the solution towards values that are physically meaningful has been developed in this work, as explained in the next section.

2.2 Inequality constraints

Usually in an estimation problem imposing constraints can be very useful to reduce correlations and uncertainties, provided that those constraints add valid real information to the problem. Such constraints could range from a priori values to relationships like Kaula's rule (Eq. 1.4) or the hydrostatic ratio of $J_2/C_{22} = 10/3$ (if there are valid reasons to apply them). These relationships can be expressed in terms of arbitrary (differentiable) constraint equations

$$c(\mathbf{x}) = \mathbf{0} \tag{2.1}$$

The set of constraint equations can be linearised as

$$\mathbf{0} = c(\mathbf{x}) + \frac{\partial c}{\partial \mathbf{x}}(\mathbf{x})\Delta\mathbf{x} \Longrightarrow -c(\mathbf{x}) = C(\mathbf{x})\Delta\mathbf{x} \tag{2.2}$$

and incorporated into the problem equations (Eq. 1.13) as

$$\begin{bmatrix} \Delta\mathbf{y} \\ -c(\mathbf{x}) \end{bmatrix} = \begin{bmatrix} H(\mathbf{x}) \\ C(\mathbf{x}) \end{bmatrix} \Delta\mathbf{x} + \begin{bmatrix} \boldsymbol{\epsilon} \\ \boldsymbol{\eta}_c \end{bmatrix} \tag{2.3}$$

Other times, there might be the need of using inequality constraints. In this case, as it is known for certain that $k_2 > 0$, the parameters can be selectively constrained during each iteration, searching for other potential minima where k_2 is naturally positive and, hopefully, not strongly correlated with other coefficients. This formulation for this kind of constraints is introduced in this study and can be expressed as

$$c_i(\mathbf{x}) \leq \mathbf{0} \tag{2.4}$$

The fact that these are a set of inequalities raises the question of how they can be incorporated into the problem. We propose to implement this constraint by classifying after an estimation iteration which inequality constraints have been violated (denoted by c_i^*), that is to say

$$c_i^*(\hat{\mathbf{x}}) > \mathbf{0} \tag{2.5}$$

and recomputing the previous estimation iteration with the active inequality constraints incorporated into the equations as equality constraints:

$$\begin{bmatrix} \Delta\mathbf{y} \\ -c(\mathbf{x}) \\ -c_i^*(\mathbf{x}) \end{bmatrix} = \begin{bmatrix} H(\mathbf{x}) \\ C(\mathbf{x}) \\ C_i^*(\mathbf{x}) \end{bmatrix} \Delta\mathbf{x} + \begin{bmatrix} \boldsymbol{\epsilon} \\ \boldsymbol{\eta}_c \\ \boldsymbol{\eta}_{ci}^* \end{bmatrix} \tag{2.6}$$

where C_i^* comes from the linearisation of the active constraints, in other words, $C_i^* = \partial c_i^* / \partial \mathbf{x}$. Then, following Eqs. 1.21 (Section 1.1) and Eq. 2.6, the normal equations become

$$\left(\sum_{i=1}^{N_{\text{flybys}}} H_i^T P_{y,i}^{-1} H_i + C^T P_c^{-1} C + C_i^{T*} P_{ci}^{*-1} C_i^* \right) \Delta \hat{\mathbf{x}}_{(n)} = \sum_{i=1}^{N_{\text{flybys}}} H_i^T P_y^{-1} \Delta \mathbf{y}_{i,(n)} - C^T P_c^{-1} c - C_i^{T*} P_{ci}^{*-1} c_i^* \quad (2.7)$$

In the previous equation, P_c and P_{ci}^* are the covariance matrices of the equality and active inequality constraints respectively, which govern how strictly those constraints are imposed on the solution.

An alternate possibility to this approach would be to directly impose the active inequality constraints on the parameters, reducing the number of parameters as relationships are included, forcing the solution to lay exactly at the boundary defined by those constraints within the parameter space. That method is more numerically stable when dealing with matrices with unfavourable condition numbers. It, however, comes at the cost of being more difficult implement, whereas with the procedure just described the constraint normal matrices can just be added directly to the normal equations, as can be seen in Eq. 2.7. As long as a suitable routine for matrix inversion (like Cholesky decomposition) is utilised, the associated variance of the active inequality constraints can be increased iteratively until the inequality is met (or at least the solution is close to the boundary within a certain margin of tolerance). This was the algorithm developed for the inequality constraints that were tested with the GEODYN setup. The method can be proven to be mathematically equivalent to the approach of reducing the number of parameters by substituting the equations (as long as they are compatible) in the limit where $\sigma \to 0$ (in P_{ci}^*).

2.3 Tests with inequality constraints

In order to check the possibility that the inability to estimate a positive value for k_2 is caused by the estimation loop reaching a local minimum, an inequality constraint on k_2 was incorporated into the procedure for solving the global normal equations. Initially only the constraint of making k_2 positive was tested, but it soon became clear that it was not enough for leaving the dominion of influence of the attractor previously found in the unconstrained estimation driving k_2 towards negative values. As it can be seen in Tab. 3, in the case where the $k_2 > 0$ constraint is used, the value for the Love number just stays at the boundary of the dominion, providing the same estimation results as when $k_2 = 0$ (Tab. 2).

Thus, to try to escape from the attractor larger and larger values for k_2 were tested, and the results are also presented in Tab. 3. It can be noticed that this was done to no avail, as in all cases up to $k_2 > 0.8$ the value for the Love number always tries to be as negative as possible, resulting in it staying at the boundary marked by the inequality constraint. As a note, the gravity field coefficients show important change in the interval of k_2 that was tested, meaning that $k_2 > 0.8$ can be considered a big Love number in the Titan problem and the last value tested is adequately large. This means that the attractor is really strong, and this also manifests in the fact that the correlation between k_2, J_2 and C_{22}, represented in Fig. 3, still remains. It can be observed in the results that both J_2 and C_{22} present a clear linear trend with respect to k_2, both decreasing as k_2 increases, as anticipated by the negative values in the correlation matrix previously shown. In all cases the correlation matrix is equivalent to that of the case where k_2 is not estimated, as the solution converges to the boundary resulting in the variance for k_2 going to zero.

If the focus is set in the residuals, it can be seen that they are practically the same in all cases.

Case	$k_2 > 0$	$k_2 > 0.3$	$k_2 > 0.6$	$k_2 > 0.8$
μ (km^3/s^2)	8978.0285 ± 0.0130	8978.0288 ± 0.0130	8978.0291 ± 0.0130	8978.0293 ± 0.0130
k_2	0.000 ± 0.000	0.300 ± 0.000	0.600 ± 0.000	0.800 ± 0.000
$J_2 \times 10^6$	30.383 ± 1.532	24.264 ± 1.532	18.144 ± 1.532	14.065 ± 1.532
$C_{21} \times 10^6$	-4.283 ± 0.796	-4.435 ± 0.796	-4.586 ± 0.796	-4.687 ± 0.796
$S_{21} \times 10^6$	13.745 ± 1.225	14.089 ± 1.225	14.434 ± 1.225	14.664 ± 1.225
$C_{22} \times 10^6$	7.772 ± 0.501	4.818 ± 0.501	1.863 ± 0.501	-0.107 ± 0.501
$S_{22} \times 10^6$	-1.706 ± 0.459	-1.975 ± 0.459	-2.244 ± 0.459	-2.424 ± 0.459
$J_3 \times 10^6$	1.399 ± 2.201	2.659 ± 2.201	3.919 ± 2.201	4.759 ± 2.201
RMS residuals	5.209 mHz	5.219 mHz	5.230 mHz	5.237 mHz

Table 3: Estimated values for the spherical harmonics coefficients of the gravity field of Titan and their 1-σ errors from the GEODYN model with different inequality constraints in the Love number k_2.

Thus, as with the correlation matrix, the residuals are extremely insensitive to the spherical harmonics coefficients. They only increase very slightly with k_2, which makes sense when considering that they grow when moving away from the attractor. The plots of the flyby residuals also look the same as in the previous cases, maintaining shape and magnitude. Consequently, if the correlation between parameters cannot a priori be resolved with those inequality constraints and the quality of the fit does not really respond to the spherical harmonics coefficients, then the next step is to test whether the solution is being dominated by other parameters that are masking the real values for the gravity field of Titan.

2.4 Effect of empirical accelerations

The empirical accelerations, used in orbit determination problems to absorb dynamical mismodelling, are versatile by nature and purpose and as such should be handled with care because they can pollute the estimation if they are not properly constrained or they couple with other parameters. For that reason they could explain the overfitting and absorbing the true signal for the spherical harmonics. As mentioned before, in the GEODYN model they were implemented as constant in the RSW frame during eight-hour intervals in each of the flybys. For the tests presented in this section they are removed from the estimation altogether to check their influence in the solution and residuals.

The results without estimating k_2 and constraining k_2 to be positive are presented in Tab. 4. As they are, they have no sensible physical meaning, except for the gravitational parameter, which is reasonably estimated. It can be seen in both cases that J_2 is negative, implying that Titan is prolate instead of oblate, which is something not expected for a large spinning moon with tidal interactions nor consistent with the measured topography of Titan (Corlies et al., 2017). In the same line of reasoning, it is also hard to expect that C_{22}, associated to the equilibrium tide would be negative (meaning that the tidal bulge is repelled), that J_3 would be greater in magnitude than J_2 and S_{21} to just be so large. A really interesting consequence of removing the empirical accelerations is that then the solution is attracted towards a positive value for k_2, quite a large one.

However, what is most relevant of this results are the extremely large residuals, in the hundreds of milihertzs which, as previously stated, it is in the realm of the expected magnitude of the

Case	$k_2 = 0$	$k_2 > 0$
μ (km^3/s^2)	8978.1726 ± 0.0035	8978.1738 ± 0.0035
k_2	-	7.214 ± 0.471
$J_2 \times 10^6$	-10.444 ± 1.124	-156.829 ± 9.631
$C_{21} \times 10^6$	-76.382 ± 0.610	-80.605 ± 0.667
$S_{21} \times 10^6$	234.052 ± 0.997	241.110 ± 1.119
$C_{22} \times 10^6$	-16.569 ± 0.367	-87.370 ± 4.644
$S_{22} \times 10^6$	-7.856 ± 0.354	-14.271 ± 0.539
$J_3 \times 10^6$	-229.031 ± 1.946	-195.600 ± 2.810
RMS residuals	334.3 mHz	334.4 mHz

Table 4: Estimated values for the spherical harmonics coefficients of the gravity field of Titan and their 1-σ errors with and without constraining the second degree Love number k_2 and not including empirical accelerations in both cases.

contribution to the Doppler signal from Titan's dipole field (Fig. 13). This fact confirms the idea that the empirical accelerations are dominating the solution. Although is true that the empirical accelerations, when serving their purpose, could absorb mismodellings, in this case they reveal that there is a serious signal component unaccounted in the model. Given how highly correlated the coefficients were in the estimations with empirical accelerations, this model mismatch is unacceptable if the obtained spherical harmonics are to be considered realistic. The previously estimated empirical accelerations were in the order of 10^{-7} m/s^2, several orders of magnitude larger than those from similar Cassini navigation studies (Boone et al., 2017; Di Ruscio et al., 2020). Looking at Fig. 4 is revealing, as it shows how the residuals are generally linear in time. Again, their shape and overall magnitude is not conditioned by the estimated coefficients. This linear trend in Doppler, which can be translated into spacecraft relative velocity towards the observer, represents a constant, relatively large acceleration on Cassini. A possible explanation for these results is given in Section 3.2.8; it could be related to how the spherical harmonics of Saturn are modelled. The only exception to this trend is during the closest approach to Titan, where some signal, presumably from the actual real gravity field of Titan, shows up. Thus the signal from Titan seems to be present, but the estimation filter cannot properly capture it as it fails to also compensate the large trend when no empirical accelerations are considered.

The fact that the shape of the residuals does not depend on the coefficients is a hint once again about the parameters being still highly correlated. Observing the correlation matrices in Fig. 5 for the two tests discussed in this section it can be confirmed that, without the constraint in k_2, the parameters get strongly coupled. The two correlation matrices shown here are almost identical to the ones displayed in Fig. 3. All of this means that the underlying correlation is worse that previously hypothesised, as it persists even after removing the great buffer for mismodelling that were the empirical accelerations, suggesting that the correlation is deeply rooted into the problem configuration. This correlation when setting k_2 free will be further studied in Chapters 3 and 4 and is not presented in the previous studies by Durante et al. (2019) and van Noort (2021).

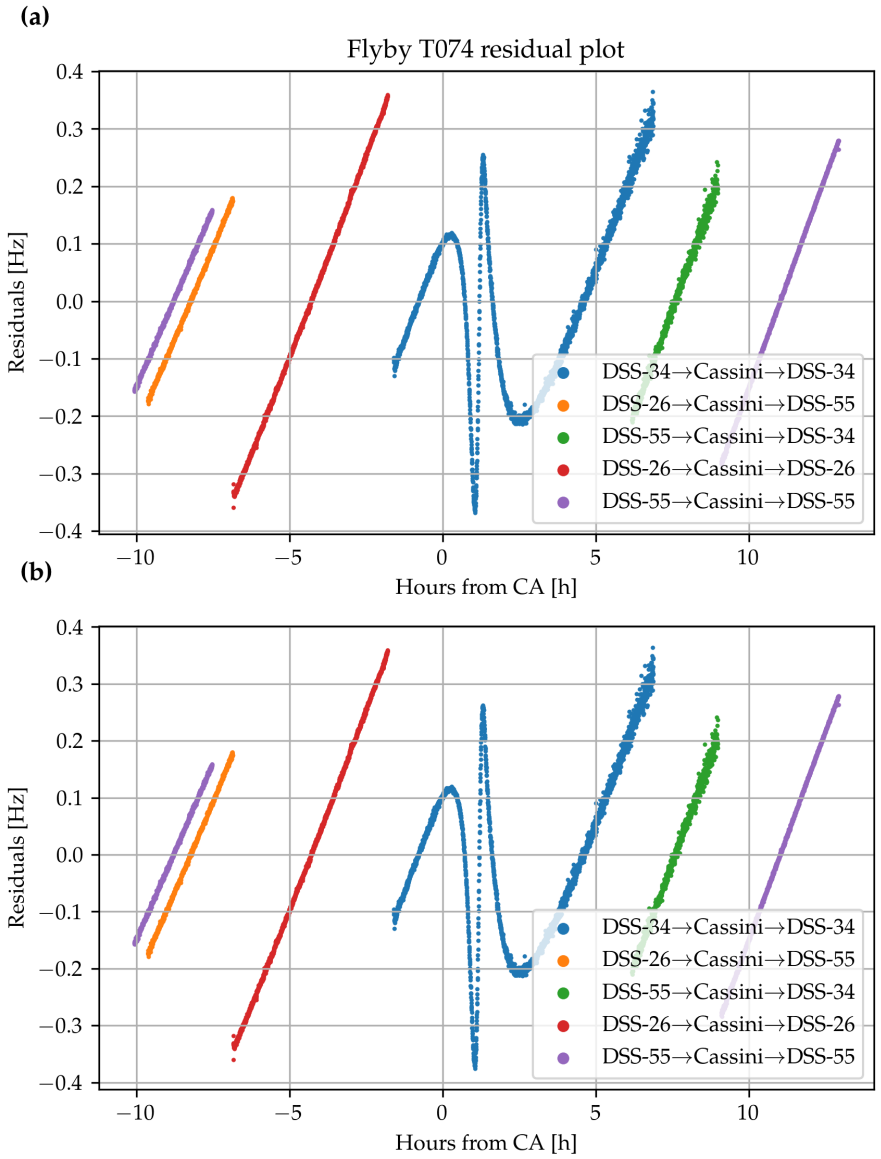

Figure 4: Doppler residuals for flyby T074 for **(a)** the case with null Love number k_2 and **(b)** unconstrained k_2. The shape and magnitude (151.7 mHz vs. 151.8 mHz RMS respectively) of the residuals is almost identical in both cases despite the large difference in estimated coefficients. Closest approach takes place at 16:04, February 18, 2011.

2.5 Effect of tidal lag estimation

Even though it still would not address the unaccounted constant acceleration described in the previous section, here the possibility that not estimating the phase of the second degree Love number (the lag of the tidal bulge due to internal dissipation) might be behind the strong correlation in the dipole field is briefly explored.

Tab. 5 shows the results after ten iterations when estimating the phase lag of the tidal bulge χ_2. After each iteration the 2π modulo of χ_2 was taken in order to ensure that it met the condition that

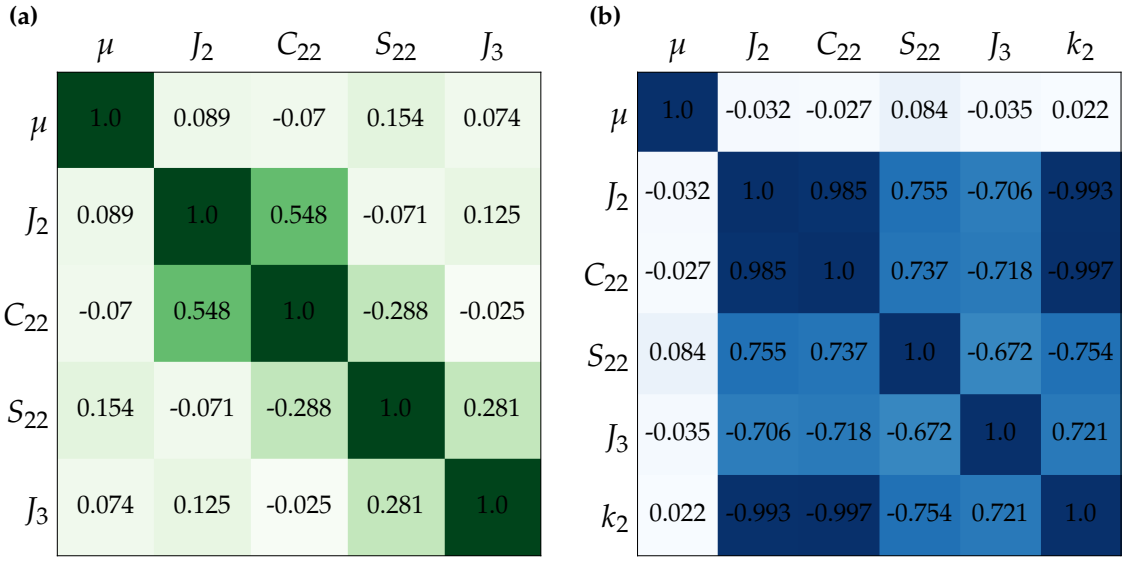

Figure 5: Correlation matrix for relevant gravity field parameters when the empirical accelerations are removed and **(a)** the Love number k_2 is not estimated and **(b)** k_2 is estimated.

Case	**With empirical accelerations**	**No empirical accelerations**
	$\mathbf{0 \leq \chi_2 < 2\pi^*}$	$\mathbf{0 \leq \chi_2 < 2\pi^*}$
μ **(km^3/s^2)**	8978.0175 ± 0.0130	8977.8807 ± 0.0035
k_2	0.000 ± 0.000	0.000 ± 0.000
χ_2 **(deg)**	122 ± 52883	-0.303 ± 0.015
$J_2 \times 10^6$	30.322 ± 1.724	-63.473 ± 1.308
$C_{21} \times 10^6$	-2.606 ± 0.806	-57.083 ± 0.614
$S_{21} \times 10^6$	-0.243 ± 1.282	186.777 ± 1.039
$C_{22} \times 10^6$	12.003 ± 1.260	-23.202 ± 1.140
$S_{22} \times 10^6$	-5.587 ± 5.789	113.770 ± 4.137
$J_3 \times 10^6$	15.496 ± 2.228	-258.729 ± 1.982
RMS residuals	7.485 mHz	344.7 mHz
***the tests with free χ_2 did not converge.**		

Table 5: Estimated values for the spherical harmonics coefficients of the gravity field of Titan and their 1-σ errors obtained at the tenth iteration when testing freeing the phase of the second degree love number.

$0 \leq \chi_2 < 2\pi$. As it can be noticed, the estimation of χ_2 does not solve the problem of unreliability of the estimated coefficients, it actually makes it worse as the results from the iterations do not converge and now k_2 tends towards negative values in the test without empirical accelerations. An interesting feature that can be observed is that the estimated phase is unstable (not exactly divergent because the modulo is taken) in the case with empirical accelerations, while it is bounded and small when not estimating them. However, it has a negative value, which would mean that

the bulge is going ahead instead of lagging, something unphysical. No explanation for this has been found, butit is probably related to the uncompensated linear trend found in the residuals (Fig. 4). The residuals increase only slightly compared to previous tests, again, confirming the conclusion that the quality of the fit is not dominated by the gravity coefficients.

To conclude this chapter, anomalies have been found in the solutions obtained with the GEODYN setup from van Noort (2021). The two important problems that put a risk on the prospects of obtaining a robust solution and that have been identified are the strong correlation between parameters and the dominant nature of the empirical accelerations. The first issue drives the solution towards attractors physically unfeasible in both cases with and without empirical accelerations. The inequality constraints proposed and tested here do not solve the correlation, nor omitting the empirical accelerations with their dominant effect, suggesting that the coupling between parameters already at the dipole field level is deeply rooted into the model definition. The second difficulty which concerns the empirical accelerations has been determined to arise from a large constant acceleration that can be observed in the Doppler residuals and that the model cannot compensate. Thus, the source for this important mismodelling needs to be searched for and understood, as well as the cause for the strong correlation between parameters, in order to improve the GEODYN model and obtain a robust, physically grounded, solution. This will be explored further in the next chapter with the use of simulated data.

3 Verification with simulated data

The focus of this chapter is set in describing the process followed for verifying the estimation setup with GEODYN, after discovering the problems from the previous chapter that the GEODYN model presented in terms of correlation between parameters and the considerable acceleration mismatch that forced the empirical accelerations to dominate the fit. With that goal in mind, the starting point was generating simulated data so then it could be tested how well the chosen virtual gravity field coefficients were determined by the GEODYN setup. The inconsistencies between the simulated gravity field and the estimated one have been be explored in the hopes of finding there the root for the undesirable behaviour the estimation filter was displaying.

3.1 Generation of simulated data

The first step in the setup verification process was to generate simulated data and attempt to reconstruct the gravity parameters with GEODYN. To ensure that the verification setup was as close to the real one as possible, the simulated flybys that were considered are analogues to the real ones, thus presenting the same geometry of Titan coverage. Apart from a fine-tuned dynamical model with all the force contributions relevant at the dipole field level, the relativistic effects on the Doppler observables were carefully considered, as they have an important effect as it will be discussed. After that, different sets of simulated observables and gravity fields were generated.

3.1.1 Simulated flybys

For the task of computing the perturbed orbit for the simulated data, the Tudat astrodynamics libraries developed at TU Delft (see appendices in Dirkx et al., 2019) were used in combination with NASA's SPICE Toolbox (Acton, 1996) and the corresponding SPICE kernels in order to extract the ephemeris for Cassini, Saturn's moons, the planets and the DSN antennae, as well as other ancillary data for analysis of the Cassini mission. The SPICE kernels have been retrieved from the Planetary Data System's Navigation and Ancillary Information Facility archive.

As just mentioned, the problem's dynamical model was constructed using the Tudat functions and tools. In this model, the acceleration sources relevant at the level of Titan's dipole field were considered (see Tab. 1). Apart from the virtual gravity field of Titan, these forces included Saturn's zonal spherical harmonics up to degree eight, Saturn's seven largest moons after Titan, Jupiter and the Sun. The values used for Saturn's harmonics are the same as the ones used in the GEODYN setup and they come from the estimation performed by Iess et al. (2019) with data from Cassini's last orbits around Saturn. Many of these gravitational interactions are not relevant for estimating the low degrees, but they were included nevertheless for convenience, ease of implementation and consistency with the GEODYN model. Other forces like atmospheric drag, RTG emissions and solar radiation pressure were not added to the model, although they can be certainly relevant

when estimating higher harmonics, as they are not necessary for these verification purposes (also drag and radiation pressure should be estimated as null by GEODYN in any case).

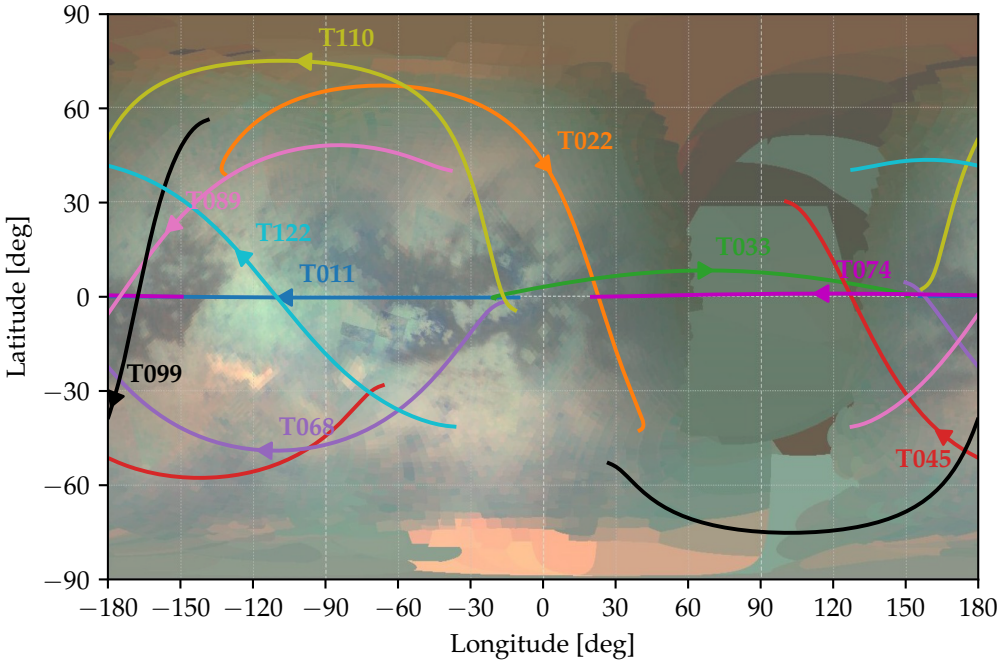

Figure 6: Ground tracks of the different simulated Cassini flybys with the point of closest approach and direction of the orbit. Twelve-hour long arcs are considered. The initial states were retrieved from the Cassini SPICE ephemeris and then the perturbed orbits propagated.

Flyby	CA time	Altitude	Latitude	Longitude	SEP angle
T011	08:25 27 Feb. 2006	1812 km	0.2°S	255.6°E	150.2°
T022	10:05 28 Dec. 2006	1297 km	45.4°N	355.9°E	130.6°
T033	17:00 29 June 2007	1933 km	8.4°N	63.1°E	46.4°
T045	02:13 31 July 2008	1614 km	43.5°S	162.7°E	30.0°
T068	03:24 20 May 2010	1397 km	48.9°S	241.1°E	120.3°
T074	16:04 18 Feb. 2011	3651 km	1.0°N	113.4°E	131.2°
T089	01:56 17 Feb. 2013	1978 km	21.0°N	203.1°E	106.0°
T099	16:27 06 Mar. 2014	1500 km	31.1°S	181.0°E	111.0°
T110	14:30 16 Mar. 2015	2274 km	74.8°N	263.1°E	108.6°
T122	08:31 10 Aug. 2016	1698 km	12.4°N	234.4°E	112.7°

Table 6: Time, minimum altitude reached, latitude and longitude of the point where that close approach took place and Sun-Earth-Probe (SEP) angle for different Titan flyby arcs. Values taken from Durante et al. (2019) and van Noort (2021).

The simulated flybys were configured to emulate the real ones. To achieve that, the initial state for Cassini is extracted from the spacecraft's SPICE ephemeris six hours prior to the time of closest approach to Titan. Then the orbit is propagated with ten second steps up to six hours after the closest approach, the simulated arc covering twelve hours in total. The reason why ten second steps where selected is in order to match with the real data, used in the tests in the previous chapter, which had the same time interval between points. The ground tracks of all the flybys

can be seen in Fig. 6, where the point of closest approach and direction of the orbit have also been marked. The reference time at which that point is considered to be reached (so the orbit integration starts six hours prior) can be seen in Tab. 6 and it is used in the plots in this document in general to reference the time coordinate for each flyby. Tab. 6 also shows the altitude, latitude, longitude and Sun-Earth-Probe angle of the closest approach. The last piece of information is important when taking into account how noisy the real data would be expected to be because of interplanetary plasma interactions. Returning to Fig. 6, it can be seen that coverage at the polar regions is poor, something that poses a challenge when trying to get information from those regions, but at least there is some variety in terms of inclinations and longitudes, beneficial for reducing the correlation between parameters. How good the flyby geometry really is at a fundamental level will be explored in Chapter 4.

Once the orbit is computed, the next step is to generate the observables. With the Tudat-based software implemented here for the tracking data simulation it is possible to generate different types of measurements like one-way, two-way and three-way Doppler or relative velocity. For the verification tests described in this chapter, two-way Doppler measurements transformed into relative velocities through Eq. 1.33 were used (because of implementation issues regarding feeding the simulated data to GEODYN). The data can also be generated with different relativistic effects taken into account, which will also be useful for the verification, as it will be seen. No plasma, ionospheric or tropospheric perturbations have been modelled, despite being potentially relevant, as they can be turned off in GEODYN. As such, the two-way Doppler shift produced in all the flybys is displayed in Fig. 7. If attention is briefly paid to Fig. 13 showing the contributions of the gravity coefficients to the Doppler signal it is possible to get the idea of how small their expected effect is ($\sim 10^{-1}$ Hz), first, compared to just the orbital velocity of Cassini around Saturn and the relative velocity between Saturn and the Earth ($\sim 10^{6}$ Hz) and, second, the signal from the deflection from the Titan gravity assist ($\sim 10^{4}$ Hz). A phenomenon that can be well observed in Fig. 7 is how the shift in velocity in the hyperbolic orbit from before and after encountering Titan manifests in Doppler data of all flybys around an hour and a half after the time of closest approach. As can be guessed, this is a result from the light-time delay between Saturn and the Earth, which has to be calculated iteratively for both the uplink and downlink. The closest approach appears as a spike in the Doppler shift in some of the flybys, as orbital velocity increases near the moon, while in other flybys it can be better described as just a slope. This variability in shape of the signal can be attributed to the orientation of the hyperbolic trajectory relative to the Earth, and it serves to illustrate the point that the trajectory relative to Titan is not the only important factor regarding how favourable for estimation is the overall geometry of the flybys.

At this point it might have been noticed how the Doppler curve from flybys T110 and, especially, T089 cover a smaller time period. The reason behind this is in the way the simulated observations are generated: for each data point, the inclination with respect to the horizon of the light propagation vector is checked to ensure it is 15° over the horizon at both transmission and reception on Earth. This means unfortunately that no complete coverage of the closest approach can be attained for those two flybys when only considering two-way Doppler (same transmitting and receiving antennae). It should be mentioned that only three DSN antennae were considered for the simulated data: DSS-14, DSS-43 and DSS-63, each one chosen arbitrarily form each of the DSN complexes, but representing the real visibility conditions from Earth for the flybys. The minimum elevation requirement was not only set to replicate the physical limitations of the true data, but it is also useful for preventing numerical issues with the light-time equations solver when taking into account relativistic effects, where the Earth crossing the path of the radio signal leads to a singularity. This last consideration brings the discussion towards the next relevant topic.

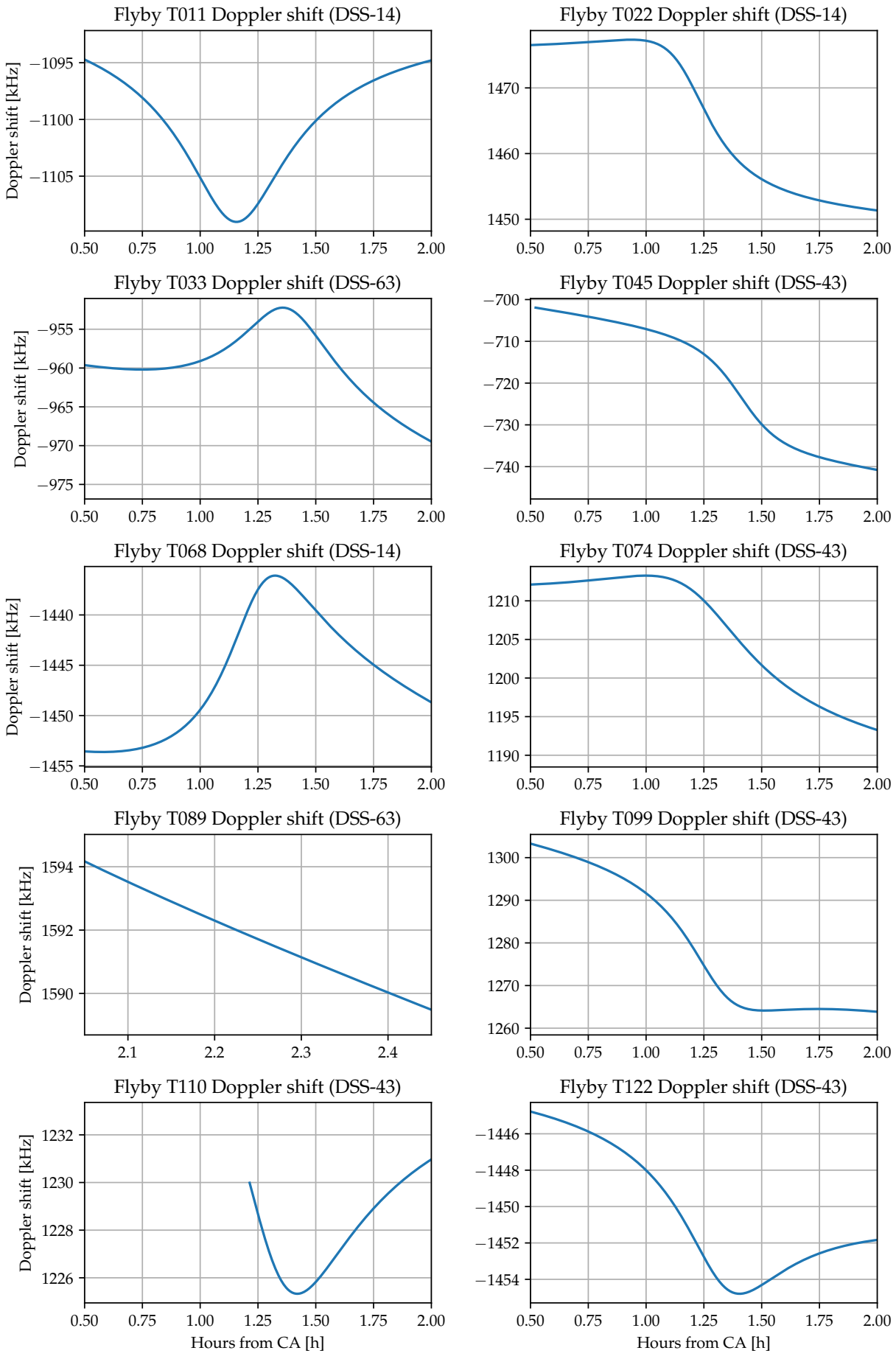

Figure 7: Received two-way Doppler shift signal for the different simulated flybys.

3.1.2 Magnitude characterisation of relativistic effects

An important part of measurement modelling are the relativistic effects that can affect the Doppler observables. This is in contrast with the case of the spacecraft's orbit, where these effects play an extremely minor role. As previously discussed in Section 1.2, in a precise orbit determination problem like this one, both special and general relativity can have a noticeable impact in the received frequency of the radio signal. As a reminder, the general relativistic effects can be decomposed into three: the frequency drift, which can be regarded as a gravitational redshift caused by leaving a body's gravity well (blueshift if entering), the geodesics of the curved space-time, which affects the perceived relative velocity, and the additional time delay, a result of the increased light-path because of the non-flat space-time geometry. Consequently, the objective of this subsection is not only to explain which phenomena has been taken into account in the software for the simulation of the observables that has been implemented for this study, but to also show as a result what is their calculated effect on the Doppler signal.

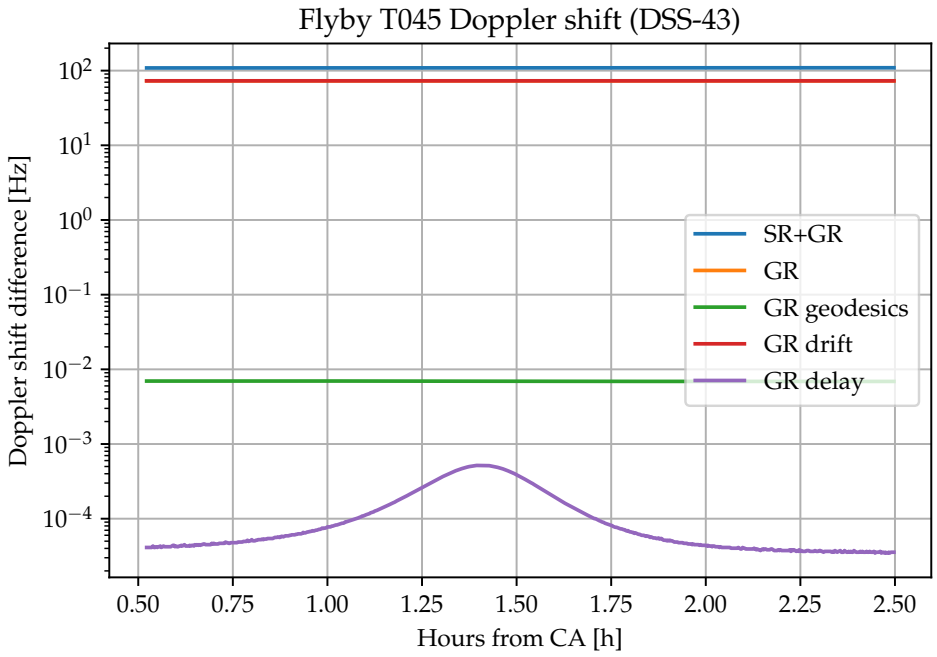

Figure 8: Comparative magnitude of different relativistic effects on one-way Doppler observables, computed as the difference between the nominal curve with all the effects and the signal without the respective ones. The line corresponding to the overall general relativistic effect is behind the drift curve.

The magnitude of the different relativistic contributions to the signal when considering one-way measurements, just one trip from Cassini to the ground station, is displayed in Fig. 8 as a function of reception time. A nominal orbit with all the relativistic effects, including those from Titan, Saturn, the Jovian system, the Sun, Moon and Earth, was computed and, by evaluating the difference in signal when omitting the respective contributions, the magnitude of the effects characterised. As it can be observed, if all relativistic effects were to be disregarded completely, an unacceptable large modelling error in the order of 100 Hz would be committed. The signal from just the general relativity is close behind and it overlaps with the one from the gravitational frequency drift, revealing that it is the most important general relativistic effect when it comes to one-way observables. After that, geodesics and the time delay have the smallest impact. Looking at Fig. 9 with the contribution of each considered body (through general relativity) to the Doppler signal, it can be seen how the Sun has by far the largest contribution, being so massive and, thus, being the change in the gravitational well from the Saturnian System to the Earth so relevant. Afterwards, Saturn and Jupiter have a significantly smaller but potentially non-negligible influence,

followed by the Earth. The effect from Titan and the Moon is so small that it is just dominated by erratic numerical rounding error, as it can be seen.

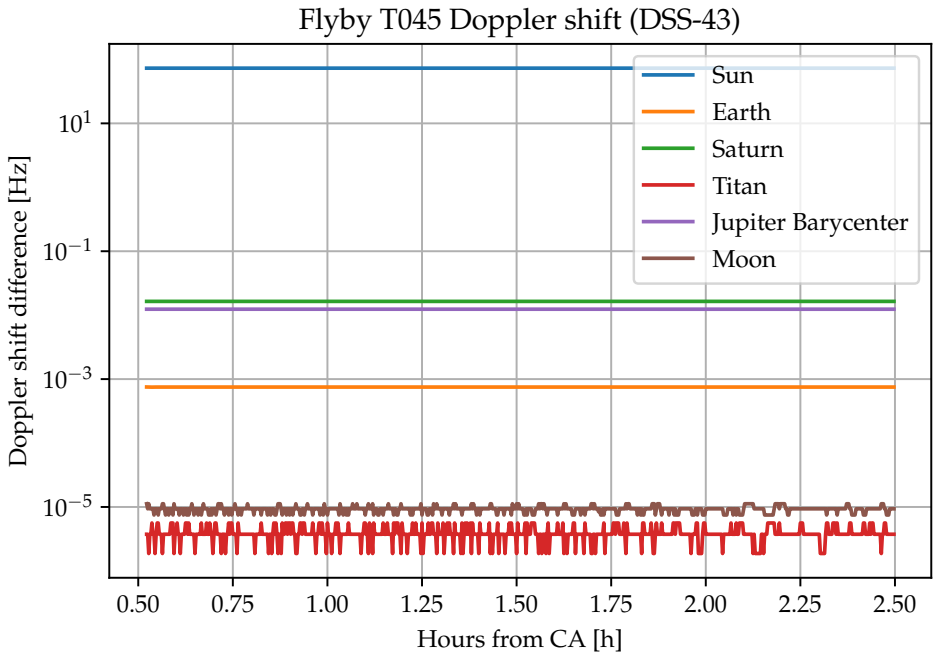

Figure 9: Comparative magnitude of different relativistic effects on one-way Doppler observables, computed as the difference between the nominal curve with all the effects and bodies and the signal without the respective body.

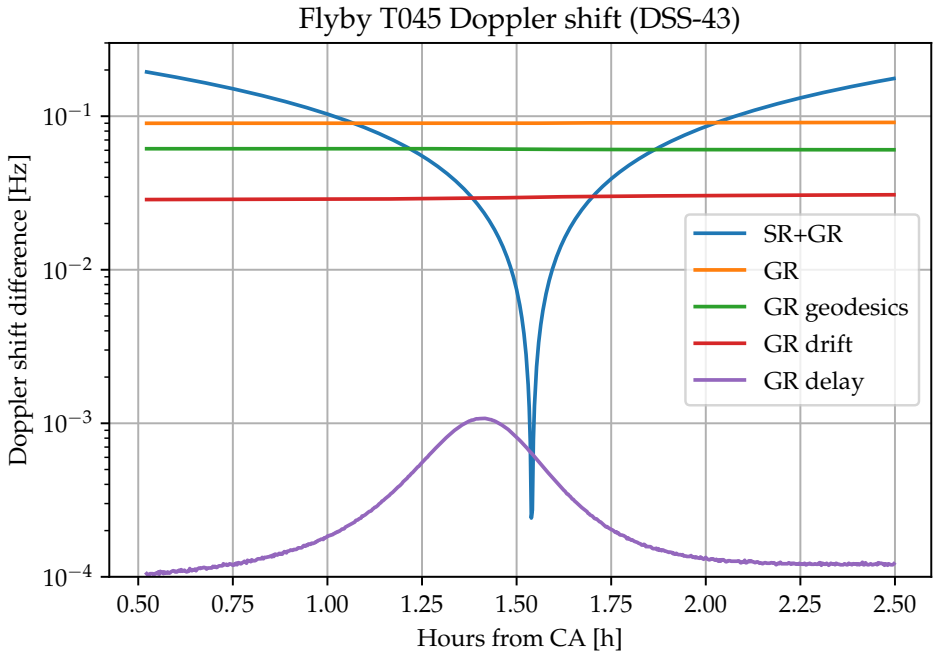

Figure 10: Comparative magnitude of different relativistic effects on two-way Doppler observables, computed as the difference between the nominal curve with all the effects and the signal without the respective ones.

Something notable that purposely has not been discussed until now is how the relativistic delay curve is the only one in Fig. 8 that shows a significant change in magnitude and it does so precisely during the closest approach to Titan (as depicted in Fig. 7 it manifests in the data after close to an hour and a half). At first glance this might seem contradictory with the results displayed in Fig. 9, where it was clear that any contribution from Titan is below the numerical noise level. What this is revealing is a fundamental element of an orbit determination problem of this nature: the importance of precise timing. Unlike special relativity and the general relativistic drift, the time delay is not affecting physically the frequency of the radio waves but instead is causing the signal to arrive at a slightly later time. However, if this delay is not accounted for, a difference can appear when comparing the two signals at equal times, especially if the Doppler shift is experiencing a rapid change, exactly what happens close to Titan (as seen in Fig. 7) and explaining how it can indirectly cause the discrepancy. Here the effect is fairly small, but the impact of timing errors will be further explored in Section 4.5.

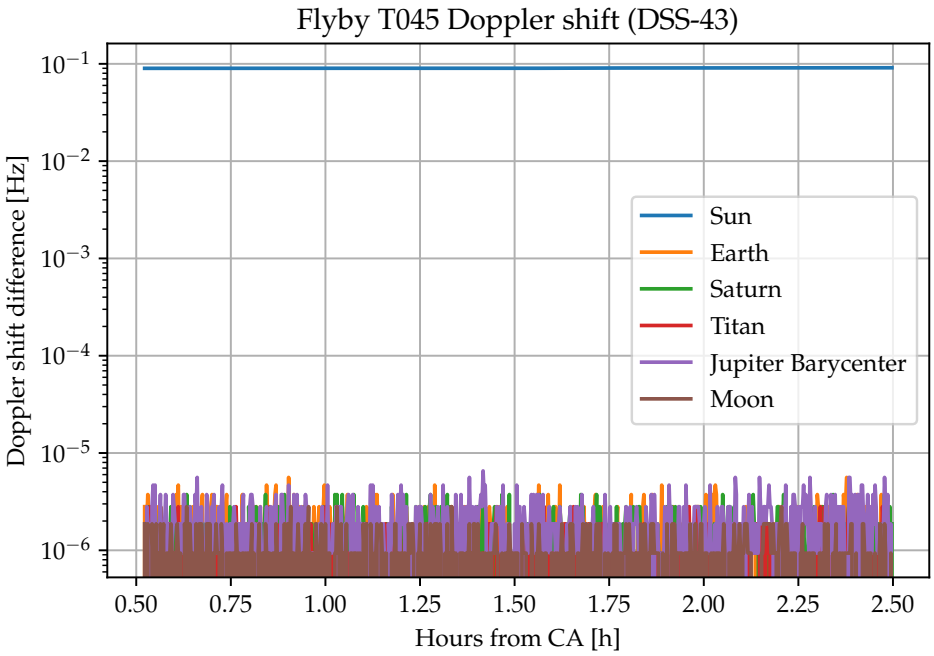

Figure 11: Comparative magnitude of different relativistic effects on two-way Doppler observables, computed as the difference between the nominal curve with all the effects and bodies and the signal without the respective body.

Shifting now attention to Figs. 10 and 11, where the magnitude associated to different relativistic effects and bodies in two-way Doppler data is illustrated, a general reduction in what would be the error if relativistic effects were ignored can be noticed. This fact is one of the strengths of two-way measurements versus one-way ones. Because of the similar geometry of spacecraft, planets and ground stations relative positions and velocities during the uplink and downlink trips, most of the frequency change from the special relativistic Doppler effect and the gravitational redshift cancels out. Nevertheless, as can be regarded in Fig. 10, the mismatch between the two light-paths is still capable of producing a non-negligible frequency shift, relevant at the dipole field level (see Fig. 13). The impact of special relativity is still the largest, and in this particular flyby there is a change of sign in the difference between the signals, hence the downwards spike that can be found in the plot. It must be highlighted how the geodesics and the time delay are an exception and their magnitude is actually larger in two-way observables compared to one-way Doppler, the first effect now becoming the strongest contribution from general relativity instead of the gravitational drift. The reason behind this result is that the curved geodesics lead to observing the spacecraft relative velocity from a slightly different angle, but this effect does not cancel from uplink to downlink, on

the contrary, it actually gets enhanced. The same applies to the time delay, which lengthens the light travel in both trips.

The main outlook that can be drawn from Fig. 11 is that for two-way Doppler data only the general relativistic effect from the Sun is relevant. The contributions from the rest of the bodies just appear as the characteristic rugged curve coming from numerical rounding error. Considering that each body adds two extra relationships and unknowns to the light-time equations (Eqs. 1.23 and 1.24), taking into account more bodies than the Sun just results in higher computational effort with no benefit in precision whatsoever, so they can be disregarded for simulating two-way measurements. Of course, in a more advanced attempt at this problem with data from a future probe it may no longer be the case and more floating point precision would be needed to check that the other bodies do not mix with the higher degree coefficients signal from the gravity field. Last but not least, it should be mentioned that, in order to save an extra computational cost, a fantastic initial guess for light-time time equations for one data point can be taken from the solution for the previous point, if data points are processed sequentially, or just from any of the points in a data sequence if they are processed in parallel (i.e. with a GPU). This is because, as it can be expected, the travel times do not change drastically over a flyby's duration.

3.1.3 Simulated gravity fields

To finish this section, the simulated gravity fields of Titan that were generated for the verification tests are explained here. First, a simple case in which all Titan gravity field coefficients are null (except the gravitational parameter) was simulated as a baseline to which other results can be compared. Titan's gravitational parameter was taken as $\mu = 8978.1388\ \mathrm{km}^3/\mathrm{s}^2$, the value from the SPICE kernel, which sits in between the values provided by Iess et al. (2012) and by Durante et al. (2019). Then four additional gravity fields were simulated: with just the normalised $\overline{C}_{20} = -10^{-5}$ ($J_2 = 22.4 \cdot 10^{-6}$), with $\overline{C}_{22} = 10^{-5}$ ($C_{22} = 6.5 \cdot 10^{-6}$), with $\overline{C}_{30} = 10^{-5}$ ($J_3 = -26.5 \cdot 10^{-6}$) and with $k_2 = 0.6$. In all four cases the rest of the coefficients were equal to zero except for the one being considered. Intentionally, these coefficients have similar magnitudes to the estimated ones that where presented in Chapter 2, so they have comparable associated simulated signals.

As the means for representing the effect from some of the relevant gravity field coefficients, the difference of each of the four simulated parameters and the case in which the gravity field is null has been computed and plotted. The change in relative velocity seen from the observer as well as the impact in the Doppler signal for flybys T011 and T022 are represented side by side in Fig. 12, while the shifts in Doppler data for the rest of the flybys are displayed in Fig. 13. As it can be seen, the specific geometries of the flybys lead to a wide variety of footprints from the gravity coefficients in the Doppler signal. A remarkable feature that can be regarded in Fig. 12 is how the shift in relative velocity corresponds with the change in Doppler with no distinguishable difference (although there actually is a minimal one), just with an opposite sign (see Eq. 1.33), despite the strong effect of the relativistic corrections (remember Fig. 10). In fact, all the difference in Doppler plots for all the flybys were tested to look exactly the same despite not even applying any relativistic effects to the simulated measurements altogether. The implication of the near perfect correspondence with relative velocity and the insensibility of the differences in Doppler to the computation of relativistic effects (not to be confused with the overall Doppler curve which gets well affected by relativity as described in Section 3.1.2) is that the perturbations from the gravity field add linearly to the signal. This is a good sign for obtaining a global solution, because the strong linearity accelerates convergence of the least squares algorithm and guarantees that, given a solution to the problem, no other minima could exist nearby. The result found here serves to explain why the approach of using inequality constraints discussed in Section 2.3 did not work for this problem, as no other minima with a positive k_2 could be found close to the unconstrained

solution because of the strong linearity around the attractor.

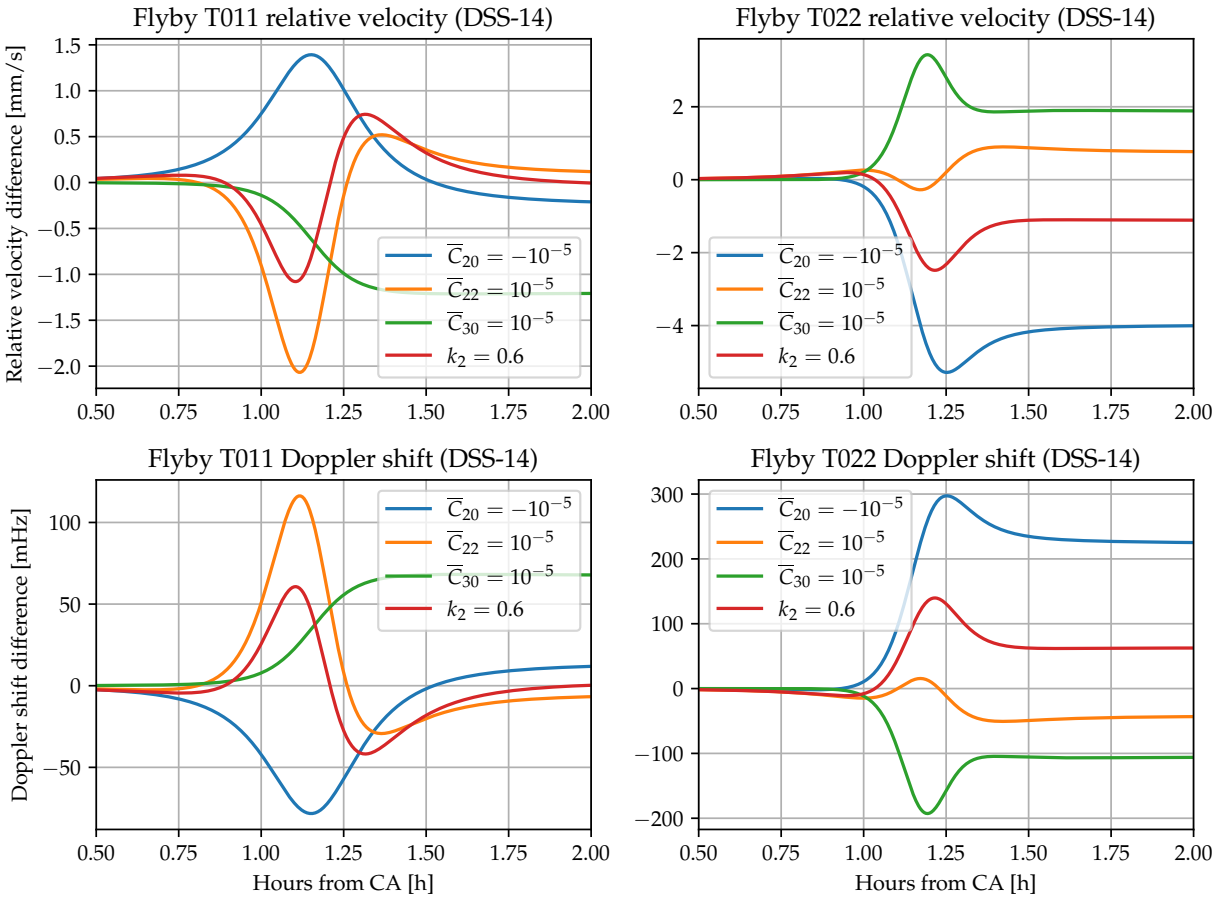

Figure 12: Difference in relative velocity and two-way Doppler data for different simulated gravity field coefficients and flybys T011 and T022. Changes in relative velocity and Doppler show the same curve shapes but with opposite signs.

Looking at all flybys in Figs. 12 and 13 the presence of a strong correlation between the signals arising from C_{22} and k_2 can be established. This is not surprising as k_2 is determining the strength of the response to the periodic changes in the disturbing tidal potential and its leaks into the J_2 field and, most importantly (in relative terms), into the C_{22} field (tidal bulge, see Eqs. 1.7-1.8). Thus, the k_2 is always a combination of the J_2 and C_{22} signals where the latter is dominant. Another interesting feature of the flyby geometry that becomes apparent in these plots is how the low inclination passes (T011, T033 and T074) present less correlation between J_2 and C_{22}/k_2, so they are useful for properly resolving those coefficients, which tend to be strongly coupled (as seen in Chapter 2). This is because low inclination trajectories sweep the low latitude regions where the acceleration from C_{22} and k_2 changes with longitude while the one from J_2 stays constant, giving rise to distinct signals. It can also be noticed that the signal from J_3 shows no spike in those flybys, as the acceleration is applied cross-track, but strong spikes can be seen when the orbit has a high inclination and the point of closest approach is far from the equator. High northern latitude close approaches in T022 and T110 lead to a negative correlation between J_2 and J_3, while flybys in southern latitudes like T045 and T099 produce positively correlated profiles. Flyby T099 takes place at a really high inclination, a southern latitude, and at 180° longitude (where the tidal bulge can be found) and, as such, it separates well in magnitude the zonal and tesseral coefficients, but they are very correlated. Additionally, T022 shows high correlation between all the coefficient signal footprints, as this flyby takes place near the sub-Saturn point and with a medium inclination, so the acceleration from the spherical harmonic terms should experience similar evolution during the close approach.

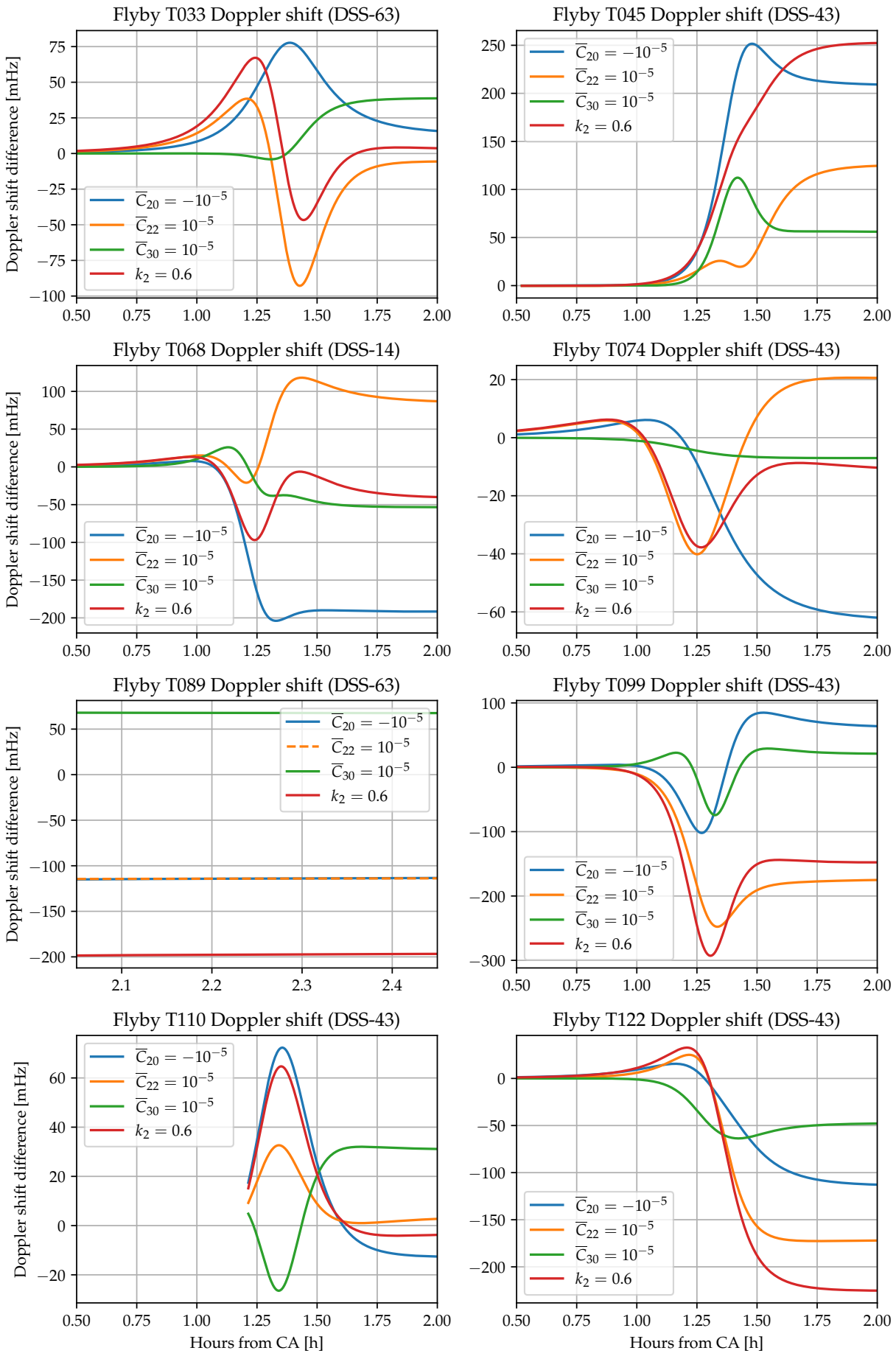

Figure 13: Difference in two-way Doppler data for different simulated gravity field coefficients and flybys.

Once again, it might have been noticed that both T089 and T110 have incomplete coverage of the close approach, especially the first one. As explained before, this is because for this batch of simulated data only two-way Doppler observables are being considered and the relative position of the DSN stations and the Saturnian System at those times is unfavourable and presents black-outs. Of course, with three-way measurements that would no longer be a problem, and the real data presents better temporal coverage (also simulated three-way Doppler is later used in Chapter 4).

To close up, the main takeaways from this whole section will be pointed out. Simulated Doppler data, analogous to the real data and taking into account relativistic effects, has been produced for the different Titan flybys and several virtual gravity fields. It has been studied and visualised how the flyby geometry not only relative to Titan but also with respect to the ground stations on Earth and in relation to the other flybys so a good overall Titan coverage is attained, is fundamental to reduce correlations between coefficients and being able to successfully discriminate the signal from each of the gravity field parameters. The magnitude of the special and general relativistic effects has been explored and determined to be relevant even when attempting to just estimate the dipole field of the Saturnian moon. As such, they must always be carefully considered when modelling the Doppler measurements. It has also been observed that for two-way data, the Sun is the only body that has to be taken into account in the calculations for the general relativity corrections. Lastly, it has been tested how the variation in Doppler signal arising from different coefficients behaves as linearly additive: it corresponds well with the change in relative velocity despite the relativistic corrections being applied. Thus, no minima should exist in proximity to each other and convergence to the solution is expected to be fast. These sets of simulated data were generated for the purpose of verifying the GEODYN configuration. The outcomes from that process will be described in the next section.

3.2 Verification tests

The capability of generating simulated data provides enormous freedom to conduct a careful review of the model setup. As it was already suspected in Chapter 2, the model in GEODYN displays some unexplained behaviours, namely a strong correlation between parameters and a large model mismatch, larger than the dipole field's signal, that can only be compensated with large empirical accelerations and measurement biases. For that reason, the setup was tested with the simulated data previously described and, again, an unacceptably important signal was found in the residuals. Having complete knowledge of how the artificial data was produced (i.e. the virtual fields, all the radiometric effects and dynamical modelling), the goal was set to reproduce in estimation the parameters from the simulations and, in the process, explain the source of the inconsistencies between the two models implemented in GEODYN and with Tudat (and hopefully shed some light into why the real data presents large residuals). These considerations are addressed in this chapter, although, in the end, unfortunately not all the causes for the differences observed have been found.

3.2.1 Empirical accelerations and measurement biases

The first step into the verification process was to directly test the GEODYN model with the simulated Titan point mass gravity field and all the relativistic effects acting on the radio tracking signal. This is to emulate the estimation with real data with no changes to the GEODYN configuration. Because of their great impact on the residuals, only the empirical accelerations were toggled on and off, in order to check the resulting estimated gravity field parameters and signal

in the residuals.

Case	EA, MB	EA	MB	No EA, no MB
μ (km^3/s^2)	8980.5846 ± 0.0173	8980.5764 ± 0.0173	8978.1588 ± 0.0148	8978.2173 ± 0.0148
k_2	10.425 ± 0.662	2.164 ± 0.660	27.614 ± 0.508	22.184 ± 0.507
$J_2 \times 10^6$	-126.872 ± 13.364	9.631 ± 13.314	-557.163 ± 10.279	-491.207 ± 10.255
$C_{21} \times 10^6$	93.398 ± 0.758	21.334 ± 0.738	33.642 ± 0.591	-26.521 ± 0.579
$S_{21} \times 10^6$	8.702 ± 1.620	236.610 ± 1.518	51.694 ± 1.136	307.538 ± 1.037
$C_{22} \times 10^6$	-160.990 ± 6.631	-77.524 ± 6.616	-277.192 ± 5.075	-220.406 ± 5.068
$S_{22} \times 10^6$	36.180 ± 0.704	49.590 ± 0.702	-57.111 ± 0.569	-41.294 ± 0.567
$J_3 \times 10^6$	-76.070 ± 2.890	-442.217 ± 2.815	-23.328 ± 2.443	-445.998 ± 2.363
RMS residuals	201.8 mHz	324.0 mHz	231.1 mHz	348.6 mHz

Table 7: Estimated values for the spherical harmonics coefficients and their 1-σ errors when using simulated two-way Doppler data with a Titan point-mass gravity. Four cases were tested with and without empirical accelerations (EA) and measurement biases (MB).

The estimated coefficients with the two-way Doppler data converted to relative velocity (Eq. 1.33) are presented in Tab. 7. As it can be seen, in all test cases the estimated spherical harmonics coefficients are far from being null, meaning that, as with the real data, there is a strong model mismatch. However, the difference here is that when performing an estimation with the empirical accelerations and measurements now the residuals are quite large compared to those of the estimations in Section 2.1 (201.8 mHz vs. 5.1 mHz). Looking at the plot of the residuals in Fig. 14, two problems can be observed at play. The first one is that the estimation filter seems to be having some trouble matching the signals from the two different antennae. That is the reason why flyby T110 was chosen for the figures, to showcase this phenomenon. The second problem, and possibly a cause for the first one in the simulations with measurement biases that can compensate offsets between antennae, is the presence of strange, regular jumps in the residuals.

These mysterious shifts manifest in the residual signal as if they were noise, although no noise was simulated for the virtual data. Instead of showing the characteristic dispersion of a somewhat Gaussian stochastic noise, the points appear distributed in extremely regular steps. The oscillations in residuals, not present previously with the real data (see Fig. 2), reveal that there must be an issue either with how the simulated data is fed to GEODYN or how it is processed (these jumps were not seen in the Doppler plots like Fig. 13 in the previous section). This could be due to integration error and/or not properly lining the time steps. However, the integration error was checked when generating the data and it cannot justify the large residuals (the numerical accuracy in velocity is within 10^{-9} m/s. The light-time equations were solved to an accuracy of 10^{-6} s, and the time step between data points is set as ten seconds in GEODYN, exactly as with the simulated data. It is also not a problem with the initial point for integration in GEODYN: it uses a multi-step predictor-corrector that does not need to fall exactly on the measurement points as, by default, it then interpolates in time to match the observations. Also, in any case, a test run was made forcing the initial state to be equal to the one for the simulated data and the same dispersion was found in the residuals, as it will be described in Section 3.2.8. The reasons behind the weird jumps are further discussed in that subsection. Nevertheless, as can be observed in Figs. 14 and 15, this disruptive signal is not dominant in the cases where no measurement biases are considered, so for now it can be ignored as an important objective of these verification tests is to explain the large gap between models.

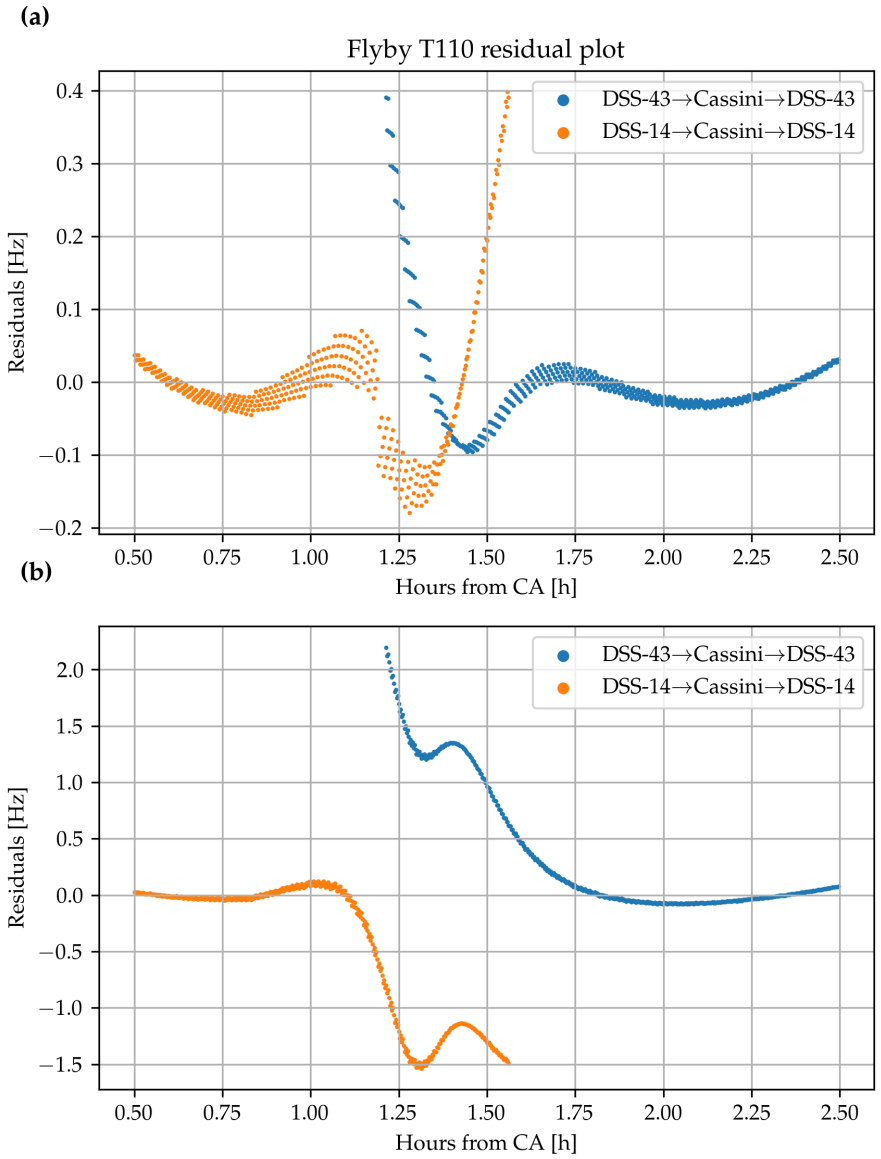

Figure 14: Doppler residuals for flyby T110 for the cases with empirical accelerations and **(a)** with measurement biases and **(b)** without them. The RMS of the residuals in this flyby for each case are 85.39 mHz vs. 724.5 mHz respectively.

Focusing again in Tab. 7, it can be seen how in all tests the estimated coefficients are large, as well as the RMS of the residuals. As expected, the empirical accelerations reduce the residuals. It is noticeable how both cases without measurement biases present significantly greater residuals, as well as spherical harmonics coefficients, being the largest when not estimating both the accelerations and biases. Observing the residual plots (Figs. 14 and 15), it is clear how the cases without biases fail to match the residuals from one of the ground stations with those of the other. The two signals present a similar shape in both situations but the estimation filter fails to make them overlap, leaving instead a big offset between them. At first glance, this would suggest a disagreement between the relative velocities of the DSN antennae in each of the models but, as discussed in Section 3.2.7 this seems unlikely and, on top of that, the relative velocity between

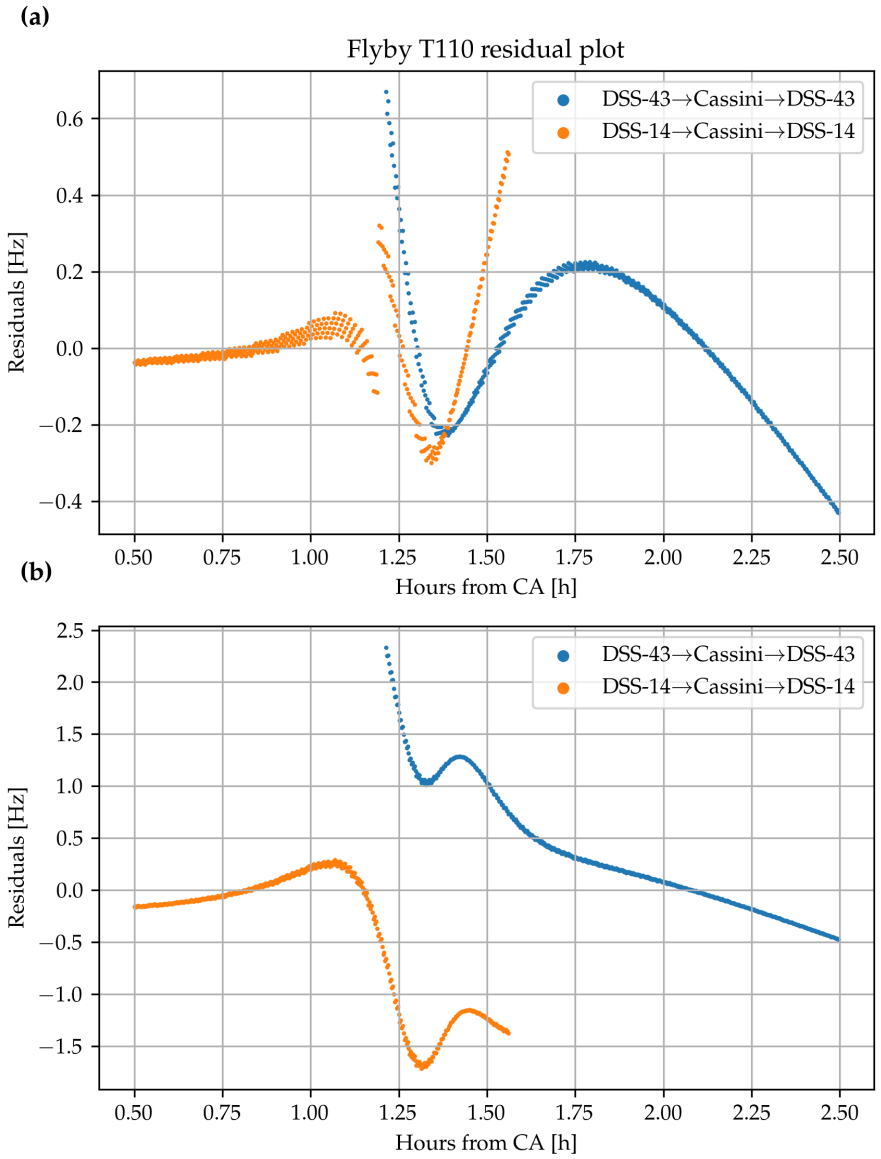

Figure 15: Doppler residuals for flyby T110 for the cases without empirical accelerations and **(a)** with measurement biases and **(b)** without them. The RMS of the residuals in this flyby for each case are 179.8 mHz vs. 746.5 mHz respectively.

the ground stations must be close to zero in any case as they are Earth-fixed (they are moving at significantly different relative velocities with respect to Cassini but, because of that relationship, if the residuals of one of them are good, then those of the other have to be small as well). In the test with no empirical accelerations but with biases the two sets of residuals are closer to match as their shape is not perturbed by the accelerations and the offset is compensated by the biases. In conclusion, there are three features in the residual signal that need explanation: the structured and perturbing jumps between points, the displacement of the curves from different antennae and the overall magnitude of the residuals when omitting the empirical accelerations and measurement biases.

3.2.2 Simulated fields and Titan reference frame

The disagreement that has been found between the simulated data and the GEODYN model is not catastrophic in the sense that the estimator does not diverge and the gravitational parameter of Titan is estimated reasonably well. Nevertheless, it is a strong mismatch when facing a precise orbit determination problem, and it does not allow for the estimation of the spherical harmonic terms. Given that the spherical harmonics gravity field produced by Titan is, by definition, bound to its body-fixed reference frame, any modelling error regarding Titan's orientation (defined by its rotation axis and prime meridian) would lead to an enormous footprint in the residuals, potentially of similar magnitude as the signal previously observed. Thus, this mismatch possibility needed to be assessed.

Case	**Null field**	$\overline{C}_{20} = -10^{-5}$	$\overline{C}_{22} = 10^{-5}$	$\overline{C}_{30} = 10^{-5}$	$k_2 = 0.6$
	Values				**Differences in coefficients**
μ **(km^3/s^2)**	8980.5846 ± 0.0173	$+0.0000$	-0.0002	$+0.0000$	-0.0001
k_2	10.425 ± 0.662	$+0.008$	$+0.016$	-0.016	$+0.602$
$\overline{C}_{20} \times 10^5$	5.674 ± 0.598	-0.991	$+0.011$	-0.011	$+0.002$
$\overline{C}_{21} \times 10^5$	7.235 ± 0.059	$+0.003$	$+0.005$	$+0.030$	-0.000
$\overline{S}_{21} \times 10^5$	0.674 ± 0.125	$+0.012$	$+0.001$	-0.023	$+0.000$
$\overline{C}_{22} \times 10^5$	-24.941 ± 1.027	-0.012	$+0.977$	$+0.016$	-0.002
$\overline{S}_{22} \times 10^5$	5.605 ± 0.109	-0.002	-0.036	-0.010	-0.000
$\overline{C}_{30} \times 10^5$	2.875 ± 0.109	$+0.009$	$+0.006$	$+0.993$	-0.000
RMS residuals	201.8 mHz	201.8 mHz	201.8 mHz	201.8 mHz	201.8 mHz

Table 8: Estimated values for the spherical harmonics coefficients of the simulated gravity field of Titan and their 1-σ errors when including empirical accelerations and measurement biases. The estimated coefficients for the non-null fields are expressed as the difference with respect to the null field.

The verification results that were presented so far in the previous subsection were only using the simulated null field. However, a remarkable behaviour is obtained when also feeding to the estimation filter the other simulated data sets with the different virtual gravity fields described in Section 3.1.3. Tabs. 8-11 show the estimated normalised coefficients for the null field, by how much the coefficients differ with respect to the empty harmonics when using the non-zero fields and the RMS of the residuals in all test cases, for all the combinations of estimation setups with and without the empirical acceleration and biases. The reason why the coefficients that come from the tests with the fields that are not empty are expressed as differences in those tables is not fortuitous. The change in the coefficients in all cases, independently from the estimation setup, is extremely close to the field that was simulated. This is a very important result, as it proves that GEODYN is being able to detect the changes in gravity field and there is certainly some agreement between the models. What is messing with the estimation is the existence of what can be regarded a great bias in the coefficients, which manifests as the solution to the null field, caused by a large, unexplained signal. Also, the fact that the difference in coefficients is so precise, despite all the problems with the residuals observed in the previous subsection (the artificial dispersion, the offset between antennae and overall large signal) and in spite of the considerable variation in residual profiles depending on whether additional parameters like the empirical accelerations and measurement biases are estimated or not (Figs. 14 and 15), shows how strongly linearly is the problem behaving. This is confirming once again what was already seen in Section 3.1.3 and explains the results in

Section 2.3 where the inequality constraints failed to find another minimum.

Case	Null field	$\overline{C}_{20} = -10^{-5}$	$\overline{C}_{22} = 10^{-5}$	$\overline{C}_{30} = 10^{-5}$	$k_2 = 0.6$
	Values				Differences in coefficients
μ (km^3/s^2)	8980.5764 ± 0.0173	$+0.0000$	-0.0002	$+0.0000$	-0.0002
k_2	2.164 ± 0.660	$+0.008$	$+0.018$	-0.011	$+0.605$
$\overline{C}_{20} \times 10^5$	-0.431 ± 0.595	-0.991	$+0.013$	-0.007	$+0.005$
$\overline{C}_{21} \times 10^5$	1.653 ± 0.057	$+0.003$	$+0.005$	$+0.030$	-0.001
$\overline{S}_{21} \times 10^5$	18.328 ± 0.118	$+0.013$	$+0.002$	-0.022	$+0.000$
$\overline{C}_{22} \times 10^5$	-12.010 ± 1.025	-0.011	$+0.974$	$+0.010$	-0.007
$\overline{S}_{22} \times 10^5$	7.682 ± 0.109	-0.002	-0.036	-0.011	-0.001
$\overline{C}_{30} \times 10^5$	16.714 ± 0.106	$+0.009$	$+0.007$	$+0.992$	-0.000
RMS residuals	324.0 mHz	324.0 mHz	324.0 mHz	324.0 mHz	324.0 mHz

Table 9: Estimated values for the spherical harmonics coefficients of the simulated gravity field of Titan and their 1-σ errors when including empirical accelerations. The estimated coefficients for the non-null fields are expressed as the difference with respect to the null field.

Case	Null field	$\overline{C}_{20} = -10^{-5}$	$\overline{C}_{22} = 10^{-5}$	$\overline{C}_{30} = 10^{-5}$	$k_2 = 0.6$
	Values				Differences in coefficients
μ (km^3/s^2)	8978.1588 ± 0.0148	$+0.0000$	-0.0000	$+0.0002$	$+0.0000$
k_2	27.614 ± 0.508	$+0.005$	$+0.011$	$+0.009$	$+0.598$
$\overline{C}_{20} \times 10^5$	24.917 ± 0.460	-0.992	$+0.008$	$+0.013$	-0.002
$\overline{C}_{21} \times 10^5$	2.606 ± 0.046	$+0.002$	$+0.006$	$+0.024$	$+0.000$
$\overline{S}_{21} \times 10^5$	4.004 ± 0.088	$+0.012$	$+0.003$	-0.013	$+0.000$
$\overline{C}_{22} \times 10^5$	-42.942 ± 0.786	-0.007	$+0.983$	-0.021	$+0.003$
$\overline{S}_{22} \times 10^5$	-8.848 ± 0.088	-0.002	-0.034	-0.011	$+0.000$
$\overline{C}_{30} \times 10^5$	0.882 ± 0.092	$+0.010$	$+0.008$	$+0.990$	$+0.001$
RMS residuals	231.1 mHz	231.1 mHz	231.1 mHz	231.1 mHz	231.1 mHz

Table 10: Estimated values for the spherical harmonics coefficients of the simulated gravity field of Titan and their 1-σ errors when including measurement biases. The estimated coefficients for the non-null fields are expressed as the difference with respect to the null field.

This last result rules out the possibility of a serious mismatch in the reference frames for Titan in the two models as then the shifts in coefficients when swapping the input data would manifest as arbitrary ones. This is because the simulated field would improperly map into the one defined in the estimation software, so that the signal from some of the coefficients would leak into the other spherical harmonics terms, and that is certainly not the case here. As can be seen in Tabs. 8-11, the differences are detected well not only for the static dipole field, but also for the periodic variations represented by k_2. The shift in higher degree J_3 is also recorded nicely.

Case	Null field	$\overline{C}_{20} = -10^{-5}$	$\overline{C}_{22} = 10^{-5}$	$\overline{C}_{30} = 10^{-5}$	$k_2 = 0.6$
	Values				Differences in coefficients
μ (km^3/s^2)	8978.2173 ± 0.0148	$+0.0001$	$+0.0000$	$+0.0003$	$+0.0000$
k_2	22.184 ± 0.507	$+0.006$	$+0.012$	$+0.012$	$+0.601$
$\overline{C}_{20} \times 10^5$	21.967 ± 0.459	-0.991	$+0.009$	$+0.015$	$+0.001$
$\overline{C}_{21} \times 10^5$	-2.054 ± 0.045	$+0.002$	$+0.006$	$+0.024$	$+0.001$
$\overline{S}_{21} \times 10^5$	23.822 ± 0.080	$+0.013$	$+0.004$	-0.012	$+0.001$
$\overline{C}_{22} \times 10^5$	-34.145 ± 0.785	-0.008	$+0.982$	-0.025	-0.002
$\overline{S}_{22} \times 10^5$	-6.397 ± 0.088	-0.001	-0.034	-0.011	$+0.000$
$\overline{C}_{30} \times 10^5$	16.857 ± 0.089	$+0.011$	$+0.009$	$+0.989$	$+0.001$
RMS residuals	348.6 mHz	348.6 mHz	348.6 mHz	348.6 mHz	348.6 mHz

Table 11: Estimated values for the spherical harmonics coefficients of the simulated gravity field of Titan and their 1-σ errors when not including empirical accelerations or measurement biases. The estimated coefficients for the non-null fields are expressed as the difference with respect to the null field.

Observing that the change in the periodic Saturn tide k_2 term is detected without any trouble of leakage into the J_2 and C_{22} equilibrium tide coefficients suggests that the phenomenon of high correlation between those parameters found on Chapter 2 with the real Doppler data is not due to how the spherical harmonics of Titan are defined, nor an intrinsic correlation resulting from a poor flyby geometry and coverage (see Chapter 4). If attention is paid to the residuals, it can be seen that they stay constant in each of the tables despite the relatively large variation in coefficients resulting from the different virtual fields. They do not vary across sets of simulated data even in the case when there are no empirical accelerations or Doppler frequency biases, implying that the new estimated gravity parameters are successfully absorbing the signal that necessarily emerges from the shift in coefficients, which is in the order of $\sim 10^2$ mHz (as depicted in Fig. 13). This behaviour where the residuals are insensible to significant differences in solutions might seem similar to what could be observed in Chapter 2 when discussing correlation between parameters, but it is fundamentally different here as the input data is being modified when comparing tests and the additional signal is being properly fitted, thus it disappears from the residuals. The increase in k_2 is not producing any appreciable change in J_2 and C_{22} and vice-versa, contrary to what happened when imposing different constraints on k_2 with the real data.

In conclusion, the important leftover signal in the residuals that is common to all simulations has to originate from another element of the problem other than a disagreement in the definition of the spherical harmonics gravity of Titan and its reference frame. The GEODYN setup and the simulated data are at least partially compatible as the changes in gravity field are captured well in the GEODYN solution. However, the large bias in coefficients and strange residuals are still unexplained.

3.2.3 Correlation between parameters

Before continuing with the search for other possible mismatches between the models in order to explain the behaviour previously described, it can be of interest to check the results from the previous tests in terms of their correlation matrices, in order to check whether the high correla-

tion found in Chapter 2 still persists. Fig. 16 presents the correlation matrix of the gravity field parameters when using both the empirical accelerations and observation biases (right) and without them (left). In this case the matrices belong to the tests with the null field as input data, but they do not present any significant change with virtual fields. Those two cases were picked to be displayed because they represent the cases with the least and most residuals, respectively. It can be noticed that both matrices show similar correlations and that in both cases the parameters are highly correlated, especially J_2, C_{22} and k_2, just like what happened with the real data (Figs. 3 and 5 in Chapter 2). It is interesting though how some correlations change sign between matrices. For instance, when turning off the accelerations and biases, the correlation between J_2 and C_{22} becomes positive but the correlation between J_2 and k_2 is negative. No explanation for this has been found and this last correlation matrix bears more resemblance to the ones with the real data.

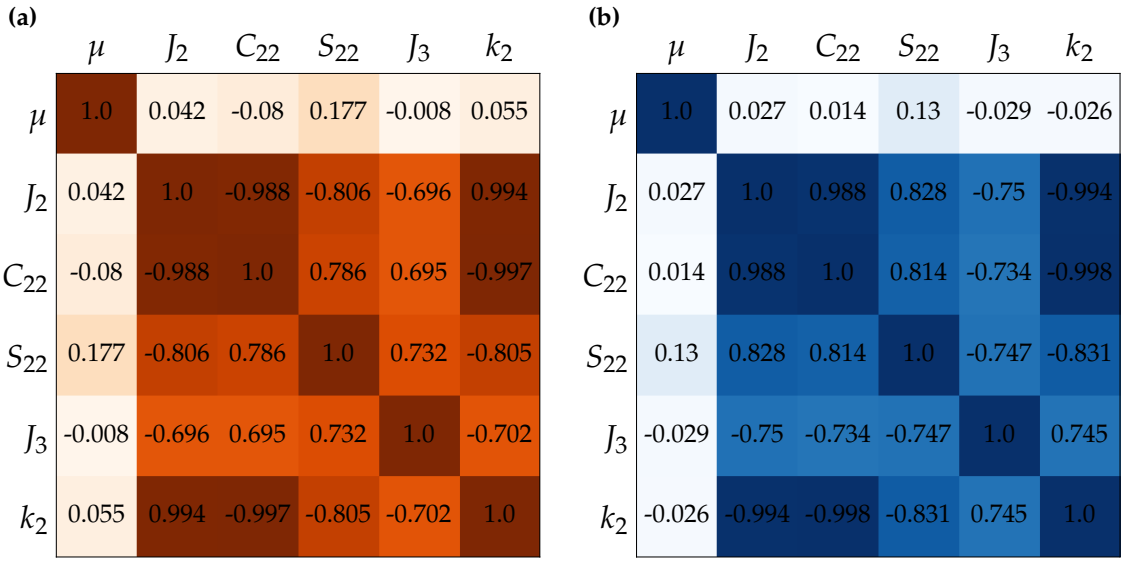

Figure 16: Correlation matrix for relevant gravity field parameters when estimating with the simulated null field and **(a)** with empirical accelerations and simple measurement biases and **(b)** without them. Differences between the two are small, but some correlations change sign.

At first glance, these results seem to contradict what was discussed in the previous subsection, where changes in the dipole coefficients were detected and would not be coupled with the other parameters, as suggested by these correlation matrices. But they instead reinforce the idea, also hypothesised in Chapter 2 with the real data, that these correlations are forced by the large bias coming from some mismodelling and not by poor data quality. That is to say, that the base values obtained for the coefficients (i.e. the ones from the null field tests) are tightly conditioned by the unexplained signal, but their variation when modifying the input field is uncorrelated. To provide an additional proof for this, the tests presented in Tab. 12 were conducted. In order to eliminate the possibility of correlation between coefficients all gravity parameters (excluding μ) were constrained to be zero except the coefficient being studied, and two runs were executed: one with the point-mass gravity field as input and another with the point-mass gravity field and the coefficient in question being not null. All results are from using the GEODYN setup with empirical accelerations and measurement biases off (so the behaviour with the complete mismatched signal can be studied).

As it can be observed in Tab. 12, something interesting happens when constraining all coefficients but one in all cases: the strange null field bias does not disappear, but it becomes significantly smaller than in previous tests (see Tab. 11). Also the formal errors get reduced. The fact that

Case	Null field	Coefficient	Difference	RMS residuals
k_2	0.554 ± 0.014	1.154 ± 0.014	$+0.600$	352.9 mHz
$\overline{C}_{20} \times 10^5$	2.436 ± 0.030	1.442 ± 0.030	-0.994	351.5 mHz
$\overline{C}_{22} \times 10^5$	3.878 ± 0.032	4.871 ± 0.032	$+0.994$	354.6 mHz
$\overline{C}_{30} \times 10^5$	0.237 ± 0.023	1.232 ± 0.023	$+0.995$	352.3 mHz

Table 12: Estimated values of the simulated gravity field of Titan when not including empirical accelerations or measurement biases and only estimating the coefficient indicated (as well as μ). The *coefficient* column denotes the results using the field with the corresponding coefficient having the values used in previous tests ($\overline{C}_{20} = -10^{-5}$, $\overline{C}_{22} = 10^{-5}$, $\overline{C}_{30} = 10^{-5}$ and $k_2 = 0.6$).

the bias in coefficients is persistent even in these heavily constrained setups confirms that it is not just due to some obscure correlation between parameters and it can only be solved by reviewing the dynamical and measurement models in search of the root cause or causes. Nevertheless, the reduction in magnitude of estimated coefficients reveals how the estimation filter, when facing the large unmodelled signal, tries to compensate for it with all the coefficients collectively and, as they fail to properly do so, they drive each other into large values. Thus, it is the failure to fit the Doppler observations that is producing the poor correlation matrices.

It can be seen once again that, when comparing the cases with and without the null field, the changes in the spherical harmonics gravity field are correctly detected, this time with striking precision. As in the results in Section 3.2.2, the residuals are the same when swapping between the null field and the respective field with a non-zero coefficient, meaning that the shift in gravity field is compensated adequately. The RMS of the residuals is only slightly bigger in the constrained cases than in the unconstrained one. That they are larger is a result that is not surprising, as the estimation filter has less freedom to fit the Doppler signal. However, it is worth noticing that the variation in residuals is really small despite constraining the problem so much, a manifestation of what have just been discussed about the origin of the strange results.

3.2.4 Atmospheric effects

Up until this point, the possibilities of an incorrect definition of reference frame of Titan or high correlation between gravity coefficients have been discarded as being the cause for the big residuals. Now is time to recall that, in order to keep the simulated data model simple just for the verification runs, no atmospheric effects were simulated. Here the term atmospheric effects loosely refers to two phenomena very different in nature and area of application within the gravity determination problem. The first one would be the drag force on the Cassini spacecraft exerted by Titan's far reaching atmosphere at the lower altitudes of the flybys. This force was already expected to be not relevant for the dipole field (and also the drag coefficient should be estimated as zero if dismissed in the simulated data), but an extra test with it turned off in the GEODYN setup was performed to check if there could be a mistake on how it is configured, as drag is an along-track force and any error in its modelling or estimation can have a radical impact. The previous contribution concerns the dynamical model of the orbit but, in addition to it, the Earth's atmosphere certainly has an impact on the measurements. This effect manifests as a path delay in the radio uplink and downlink and in GEODYN it is accounted by calculating both ionospheric and tropospheric corrections. As already anticipated by studying the relativistic effects (see Section 3.1.2), any physical phenomena that affects the Doppler observables has the potential to severely disrupt the estimation results, especially those that affect the light-time equation and, thus, the

timing of the measurements.

Case	No atm. corr.	No atm. corr. and no drag	No EA, no MB difference
μ ($\mathbf{km^3/s^2}$)	8978.2107 ± 0.0148	8978.2107 ± 0.0148	-0.0066
k_2	21.791 ± 0.507	21.791 ± 0.507	-0.393
$\overline{C}_{20} \times \mathbf{10^5}$	21.749 ± 0.459	21.749 ± 0.459	-0.218
$\overline{C}_{21} \times \mathbf{10^5}$	-2.224 ± 0.045	-2.224 ± 0.045	-0.169
$\overline{S}_{21} \times \mathbf{10^5}$	24.624 ± 0.080	24.624 ± 0.080	$+0.803$
$\overline{C}_{22} \times \mathbf{10^5}$	-33.543 ± 0.785	-33.543 ± 0.785	$+0.602$
$\overline{S}_{22} \times \mathbf{10^5}$	-6.255 ± 0.088	-6.255 ± 0.088	$+0.142$
$\overline{C}_{30} \times \mathbf{10^5}$	17.361 ± 0.089	17.361 ± 0.089	$+0.503$
RMS residuals	349.7 mHz	349.7 mHz	+1.1 mHz

Table 13: Estimated values for the spherical harmonics coefficients of the simulated point-mass gravity field of Titan without ionospheric and tropospheric corrections due to the Earth's atmosphere and also without drag from Titan's atmosphere. No empirical accelerations or measurement biases were estimated.

For those reasons, the drag acceleration and the ionospheric and tropospheric corrections were selectively disabled in GEODYN to find if they were the main source for the disagreement with the simulated data. Some of the results from these runs, without using empirical accelerations or measurement biases, can be regarded in Tab. 13. There, the estimated coefficients without the atmospheric corrections on the measurements and also without any drag force or estimation of the drag coefficient are displayed, as well as their difference relative to the corresponding previous test case that did not omit those contributions. As it can be seen, the drag force has no perceptible effect on the estimation results, both cases shown in the table present the same coefficient and RMS of residuals. Looking at how they compare to the previous setup, it is proven that the ionospheric and tropospheric corrections certainly have an important effect on the solution that cannot be ignored when performing an estimation. However, they are far from cancelling the mysterious bias in the coefficients and, as such, they are not the cause for the bulk mismodelling that manifests in the residuals.

The RMS of the residuals barely gets modified, slightly increasing, but, as in previous tests, this change is too subtle and does not correspond with the magnitude of the variation in coefficients. This means that the underlying signal is still persisting and the change in Doppler because of not calculating the corrections is absorbed by the estimated gravity field. It must be noted though, that in the cases with observation biases, that can compensate the offset between stations, the RMS of the residuals reduces roughly 10 mHz (RMS of 193.3 mHz with accelerations and biases and 223.6 mHz with only biases). To sum up, the path delay caused by atmospheric refraction has a relevant effect in the estimation but it does not account for the large signal that the estimation filter fails to fit. In all the tests that will follow, they were turned off to ensure more consistency with the simulated data.

3.2.5 Propagation of the position of Titan

In the previous subsection, the impact of a possible mismatch between the GEODYN configuration and the measurement simulation model was studied. Additionally, there is a potential for disagreement in the positioning of Titan across the two models, which needed to be checked.

For generating the simulated data, the position of Titan was directly retrieved from the SPICE ephemeris, while in the GEODYN software it was propagated.

Case	Titan from ephemeris	Difference Titan propagated
μ ($\mathbf{km^3/s^2}$)	8978.2173 ± 0.0148	$+0.0066$
k_2	22.184 ± 0.507	$+0.392$
$\overline{C}_{20} \times \mathbf{10^5}$	21.967 ± 0.459	$+0.218$
$\overline{C}_{21} \times \mathbf{10^5}$	-2.054 ± 0.045	$+0.169$
$\overline{S}_{21} \times \mathbf{10^5}$	23.822 ± 0.080	-0.803
$\overline{C}_{22} \times \mathbf{10^5}$	-34.145 ± 0.785	-0.602
$\overline{S}_{22} \times \mathbf{10^5}$	-6.397 ± 0.088	-0.142
$\overline{C}_{30} \times \mathbf{10^5}$	16.857 ± 0.089	-0.503
RMS residuals	348.6 mHz	-1.1 mHz

Table 14: Estimated values for the spherical harmonics coefficients of the simulated point-mass gravity field of Titan when extracting the state of Titan from the SPICE ephemeris. The difference with respect to the case where the position of Titan is propagated is also displayed. No empirical accelerations, measurement biases and atmospheric corrections where used.

The results when changing the GEODYN executable for an alternate one where the position of Titan in extracted from the SPICE ephemeris can be seen in Tab. 14. The difference in estimated parameters with respect to the previous setup that updates the state of the moon by propagating it is shown on the column on the right. In these tests, no empirical accelerations, observation biases and atmospheric corrections where considered. As it can be noticed, something similar as in the previous subsection with the atmospheric refraction happens: the impact in the solution is relevant but it still fails to reduce the residuals and is small in comparison to the leftover signal. Again, the residuals stay practically constant (they reduce a bit). For those reasons, the way the state of Titan is simulated is not the main cause for the mismatch between models and extracting it from the SPICE ephemeris does not solve the issue with the large bias in the estimated coefficients. These considerations and differences can however be significant for future estimations.

3.2.6 Relativistic effects

In Section 3.1 it was shown how the relativistic effects have a considerable effect on the Doppler measurements, of $\sim 10^2$ mHz in two-way and three-way observables. The unexplained residual signal that has been tried to be addressed in the previous subsections is of the same order of magnitude. As such, it was hypothesised that the root of the problem with the estimation could be in the relativistic corrections. By default, GEODYN accounts for the general relativistic effect due to the Sun and also the spacecraft's clock frequency drift due to both special and general relativity (McCarthy et al., 2015). However, the approximations used in GEODYN and in the simulated data are not the same. That is why some tests needed to be performed, disabling relativistic computations in both the artificial measurements and GEODYN, to verify whether the estimation significantly improves and strange results for the null field are no longer obtained.

It was in performing those checks where a bottleneck was found when checking the output files detailing the corrections being applied to the data: despite explicitly turning off all relativistic corrections in the GEODYN setup configuration input files, the estimation software was still

Case	SR	SR full	NR	NR full
μ (km^3/s^2)	8978.2134 ± 0.0148	8978.4766 ± 0.0148	8977.0507 ± 0.0148	8977.3072 ± 0.0148
k_2	21.838 ± 0.507	29.054 ± 0.507	107.466 ± 0.510	114.751 ± 0.510
$\overline{C}_{20} \times 10^5$	21.789 ± 0.459	29.221 ± 0.459	96.373 ± 0.461	103.837 ± 0.461
$\overline{C}_{21} \times 10^5$	-2.222 ± 0.045	-2.816 ± 0.045	-5.403 ± 0.045	-5.981 ± 0.045
$\overline{S}_{21} \times 10^5$	24.634 ± 0.080	29.638 ± 0.080	15.294 ± 0.080	20.266 ± 0.080
$\overline{C}_{22} \times 10^5$	-33.617 ± 0.785	-44.948 ± 0.785	-167.750 ± 0.789	-179.182 ± 0.789
$\overline{S}_{22} \times 10^5$	-6.262 ± 0.088	-7.004 ± 0.088	-11.014 ± 0.088	-11.763 ± 0.088
$\overline{C}_{30} \times 10^5$	17.371 ± 0.089	20.049 ± 0.089	-13.101 ± 0.090	-10.398 ± 0.090
RMS residuals	349.9 mHz	429.0 mHz	476.0 mHz	435.1 mHz

Table 15: Estimated values for the spherical harmonics coefficients of the simulated point-mass gravity field of Titan. The simulated data with only special relativistic effects (SR) and with no relativistic computations (NR) were tested in the GEODYN setup with the corrections turned off in the configuration files. Also simulations were run brute-forcing them to be zero in the software (SR full and NR full).

applying some relativistic corrections. And they were extremely large ones, in the order of one meter per second in terms of relative velocity for some of the data points. The reason for this undesired behaviour is that, before performing the estimation, GEODYN pre-processes the data. How this pre-processing takes place is governed not only by the configuration files but also by some words embedded in the input data. These pre-processing words had to be modified for each data point to fully turn off all undesired corrections, including the relativistic ones. However, even after changing the pre-processing words and turned off relativity in the GEODYN configuration files, a large relativistic correction was being applied regardless. To cancel this last undesired contribution it was necessary to go into the source code and brute-force the relativistic corrections to be zero.

As a side note, the simulated data was transformed into the GEODYN input data format using its associated tracking data formatting program. The usage of this program was not exempt of trouble: a hard to spot integer overflow was corrupting the transformation. In the end it was found to be caused by how data timestamps were being stored as the software was written in the eighties and dates past the year 2010 would overflow. Changing the default integer precision did not solve the issue as it messed up with other parts of the software, but finally modifications were made to achieve a workaround.

The resulting estimated coefficients for the point-mass gravity field can be seen in Tab. 15. It can be observed that no matter if only the GEODYN input files are modified, if all relativity in the software is forced to be disabled or if simulated data with only special relativity or no relativity is taken into account, the bias in the estimated parameters does not go towards zero. In fact, the estimations are even worse in terms of residuals and magnitude of the spherical harmonics, especially in the cases where no relativistic calculations were made over the generated data. The test case with all relativity turned off is the one was expected to reconcile best the GEODYN and simulated data models but instead the estimation filter obtains very poor results and even greater residuals compared to the previous tests with the relativistic effects. However, this case has at least better RMS of residuals than the similar one where the pre-processing words and software were not touched. This last behaviour would suggest, but not prove, that disabling the pre-processor corrections improves the quality of the fit. However, the same does not apply to the estimations using the data with accounted special relativity. This and the large disagreement

between gravitational parameters in Tab. 15 makes seem more likely that it was just an accidental result.

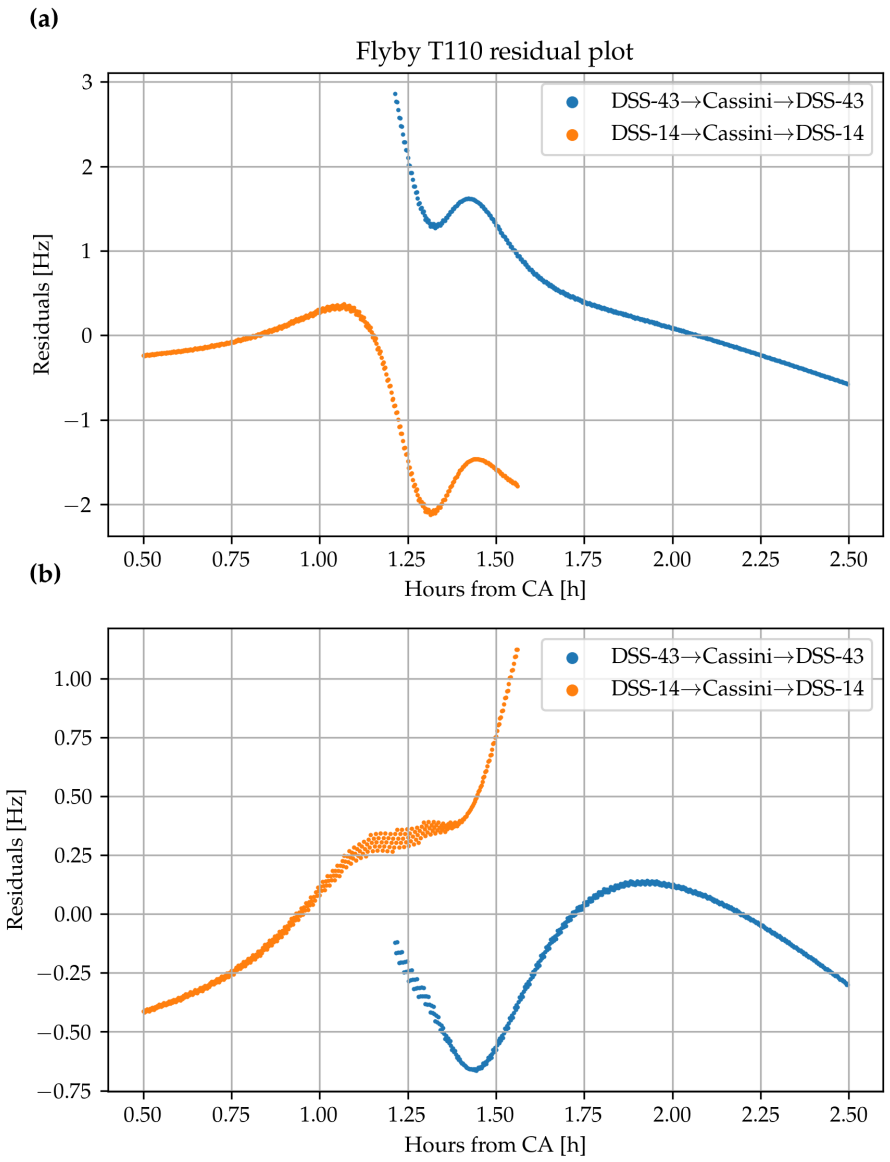

Figure 17: Doppler residuals for flyby T110 for the cases with **(a)** simulated data accounting for special relativity and **(b)** the data without relativistic effects (936.0 mHz vs. 335.1 mHz RMS respectively). All relativistic effects were stripped from the estimation processing chain.

The rationale behind also doing tests utilising the data with only the effects of special relativity was to check if, for some reason, GEODYN is still applying that correction to the Doppler observables. The residuals of flyby T110 for the cases with all relativistic corrections turned off in GEODYN can be viewed in Fig. 17. It is curious that, unlike the RMS of the residuals in Tab. 15, for this particular flyby the case with no relativistic effects in the simulated data presents smaller residuals, and the spurious dispersion in data points can be perceived a bit. The shapes of the curves for the case with special relativity correspond better with each other. The offset between antennae first identified in Section 3.2.1 is still present.

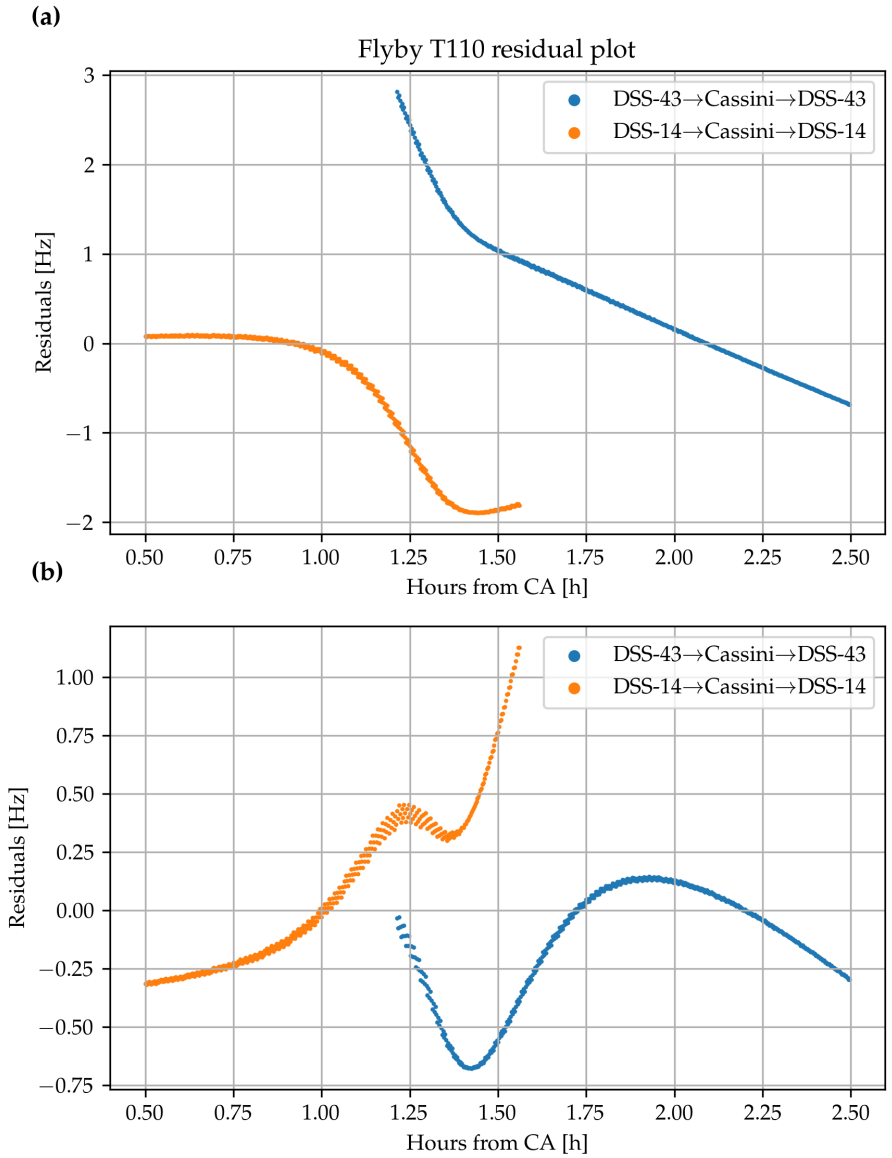

Figure 18: Doppler residuals for flyby T110 for the cases with **(a)** simulated data accounting for special relativity and **(b)** the data without relativistic effects (936.0 mHz vs. 335.1 mHz RMS respectively). Only Titan's gravitational parameter was estimated. All relativistic effects were stripped from the estimation processing chain.

It can be noticed that the special relativity data curves in Fig. 17 become linear when they are away from the time of closest approach, corresponding with asymptotic arms of the hyperbolic

trajectory. This could be a good sign towards getting a better estimation, as it could be due to the relativistic effects properly being accounted for, but an incorrect estimated gravitational parameter producing the non-zero trend. Also, because of the effort to minimise the residuals, the estimated gravity field of Titan leaves a marked signature in the residuals near the closest approach. In order to isolate the linear behaviour from that last phenomenon, some additional test runs were conducted setting the spherical harmonics to be null and only estimating the gravitational parameter. The residual plots for flybys T110 and T068 are displayed in Figs. 18 and 19 respectively.

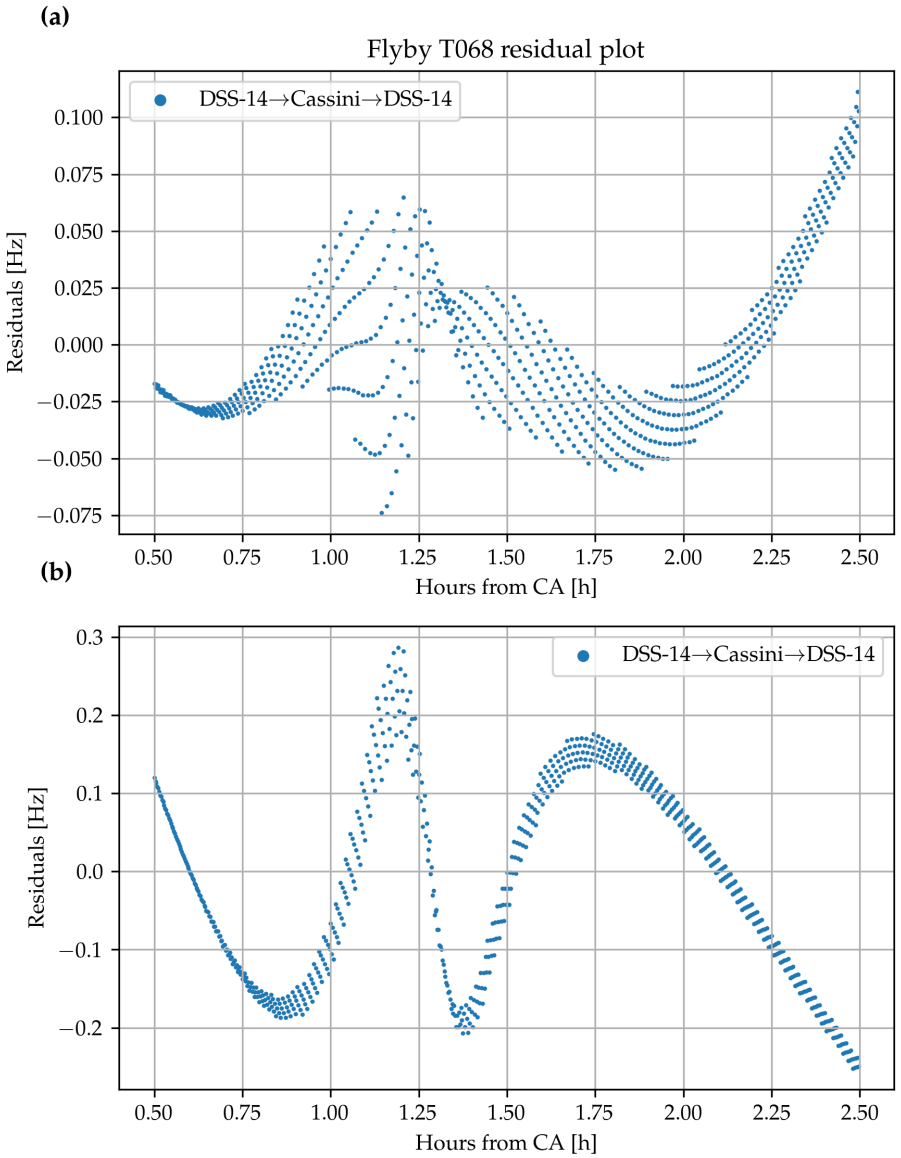

Figure 19: Doppler residuals for flyby T068 for the cases with **(a)** simulated data accounting for special relativity and **(b)** the data without relativistic effects (33.35 mHz vs. 129.0 mHz RMS respectively). Only Titan's gravitational parameter was estimated. All relativistic effects were stripped from the estimation processing chain.

After removing the spherical harmonics of Titan from the estimation, it can be observed in the plots for flyby T110 that the linear profile on the edges becomes more noticeable and clear

in the case with the input data with special relativity. Unfortunately, the estimation still fails to properly estimate the gravitational parameter, and that gets manifested in the negative trend in the DSS-43 antenna curve and the large residuals (and non-linear behaviour) close to Titan. When looking at the residuals form the data with no relativistic effects, the hypothesis that GEODYN is still internally accounting for special relativity becomes more plausible as, despite being smaller in magnitude (note that this is the case in just this particular flyby), the residuals for that case have a wavy behaviour that should not appear in a hyperbolic trajectory (unless there are more modelling mishaps, but then the linearity seen with special relativity would look as an unlikely coincidence).

Shifting focus to another flyby, T068 in Fig. 19, the residuals in a flyby with a single antenna are much more favourable in general. Here the linear curve tails disappear, but the residuals show a heavy influence from the spurious dispersion of points. Also, in this flyby, the case with special relativistic data presents considerably better RMS of residuals (33.35 mHz vs. 129.0 mHz). Very importantly, the special relativistic case is dominated by the artificial and undesired noise from the regular jumps between points. As already discussed, the jumps cannot be attributed to integration numerical errors in the simulated data or matching the integration steps in GEODYN.

What can be concluded is that the mismatch in relativistic corrections was also affecting the solutions and that it is likely that an agreement between the simulated data and the estimation model regarding those contributions is achieved when only calculating the impact of special relativity on the simulated observables and omitting all relativistic considerations in GEODYN (all the ones that were within a reasonable verification effort, that is to say, changing input files, preprocessing words and the slight software modification previously described). There is a persistent strong signal of dispersed points showing a regular jump pattern and ensuring that the relativistic corrections still does not fix the coefficient biases in the estimations.

3.2.7 Ephemeris

As previously suggested, a possible explanation for the bias and the observed residuals could reside in a mismatch between ephemeris that were used. For the planets in the Solar System GEODYN uses values from NASA JPL's development ephemeris DE432 (Folkner, memorandum, 2014, see Folkner et al., 2014). The Cassini SPICE kernel released by the its navigation team uses custom ephemeris for planets, but, given that they are, as the other ones, high-precision for scientific purposes, they are believed to agree.

Having a correct relative state of Titan (Cassini's state is computed relative to it), the Earth and the DSN station on its surface is especially relevant because of the impact on the modelling of the observables, as an error of even 1 mm/s would be unacceptable for measuring the spherical harmonics of Titan.

In the case of the DSN antennae for the simulated data, their states are extracted from the corresponding SPICE kernel, where their positions are expressed in the ITRF93 reference frame (Boucher et al., 1994), an Earth's rotation model for high-precision applications. In GEODYN however, the position of the stations is stored in geodetic coordinates and the rotation of the Earth is internally computed with pole tide and ocean loading models. Nevertheless, there is no strong reason to suspect that there would be a significant difference in the station states from the SPICE kernels and calculated in GEODYN: both are trusted sources, there is a certain tolerance in position and the possible differences in the terrestrial rotation models are estimated to not be significant for the estimation of the dipole field (thus, smaller than the observed residuals). Velocity is what is relevant for Doppler measurements and a relatively large variation in geocentric position only produces a small change in velocity, which is dominated by rotation. Furthermore, there is some

evidence in the residuals from previous verification tests to support that the positioning of the stations is not the cause for the large signal remaining, as discussed in Section 3.2.1.

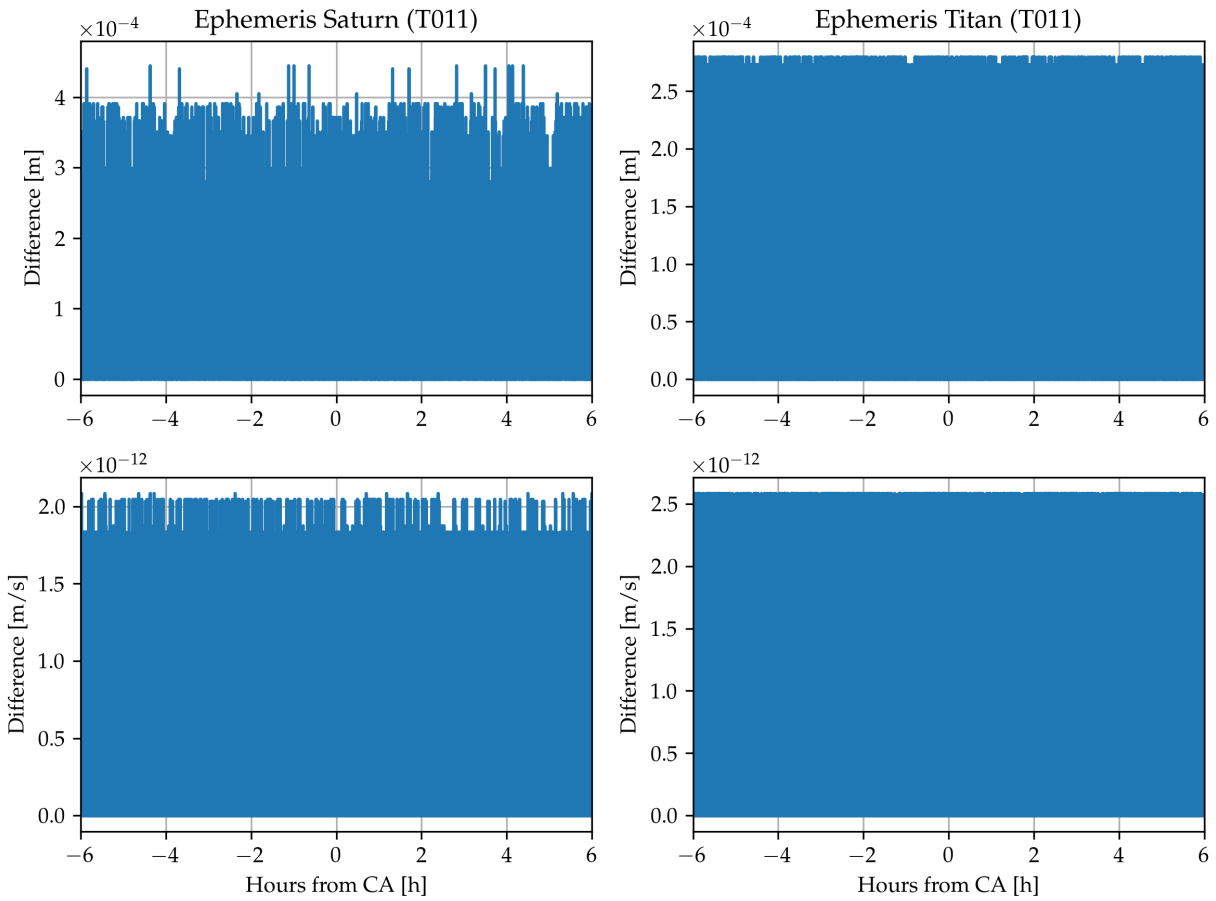

Figure 20: Difference in state (norm of position and velocity difference) between the Titan and Saturn ephemerides used in GEODYN and the ones extracted for the simulated data. The plots just show numerical rounding error.

The last point to discuss concerns the ephemeris for the Saturnian System bodies. Even though the same SPICE kernel was used for obtaining the position of Saturn and its moons, including Titan, in GEODYN and with the simulated data, there are some differences in how the states are computed in the two. Because of the way GEODYN was set up, the state of the bodies is not taken directly from SPICE but tables were generated which are then interpolated with an eighth-order Lagrange interpolator. In order to check if the state was being retrieved as expected, the orbits of the bodies in the two models were compared against each other. The differences for Saturn and Titan are presented in Fig. 20, but also the rest of the moons show similar plots. As can be observed, there is just numerical noise due to rounding errors, and both disagreement in position and velocity are far within acceptable magnitude range (this also verifies that internal numerical errors within SPICE are not an issue).

3.2.8 Integration of the orbit of Cassini

The last important verification test describe in this entire section is checking whether the orbit for the simulated data and the one computed by GEODYN agree. Seen in perspective after all the work done, it should had been the starting point for the whole verification process, although it is true that not nearly the amount of problems that have been encountered with the setup were

expected when starting this entire gravity determination project. It was trusted that the integration of the orbit would be exempt of trouble. This was not the case as it will be explained bellow.

The orbit was tested by running a single GEODYN iteration, so the parameters were not updated, with the same initial values as the ones employed for the generation of the simulated data. To start with the simplest case, the orbit was computed without having any spherical harmonics acceleration from Titan, but the rest of the forces active, excluding atmospheric drag and solar radiation pressure, which were turned off in GEODYN. As such, in principle the only additional acceleration sources accounted by GEODYN but not used dynamical model for the simulated data would be the RTG thermal emissions and gravitational pull by Saturn's rings, both of which are expected to be extremely small (irrelevant for the dipole field). Most importantly, the same initial state of Cassini relative to Titan for the integration of the orbit was ensured to properly compare the trajectories.

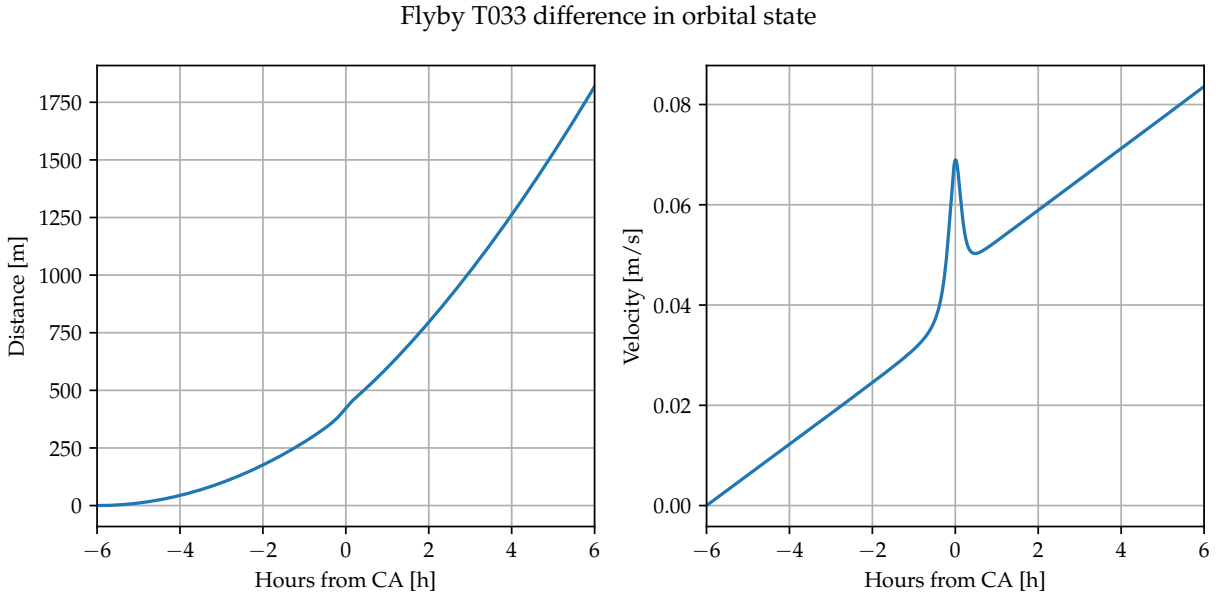

Figure 21: Norm of the difference in position and velocity between the orbit of flyby T033 computed by GEODYN and the one by Tudat for the simulated data.

The norm of the difference in position and velocity between the two orbits can be viewed in Fig. 21. It can be noticed indeed how the orbits present a large disagreement, in terms of velocity (the relevant one for the measurements), of more than 80 mm/s by the end of the twelve-hour arc (remember that the simulated spherical harmonics were in the realm of 1 mm/s). There is a clear overall linear trend present in the velocity, only disrupted by a spike near the closest approach. Note that the influence of Titan can be seen precisely at the time of closest approach (hour zero), unlike in all the previous residual plots were a delay of more than hour was present because of the modelling of the downlink light-trip. The profile of the difference in position is parabolic as a consequence of the linear growth in the velocity curve. The velocity plot implies that there is a constant (except close to Titan) mismodelled acceleration that is affecting the orbit. The spike near Titan can be attributed to the spacecraft arriving at Titan at a different position and velocity which consequently amplifies, due to the large gradient in the gravity field near the moon, the mismatch in the gravitational acceleration from Titan.

Observing this considerable difference in orbit, the next step is to compare and analyse the accelerations that are affecting the trajectories in both software. In Fig. 22, not only the norm of the mismatch in acceleration is plotted but also the three components of the normalised vector in order to get information about what could be causing the difference. Looking at the acceleration magnitude, it can be observed that, as just discussed, it remains constant during the asymptotic

arms of the hyperbolic trajectory and it only spikes close to Titan because of the difference in state when arriving at the moon. This underlying acceleration has a magnitude of $\sim 10^{-6}$ m/s^2. If attention is paid to the unitary vector plots it can be noticed that also the components directed towards Saturn were also present. What this representation proves is that the difference in acceleration is actually pointing towards Saturn, except during the closest approach for the reasons already described. This error (most probably) in the gravity of Saturn came as a surprise, as exactly the same gravitational parameter and spherical harmonic coefficients for Saturn are used in both models.

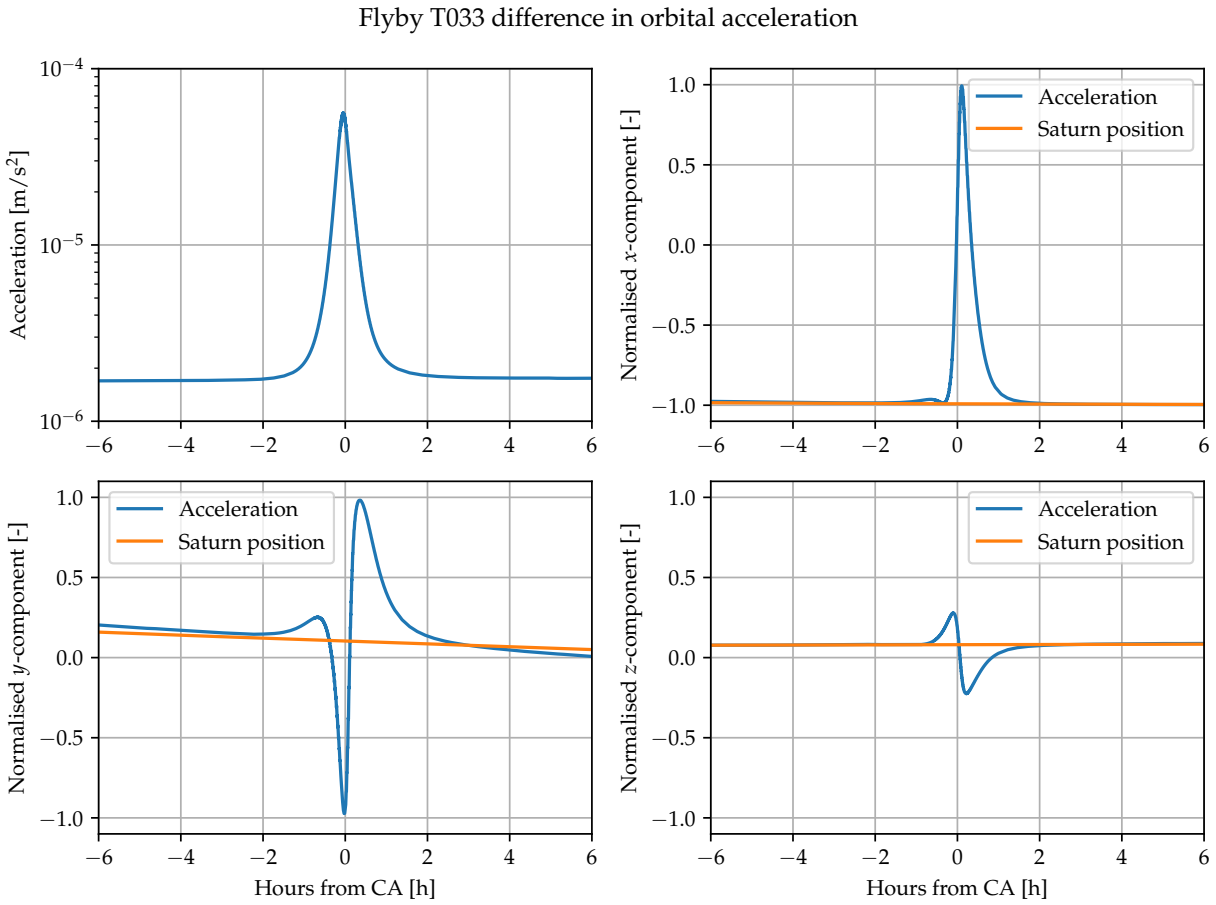

Figure 22: Norm and normalised components in the J2000 reference frame (Feissel & Mignard, 1998) of the difference in acceleration between the orbit of flyby T033 computed by GEODYN and the one by Tudat for the simulated data.

Because of the low inclination of the orbit of Titan, the acceleration mismatch that points in the direction of Saturn could be due to the point-mass gravity field of the planet or any of its even zonal spherical harmonics. For that reason, the orbit was once again computed, but this time disabling the spherical harmonics gravity of Saturn (but leaving its point-mass gravity) in both GEODYN and Tudat. The difference in state between these two new orbits is presented in Fig. 23. Now the orbits match reasonably well, being the mismatch in position and velocity by the end of flyby of just over 2.5 m and 0.1 mm/s. Such a difference in velocity is still non-negligible for gravity determination, but it at least would allow for the detection of the dipole field. The profile of the two curves in this case seems more arbitrary, although there is still a spike in velocity close to Titan, probably in part for the same reasons as previously in Fig. 21, but by looking at the plots for the acceleration (Fig. 24) it can be noticed that here there is more to it.

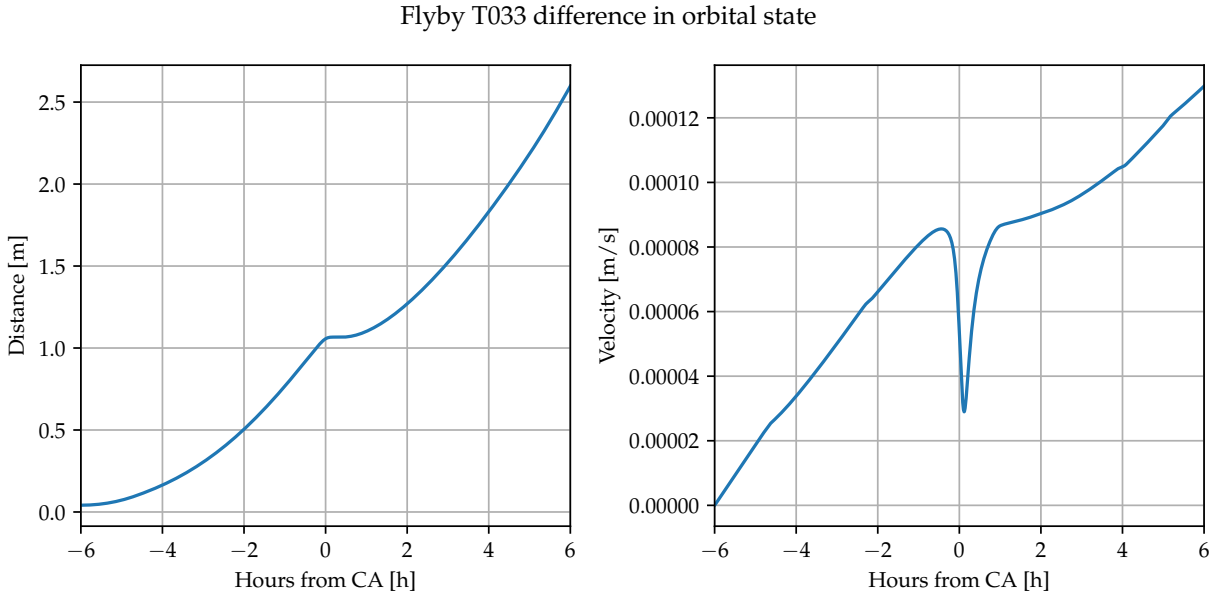

Figure 23: Norm of the difference in position and velocity between the orbit of flyby T033 computed by GEODYN and the one by Tudat for the simulated data. The spherical harmonics of Saturn were omitted in both propagations of the orbit.

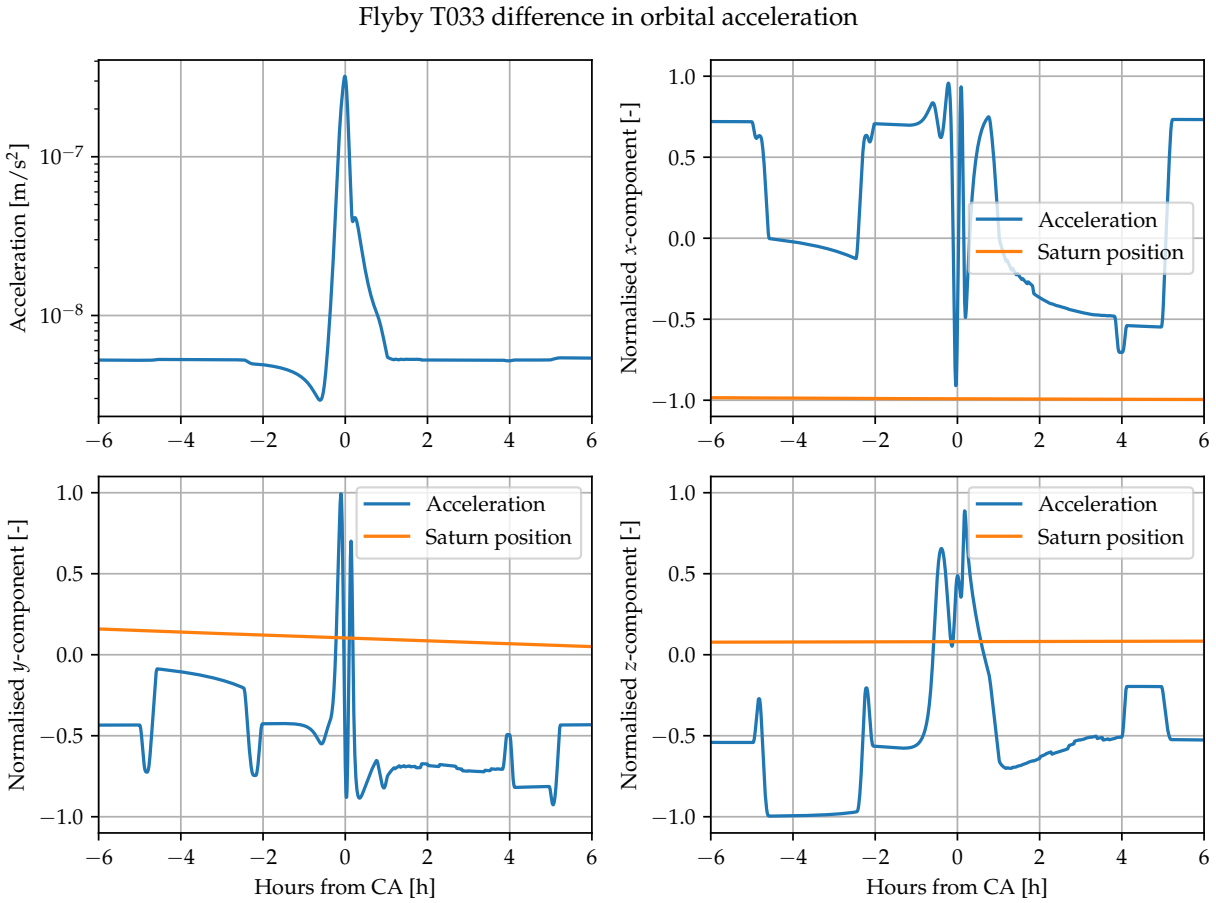

Figure 24: Norm and normalised components in the J2000 reference frame of the difference in acceleration between the orbit of flyby T033 computed by GEODYN and the one by Tudat for the simulated data. The spherical harmonics of Saturn were omitted in both propagations of the orbit.

Looking at the acceleration difference in Fig. 24 it can be seen how it is two orders of magnitude smaller. It also no longer points towards Saturn, or even any particular direction consistently during the entire flyby. As previously mentioned, these results cannot be attributed to integration numerical truncation error when generating the orbit with Tudat, as the error was checked to be in the realm of 10^{-9} m/s, five orders of magnitude bellow the observed discrepancy. This confirms that the strange linear acceleration seen previously is because of some issue regarding the implementation of the spherical harmonics of Saturn. There is further evidence to think that this strange acceleration comes from an error in the imlementation based on GEODYN: it can be recalled that in Section 2.4 the residuals from real data shown in Fig. 4 when removing empirical accelerations presented an unmistakably dominant linear trend, much like the one observed here in the orbital velocity (Fig. 21), and independent from however the simulated data has been generated (appears when using real data). The implementation of the spherical harmonics gravity of Saturn was a custom addition for the Titan gravity determination problem and, given how complex the GEODYN software is, it is not unreasonable to think that maybe the new acceleration source leads to some bug.

Once removed the mismatch due the spherical harmonics of Saturn, away from Titan an underlying acceleration difference which is constant in magnitude persists. Being $\sim 10^{-9}$ m/s^2, it is near what can be expected for the RTG emissions (see Tab. 1). However there are reasons to suspect that it is not caused by the RTG acceleration or then that acceleration source is improperly implemented in GEODYN. This is because the anisotropic thermal emission from the RTGs must be constant (over the timespan of a single flyby) in Cassini's body-fixed reference frame. As the spacecraft was constantly pointing towards the Earth with the high-gain antenna during the flybys in order to obtain high-quality Doppler measurements (except in flyby T110 where the omnidirectional low-gain antenna was used), the large jumps that appear in Fig. 24 in the direction of the acceleration could not possibly correspond to a constant vector in Cassini's frame.

However, a feature in Fig. 24 that stands out is how erratic is the behaviour of the acceleration near the point of closest approach to Titan. There is a strong and narrow spike of two orders of magnitude and the direction of that acceleration swings violently, so it cannot be attributed to the point-mass gravity of Titan (or at least only to it). The empirical accelerations cannot be the cause for this as they are turned off and also because they would work in eight-hour intervals anyway. It also cannot be associated to thruster firings because there are no sudden, impulsive footprints in the velocity plot and impulsive shots would not leave a direct footprint in acceleration (but of course the would indirectly affect it by modifying the orbit). As previously mentioned, Titan spherical harmonics, the atmospheric drag and solar radiation pressure were switch off for this propagation. The normalisation employed for the spherical harmonics was also checked. Taking into account all of this, the source for this discrepancy in the dynamical model remains unknown after this whole study.

Despite the remaining unexplained acceleration, the difference in orbits without the harmonics of Saturn would allow to try and test if the gravity of Titan can be estimated much better and the strong bias in the coefficients (Section 3.2.1) is finally gone. As such an estimation run was carried out in which the initial state was constrained to always be the same one as in the simulated data (thus, it is not updated by the estimation filter) and the simulated observables that were used as an input for GEODYN were generated with the new orbit without Saturn's spherical harmonics. The resulting difference in orbit after the estimation of the coefficients can be seen in Fig. 25 and it is much worse than even in the initial integration with the problematic harmonics (Fig. 21). The bias in the estimated Titan harmonics coefficients, instead of being null, it becomes much larger than in all previous verification tests: for both the observables with only special relativity or no relativistic effects at all the estimation loop yields $\sim 10^{-2}$ values for some of the normalised coefficients and $\sim 10^3$ for k_2. If the initial point is not constrained then similar values as previously are obtained for the coefficients when estimating the null field.

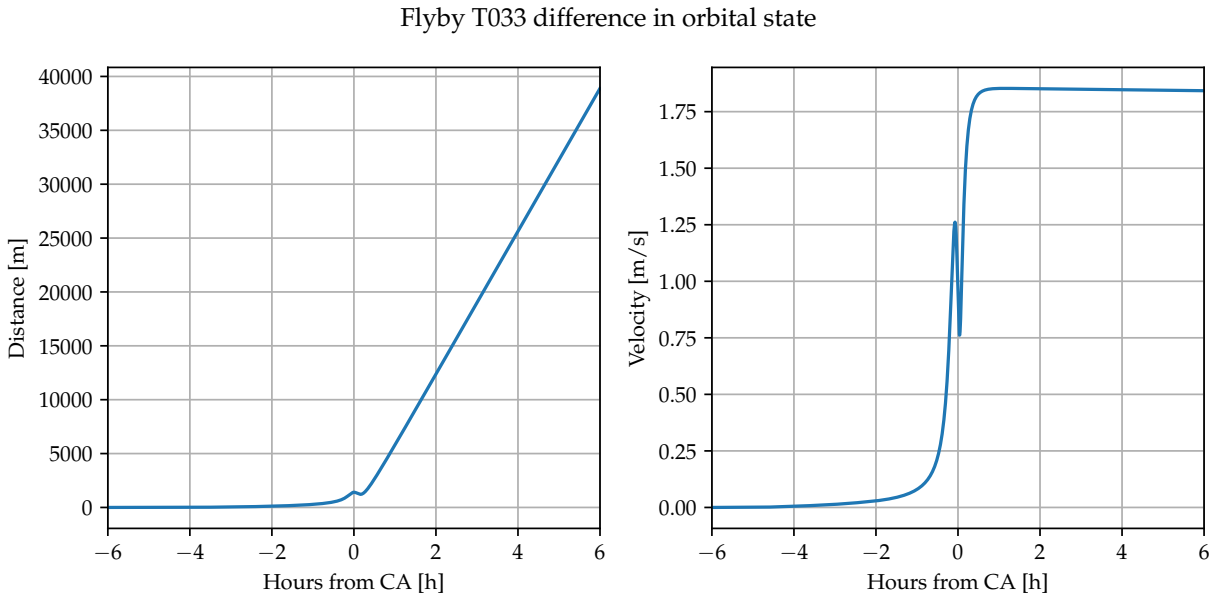

Figure 25: Norm of the difference in position and velocity between the orbit of flyby T033 computed by GEODYN and the one by Tudat for the simulated data. The spherical harmonics of Saturn were omitted in both propagations of the orbit and the spherical harmonics of Titan were estimated by GEODYN.

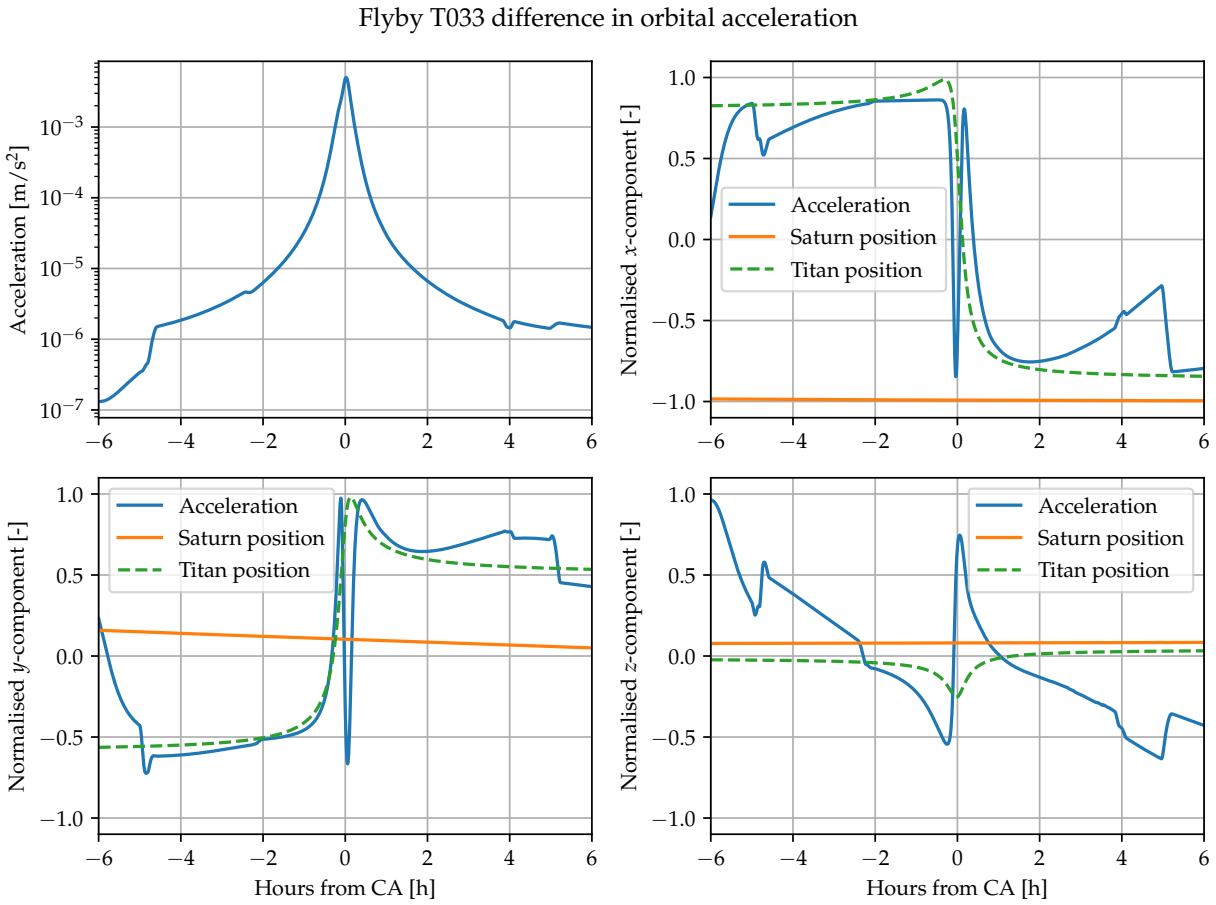

Figure 26: Norm and normalised components in the J2000 reference frame of the difference in acceleration between the orbit of flyby T033 computed by GEODYN and the one by Tudat for the simulated data. The spherical harmonics of Saturn were omitted in both propagations of the orbit and the spherical harmonics of Titan were estimated by GEODYN.

Looking at the plots comparing the acceleration (Fig. 26), it can be observed how the difference grows over 10^{-3} m/s^2 and the central peak is much wider. There is a strange jump in acceleration approximately five hours prior to the closest approach. The plots of the normalised vector components are mysteriously jagged, resembling the same unexplained behaviour just seen in Fig. 24. This time also the components of the unitary vector pointing towards Titan have been displayed. There is some correlation with the acceleration direction, most probably because of the effect of the incorrectly estimated gravitational parameter. It can be noticed how Saturn is not the source of the acceleration discrepancy. Again, there are weird swings in the acceleration direction near Titan, although this time they can be attributed as well to the incorrectly estimated large spherical harmonics gravity coefficients of Titan. These unfavourable results and unphysical acceleration profiles when trying to perform an estimation, in spite of doing a good effort of reconciling the two dynamical models, are also indicators that there is as well some issue with the estimation setup in GEODYN.

To conclude this chapter, there is evidence to think that the estimation was being disturbed by an error in the implementation in GEODYN of the gravitational acceleration due to the spherical harmonics of Titan, which would help to explain the results with real data presented in Fig. 4 of Section 2.4. Additionally, there are some hints in the strange, unexpected and inexplicable results that would suggest that there are also some issues in the estimation segment of the GEODYN setup. Overall, the residuals in the verification tests that have been described in this chapter presented an spurious dispersion (even though no noise was included in the simulated data) where they performed somewhat regular jumps. It has been argued that it is unlikely that this is due to integration or interpolation errors. The fact that the estimation fails in the last test performed were, in principle, the propagated orbits were reconciled to allow for the estimation of at least the low-degree harmonic terms also supports the idea that how GEODYN is performing the estimation needs a more profound review. Although many of them have a considerable effect on the solution, it has been proven that parameters and elements of the model like the empirical accelerations, measurement biases, reference frame of Titan, atmospheric effects, relativistic effects and ephemeris in general are not the cause for the large leftover signal in the residuals observed in all of the tests and the strong bias in the estimated gravity coefficients. Furthermore, the influence of the solar radiation pressure (just $+0.003$ in $\overline{C}_{20}$) and the rings of Saturn was checked and determined to be minimal. A remarkable behaviour that has been recorded is that GEODYN, despite the underlying disagreement with the simulated data, is capable of detecting changes in the simulated gravity field coefficients with great accuracy, a manifestation of the linear behaviour of the problem (as it became clear many times throughout this study) and proof that both the simulated data and GEODYN are not completely incompatible.

Unfortunately, the amount of time for a project like this is limited. GEODYN is a complex and sophisticated program written in Fortran, regarded by the author as a fantastic language for scientific applications regardless of its antiquity, but which has disadvantages with respect to more modern languages in terms of required implementation and debugging effort. Thus, getting deep into reviewing and testing its inner workings is no easy feat. With this panorama of a multitude of unintended behaviours whose cause is yet to be explained, it was decided to stop trying to verify the estimation setup in GEODYN and, with all the knowledge gained so far in the many tests that were performed, conform with drawing more general conclusions about the Titan gravity determination problem and its prospects.

4 Simulated estimation with Tudat

The tests presented in the previous chapter, although inconclusive as to what was the ultimate source for the signal in the residuals, provided some insight about the nature of the problem and required setting up the necessary software for simulating Doppler observables. Having developed aside such tool for simulation, it is possible to consider the possibility of going one step further and also performing estimation and studying what results can be obtained. The greatest challenge when moving forward to estimating parameters is the great implementation effort that setting up all the pertinent partial derivatives can demand. As it can be recalled, the simulated data was generated by combining the functionalities of the Tudat libraries for orbit propagation with custom functions developed by the author for calculating the Doppler shift experienced by Cassini's tracking radio signal subjected to relativistic effects. Fortunately, the partial derivatives related to the dynamical modelling were already implemented in Tudat. As such, only the partials regarding the measurement modelling had to be incorporated. Additionally, although there are plans for incorporating that capability in the future in Tudatpy (the Python interface for Tudat), at the time this project was carried on the least-squares estimation routines were not fully available. For that reason, a multi-arc global inversion algorithm was also written for the current work and incorporated in order to have a full iterative estimation loop.

In this chapter the results from putting this estimation filter to the test with simulated data analogous to the real measurements (simulated flybys replicate the real ones as described in Section 3.1) are presented. Also some lines are devoted to describe the partials derived for the Doppler measurements. First an estimation with noiseless simulated observables was performed to check whether the setup was properly working. Then simulated estimations were done with different noise powers. In line with the investigations in from the previous chapter, the effect of two model mismatches was studied: unaccounted relativistic effects and a possible timing bias. Finally, a few comments are made about the prospects of using this new setup for performing an estimation with real data.

4.1 Doppler measurement partials

As explained, the partial derivatives for the two-way Doppler measurements needed to be derived and incorporated into the estimation procedure. Tudat provides the partials to construct both the state transition and sensitivity matrices, which linearly approximate changes in initial state and force model parameters into variations in the propagated state (see Eq. 1.20). Following the first order differentiation approach, the partial derivatives of the function that relates the state of Cassini with the resulting two-way Doppler observables have to be computed, such that (following the notation used in Sections 1.1 and 1.2)

$$\mathbf{y}(t) = f_R(t, \mathbf{x}_{TR}(\mathbf{X}_0, \mathbf{p})) \Rightarrow \Delta\mathbf{y}(t) = \frac{df_R}{d\mathbf{x}_{TR}}(t)(\Phi(t)\Delta\mathbf{X}_0 + S(t)\Delta\mathbf{p}) \tag{4.1}$$

where $\mathbf{y}$ are the observations, f_R is the received frequency, $\mathbf{x}_{TR}$ is the state of Cassini, $\mathbf{X}_0$ is the initial state vector, $\mathbf{p}$ is the force parameter vector, Φ is the state transition matrix and S is the

sensitivity matrix. Thus, $df_R/d\mathbf{x}_{TR}$ would correspond to $\tilde{H}$ in Eq. 1.19.

Then, the gradient of f_R for two-way Doppler measurements is obtained by taking the derivative of Eq. 1.32:

$$\frac{df_R}{d\mathbf{x}_{TR}} = Mf_T\left(\nu_{TR,T}\frac{d\nu_{R,TR}}{d\mathbf{x}_{TR}} + \nu_{R,TR}\frac{d\nu_{TR,T}}{d\mathbf{x}_{TR}}\right) \tag{4.2}$$

The fully (first order approximation) relativistic expressions for the uplink and downlink fractional shifted frequencies, $\nu_{TR,T}$ and $\nu_{R,TR}$ respectively, provided in Section 1.2 are a bit convoluted and would take some effort to both derive and implement into the estimation software. Fortunately, the partials can be obtained to good approximation from the expressions with just the classical Doppler effect. The classical partial derivatives represent most of the gradient (accounting for relativity would only slightly correct that vector), and it is good enough of an approximation for reaching convergence, as proven by the results from the tests in this chapter. This valid approximation probably also saves computational effort as the simpler formulas require less operations to calculate.

The frequency ratio resulting from the classical Doppler shift experienced on the uplink of the radio signal corresponds to

$$\nu_{TR,T} = \frac{f_{TR}}{f_T} = \frac{1-\mathbf{k}\cdot\mathbf{v}_{TR}}{1-\mathbf{k}\cdot\mathbf{v}_T} \tag{4.3}$$

The uplink partials with respect to Cassini's position and velocity respectively are then

$$\frac{d\nu_{TR,T}}{d\mathbf{r}_{TR}} = \mathbf{0} \quad \frac{d\nu_{TR,T}}{d\mathbf{v}_{TR}} = -\frac{\mathbf{k}}{1-\mathbf{k}\cdot\mathbf{v}_T} \tag{4.4}$$

An important assumption that has been made here as well is that the light propagation vector $\mathbf{k}$ (Eq. 1.26) does not depend on Cassini's position $\mathbf{r}_{TR}$. This is, of course, not true, but it can be safely considered constant in this particular problem where the position of Cassini is defined relative to Titan and the a priori information about the initial state is really good, and the overall change position with respect to Titan during an entire flyby is negligible in the interplanetary scale of the relative position vector between the spacecraft and the Earth. Similarly, if the Doppler shift experienced during the downlink can be formulated in classical terms as

$$\nu_{R,TR} = \frac{f_R}{f_{TR}} = \frac{1-\mathbf{k}\cdot\mathbf{v}_R}{1-\mathbf{k}\cdot\mathbf{v}_{TR}} \tag{4.5}$$

then the corresponding partial derivatives are

$$\frac{d\nu_{R,TR}}{d\mathbf{r}_{TR}} = \mathbf{0} \quad \frac{d\nu_{R,TR}}{d\mathbf{v}_{TR}} = \frac{1-\mathbf{k}\cdot\mathbf{v}_T}{(1-\mathbf{k}\cdot\mathbf{v}_{TR})^2}\mathbf{k} \tag{4.6}$$

Finally, combining Eqs. 4.2-4.6, the final expression for the partials for the two-way Doppler measurements used for the estimation filter studied in this chapter is achieved

$$\frac{df_R}{d\mathbf{r}_{TR}} = \mathbf{0} \tag{4.7}$$

$$\frac{df_R}{d\mathbf{v}_{TR}} = \frac{1-\mathbf{k}_{TR,T}\cdot\mathbf{v}_{TR}}{1-\mathbf{k}_{TR,T}\cdot\mathbf{v}_T}\frac{1-\mathbf{k}_{R,TR}\cdot\mathbf{v}_T}{(1-\mathbf{k}_{R,TR}\cdot\mathbf{v}_{TR})^2}\mathbf{k}_{R,TR} - \frac{1-\mathbf{k}_{R,TR}\cdot\mathbf{v}_R}{1-\mathbf{k}_{R,TR}\cdot\mathbf{v}_{TR}}\frac{\mathbf{k}_{TR,T}}{1-\mathbf{k}_{TR,T}\cdot\mathbf{v}_T} \tag{4.8}$$

In the last expression, $\mathbf{k}_{TR,T}$ and $\mathbf{k}_{R,TR}$ represent respectively the uplink and downlink light propagation direction vectors. It must be noted that, although the distinction between the two was omitted in the previous equations, they are different vectors as the positions of Titan and the Earth vary during the more than two hours long radio signal round-trip. Nevertheless, the difference is very slight but, because the vectors need to be computed anyway for the light time equations, distinguishing them avoids any unnecessary potential trouble that might arise from simplifying even more.

4.2 Noiseless estimation

In this section an overview of the estimation setup in given and the results of a verification run without any simulated noise are presented showing that the estimation loop works properly. For the dynamical modelling of the spacecraft's orbit, only gravitational interaction were taken into account: the gravity field of Titan (which is estimated), the spherical harmonics gravity of Saturn from Iess et al. (2019) as in the GEODYN setup, the other seven largest moons of Saturn, the Sun and Jovian System. No acceleration due to atmospheric drag, RTG thermal emissions or solar radiation pressure was incorporated into the model. As mentioned in Section 3.1, they are not relevant for the dipole field and in any case, it is not necessary to model them in order to test whether the problem is well-conditioned by nature given its flyby geometry and quality of the data, as the simulated data and the estimation filter models are consistent and both do not use them.

Regarding the measurement modelling, the fully relativistic two-way Doppler observables were taken into account, as defined in Eq. 1.32. As it was seen in Section 3.1, the Sun is the only relevant astronomical body (for a low degree and order estimation) for the general relativistic corrections and, as such, is the only one considered in the relativity calculations. For the two-way Doppler partials, the classical expressions just described in the previous section were used instead. An option was configured to add a simple timing bias in the receiver signal reception timestamp, in order to study the consequences of timing issues (it would also be equivalent to an unaccounted path delay in the downlink). It was set to zero in all the estimation runs for the last tests in this chapter.

For the simulated data that was generated to fed up to the estimation filter, the same three stations considered for the simulated data in the previous chapter (DSS-14, DSS-43 and DSS-63), one from each DSN complex at Goldstone, Madrid and Canberra, were considered. As explained in Section 3.1.1, for the purposes of this simulacrum of the real problem, it does not matter which antenna is chosen (the current work does not get so deep into noise modelling) as long as they represent realistic visibility conditions from the surface of the Earth. This time, however, there is a difference in the sets of data points that are generated with respect to the measurements previously considered in Chapter 3. Both two-way and three-way observations are produced in the time interval spanning from three hours and a half prior to the closest approach to six hours afterwards. The observables are generated in a sort of simulated best-case-worst-case scenario were a single uplink and downlink link are available from the transmitting and receiving stations with the best visibility conditions. As such, only simulated data from one combination of transmitter to spacecraft to receiver is generated at any given time (despite the fact that other combinations could also be feasible at that time). This can be visualised in the residual plot in Fig. 29 and, by looking at residuals with real data like in Fig. 2, it can be observed how the choice made here is a realistic approximation of the availability of real data. Once again, a minimum elevation angle of 15° over the horizon was defined for a feasible observation and, although very few and short, there are some gaps present in the simulated data due to lack of visibility (only in flybys T089 and T110).

As for the estimated parameters, the setup was configured to estimate the initial states for all the flybys, the gravitational parameter μ and spherical harmonics of Titan up to a certain degree and order depending on the test, as well as the second degree Love number k_2. In all tests only the dipole field (maximum degree and order of two) is estimated, with the exception of the test in Section 4.3 emulating the estimation conducted in Durante et al. (2019), where the field is estimated up to degree and order five.

The initial guess for the gravitational parameter has been purposively selected as a relatively

Case	Noiseless estimation	Error true parameters
μ (km^3/s^2)	8978.1388	$-2 \cdot 10^{-5}$
k_2	0.600	$+4 \cdot 10^{-6}$
$J_2 \times 10^6$	30.000	$-1 \cdot 10^{-4}$
$C_{21} \times 10^6$	0.000	$+1 \cdot 10^{-4}$
$S_{21} \times 10^6$	0.000	$-6 \cdot 10^{-5}$
$C_{22} \times 10^6$	9.000	$-9 \cdot 10^{-6}$
$S_{22} \times 10^6$	0.000	$+2 \cdot 10^{-5}$
RMS residuals	0.303 mHz	

Table 16: Estimated values for the spherical harmonics coefficients obtained from a verification test run of the new estimation setup without simulating noise in the measurements. The column on the right represents the error with respect to the parameters used for generating the observables.

poor guess (given the available literature for a real estimation scenario) of $\mu = 8980\ km^3/s^2$ so the stability of the solution given by the estimation filter can be put to the test. As the initial guess for the coefficients of the spherical harmonics of Titan, they all were considered to be null. The guesses for initial states of all the flybys have a true deviation of +1 km and +1 m/s (the latter by far the most impactful) in the NTW reference frame (velocity-normal, velocity-tangent, cross-track frame of reference, Vallado, 2001). The reason for using such reference frame is that it is tangent to the velocity (unlike the RSW used for the empirical accelerations in GEODYN), and it is more representative of the true scope of the deviations in state when dealing with an object in a hyperbolic orbit far away from the central body, where the greatest influence in the orbit could be expected to be given by the error in the direction tangent to the velocity (which is close to the radial direction far from the main body).

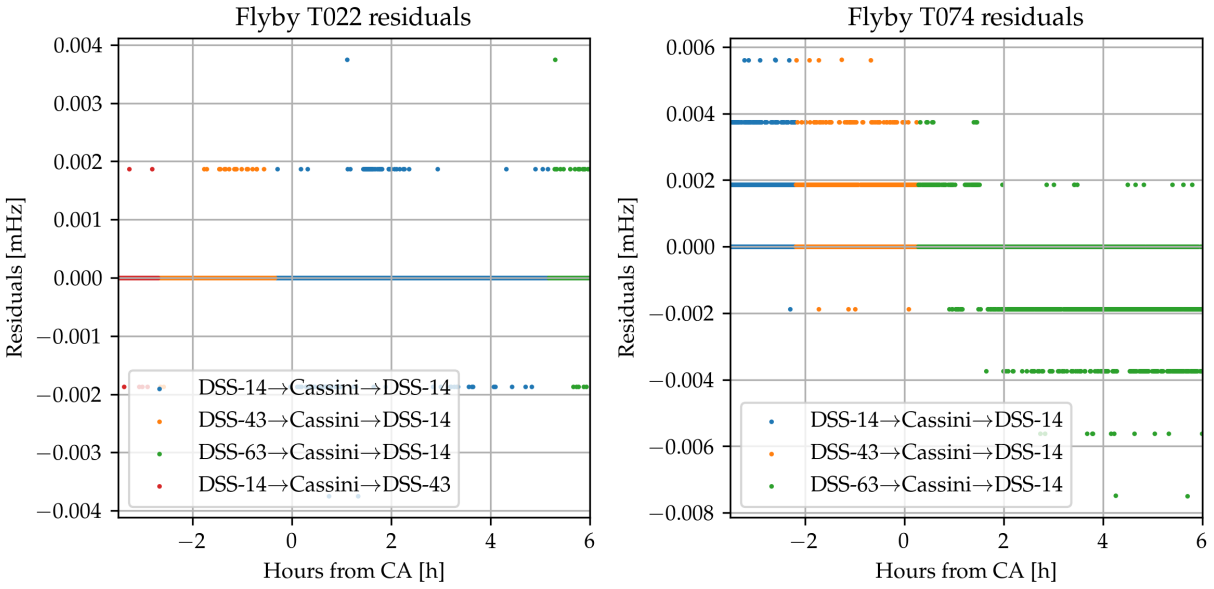

Figure 27: Residual plots of flybys T022 and T074 from the noiseless test run. The different colours represent the combinations of transmitter and receiver antennae. In this case the residuals are dominated by numerical rounding error.

This whole setup was first verified by running tests without any noise in the simulated data.

	μ	J_2	C_{21}	S_{21}	C_{22}	S_{22}	k_2
μ	1.0	0.082	0.146	0.013	0.091	0.018	0.098
J_2	0.082	1.0	-0.201	-0.305	0.947	-0.689	0.97
C_{21}	0.146	-0.201	1.0	0.132	-0.089	0.187	-0.129
S_{21}	0.013	-0.305	0.132	1.0	-0.219	0.256	-0.261
C_{22}	0.091	0.947	-0.089	-0.219	1.0	-0.664	0.992
S_{22}	0.018	-0.689	0.187	0.256	-0.664	1.0	-0.693
k_2	0.098	0.97	-0.129	-0.261	0.992	-0.693	1.0

Figure 28: Correlation matrix for the different Titan gravity field coefficients obtained in the noiseless test run.

Considering that exactly the same modelling is behind the simulated data and the estimation filter, if the software is properly configured, then it must return the same values. The results presented in Tab. 16 confirms that, indeed, the estimation loop works and successfully reproduces the coefficients of the virtual gravity field. The results of this test, and all tests in this chapter, are achieved after ten global iterations (no arc iterations were performed), although convergence is generally reached after the few first iterations, proving that the approximation developed for the measurement partials suits this problem excellently. As it can be seen in the table, the simulated gravity was a simplified version of the ones estimated by Durante et al. (2019) and van Noort (2021), where the dipole field follows the $J_2/C_{22} = 10/3$ relation (condition for hydrostatic equilibrium) and $k_2 = 0.6$. The RMS of the residuals is marginal, as well as the difference with respect to the *true* parameters of the simulated data, and they can be attributed to numerical rounding errors. This is manifested in the residual plots in Fig. 27, where the discrete jumps between points arise from the limits of the numerical resolution used. The error in estimated position is $\sim 10^{-1}$ m and $\sim 10^{-2}$ mm/s in velocity.

The correlation matrix between the parameters of gravity field of Titan in this noiseless test run is displayed in Fig. 28. Despite the fact that the coefficients are estimated accurately, there are high correlations between J_2, C_{22} and k_2, all coefficients related to the tidal interaction between Saturn and Titan. The correlations are similar to those obtained with GEODYN with both real and simulated data (Figs. 3 and 16) These are very important results, as they finally confirm that this strong coupling in the dipole field is intrinsic to the problem configuration/geometry of the flybys. This correlation matrix was obtained again from the estimation with 5 mHz Gaussian noise, to rule out the possibility that this particular result could be corrupted by the dominance of the numerical noise in the residuals, and exactly the same correlation matrix was found, demonstrating that this result is not a fluke.

4.3 Estimation with noise

After having checked that the estimation filter works as intended, the next test that was performed was to run a simulated estimation where the generated measurements are subjected to noise, in order to see what results can be expected from a more realistic case. Thus, Gaussian noise with constant standard deviation was added to the simulated signal. In reality, the noise power varies depending on the antennae, solar activity, Sun-Earth-probe (SEP) angle and atmospheric conditions, which vary between flybys (Asmar et al., 2005). There could be more realistic ways to model the noise than a normal distribution. However, it is considered that limiting to just simulating a constant noise intensity is still helpful to capture the behaviour of the solution with real data from a noisy channel.

Case	Gaussian noise (5 mHz)	Error true parameters
μ ($\mathbf{km^3/s^2}$)	8978.1520 ± 0.0081	$+0.0132$
k_2	0.588 ± 0.059	-0.012
$J_2 \times 10^6$	30.144 ± 1.225	$+0.144$
$C_{21} \times 10^6$	-0.025 ± 0.117	-0.025
$S_{21} \times 10^6$	0.112 ± 0.222	$+0.112$
$C_{22} \times 10^6$	9.099 ± 0.576	$+0.099$
$S_{22} \times 10^6$	-0.051 ± 0.083	-0.051
RMS residuals	4.986 mHz	

Table 17: Estimated values for the spherical harmonics coefficients and their 1-σ errors obtained from a simulated estimation with Gaussian noise of constant 5 mHz standard deviation. The column on the right represents the error with respect to the parameters used for generating the observables.

The results from the estimation of the same degree and order two simulated gravity field as in the previous section is presented in Tab. 17, but this time with a 5 mHz Gaussian noise, which was the RMS of the residuals when replicating the real estimation performed by van Noort (2021) with GEODYN (Section 2.1). As it can be observed, the field is estimated relatively well in this situation, although the error bars are already quite significant, especially for the very influential μ, as well as for the J_2 and C_{22}. Something remarkable is that k_2, which tends to couple with the other tidal coefficients as it has been seen throughout this study, is correctly captured. This is in strong contrast with the results from GEODYN presented in Chapters 2 and 3 with real and simulated data, where the estimated k_2 went towards unrealistic values. This result contributes to the collection of reasons to suspect that there is some unresolved issue with the estimation setup in GEODYN. In this case, the errors in estimated initial state increase as expected, to $\sim 10^2$ m in position and ~ 10 mm/s in velocity.

The residuals can be regarded in Fig. 29 for flybys T022 and T074. No unmodelled leftover signal can be perceived and just the normal random distribution of points can be seen. The total RMS of the residuals is 4.986 mHz, really close and consistent with the simulated standard deviation. Once again, despite the noise in the data, the approximation used for the measurement partial derivatives proves to work just well for this problem. As mentioned before, the correlation matrix is exactly the same one as in the case without noise, and it practically does not vary across the other cases tested here with different noise levels (the high correlations are inherent).

To test the limits of the capability to estimate the gravity field of Titan when facing noise, ad-

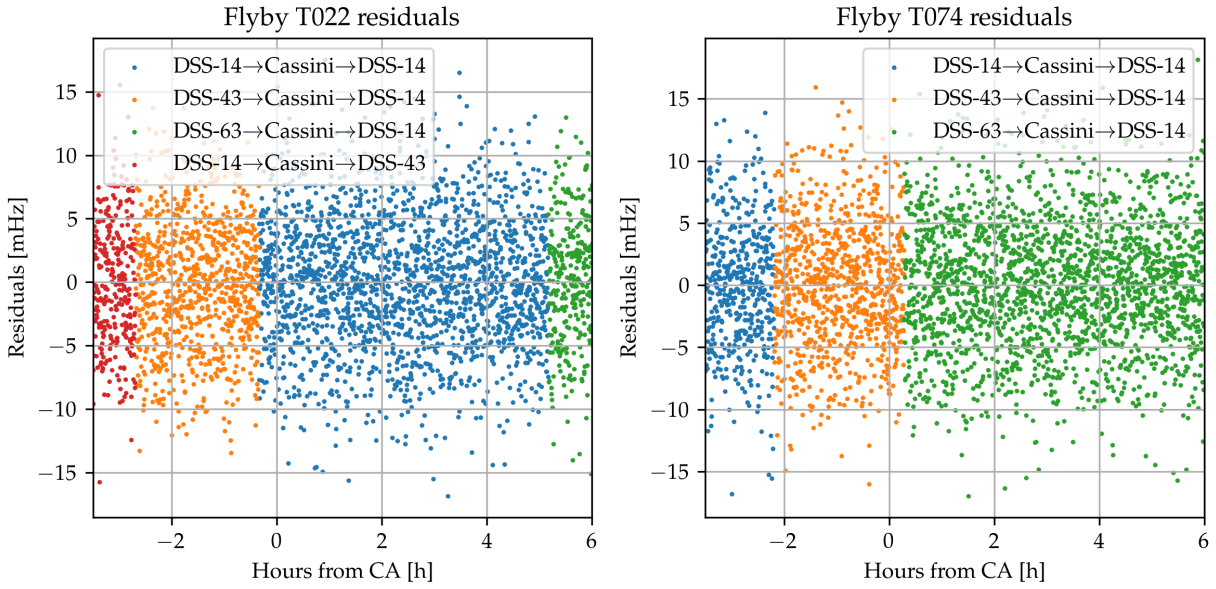

Figure 29: Residual plots of flybys T022 and T074 from the simulated estimation with Gaussian noise of constant 5 mHz standard deviation. The different colours represent the combinations of transmitter and receiver antennae.

ditional simulations were conducted with varying noise powers of 2.5 mHz, 10 mHz, 25 mHz and 100 mHz. The 2.5 mHz standard deviation was chosen in particular because it corresponds to the RMS of the residuals from all flybys reported by Durante et al. (2019). The resulting estimated coefficients are presented in Tab. 18 and, as it can be seen, from 10 mHz onwards the estimation of k_2 fails and corrupts the coefficients. The 1-σ errors become large to the point that for 100 mHz the error for J_2 is almost as large as the value itself. Nevertheless, the estimation filter manages to detect some of the main features of the field and, by looking at the RMS, it can be seen that the signal in the residuals is successfully reduced to the noise level. An interesting result is obtained for the case with 2.5 mHz, despite having half of the noise of the 5 mHz test worse values are obtained. This can be attributed to poorer odds with the generated noise leading to bad estimation of k_2 and the high-correlations doing the rest of the damage, as the seeds used for the random number generator were different in both cases. This illustrates the scope of the impact that uncertainties have in the problem, severely affecting the dipole field even when using the realistic but low noise levels of 2.5 mHz and 5 mHz. Of course, the 1-σ errors are smaller as they are calculated assuming the corresponding reduced uncertainty for the measurements.

Once all this tests with noises were done, an interesting possibility opened up: the current setup allows for the simulation of the 5×5 gravity field estimated by Durante et al. (2019), thus, allowing for an analogous estimation, when knowing the RMS of the residuals achieved in that study (2.5 mHz). This can be used to directly compare the results from these simulations with those from that previous gravity field solution. The outcomes from those tests are presented Tab. 19 aside the values for the coefficients by Durante et al. (2019) employed to generate the simulated observables. Looking at the completely unconstrained solution (simply denoted as *simulated estimation*), it can be clearly noticed how it disagrees with the one from Durante et al. (2019) even at the dipole field, presenting a strong disagreement in k_2. The 1-σ uncertainties are also significantly larger (around four times for J_2), and are similar in magnitude to those obtained by van Noort (2021). This large error in estimated k_2 and greater uncertainties in general did not manifest in the previous 2.5 mHz noise 2×2 solution, indicating that estimating up to degree and order five greatly increases the uncertainties in the dipole field, especially those of J_2, C_{22} and k_2. Looking at the correlation matrix in Fig. 30 it can be seen how it is similar to the one from the previous tests with slightly higher correlations resulting from estimating more parameters. Even with a different

Noise	**2.5 mHz**	**10 mHz**	**25 mHz**	**100 mHz**
μ **(km^3/s^2)**	8978.1428 ± 0.0040	8978.1259 ± 0.0161	8978.1478 ± 0.0403	8978.1738 ± 0.1611
k_2	0.567 ± 0.029	0.199 ± 0.118	1.101 ± 0.294	0.787 ± 1.177
$J_2 \times 10^6$	30.868 ± 0.612	38.198 ± 2.449	19.813 ± 6.123	33.073 ± 24.494
$C_{21} \times 10^6$	0.091 ± 0.058	0.074 ± 0.234	0.504 ± 0.584	1.800 ± 2.338
$S_{21} \times 10^6$	0.061 ± 0.111	0.064 ± 0.445	0.950 ± 1.112	-0.316 ± 4.448
$C_{22} \times 10^6$	9.327 ± 0.288	12.788 ± 1.152	3.599 ± 2.880	4.758 ± 11.521
$S_{22} \times 10^6$	-0.016 ± 0.041	0.618 ± 0.165	-0.757 ± 0.413	1.192 ± 1.653
RMS residuals	2.496 mHz	9.978 mHz	25.023 mHz	99.887 mHz

Table 18: Estimated values for the spherical harmonics coefficients and their 1-σ errors obtained from simulated estimations with Gaussian noise of 2.5 mHz, 10 mHz, 25 mHz and 100 mHz standard deviation.

simulated field the high correlations in the dipole field persist.

Seeing the small standard deviation for μ in the previous study, it can be argued that a strong a priori constraint was used by Durante et al. (2019). Although no mention of such a constraint is reported in the publication of the study, at first glance it is not unreasonable to restrict the value of the gravitational parameter given the available previous literature (Iess et al., 2012; Iess et al., 2010). To just emulate the most optimistic case, another estimation was executed but this time setting μ to be exactly equal to the value utilised for constructing the data and not estimating it (labelled *constrained* μ in Tab. 19). It can be seen that the estimated values become more accurate, but still the 1-σ spreads are much larger than those provided by Durante et al. (2019). The k_2 Love number is estimated well but there are disagreements in the values for S_{21} and S_{31}. The fourth and fifth degree coefficients are surprisingly compatible in general (in terms of overlapping error bars), although the values up to which the filter converges are notably different and the statistical errors larger overall.

The fact that the optimistic case with constrained gravitational parameter still has large error bars for J_2 and C_{22} compared to the Durante et al. (2019) could be explained by some more constraints being applied. Constraints like the hydrostatic equilibrium relation $J_2/C_{22} = 10/3$ or Kaula's rule could lead to a reduced σ in the dipole coefficients. However, in the article it is stated that neither of those relationships were imposed on the solution. The only constraint that is mentioned is an a priori constraint on the initial state of Cassini of 2 km in position and 2 cm/s in velocity sigmas. The last estimation that was performed here incorporated that restriction (*constrained* μ *and* $\boldsymbol{X}_0$). It can be noticed how the estimated values become worse than in the previous case. It must be noted that there is a caveat: even though the constraint was added on the initial state, the initial guess also had some error on purpose. For this simulation the deviation of the guess for the initial state in the RTW frame was reduced to a hundredth of the a priori uncertainties, that is to say, to 20 m and 0.2 mm/s. These errors in a priori initial state are not unreasonable coming from the Cassini ephemeris, seeing the uncertainties in other studies (Boone et al., 2017; Stauch et al., 2005) and considering all the errors in estimated initial state that have been registered so far in the simulated estimations (for instance, $\sim$ 10 m error in position and $\sim$ 1 mm/s in velocity for the case with constrained μ). What this result could suggests is that constraining the initial state, although loosely, to an even slightly wrong value can have a severe negative impact on the solution.

Another significant result from this last test is that the 1-σ uncertainty in the most important second-degree coefficients, although reduced thanks to the a priori constraints, are still signif-

Case	Durante et al. (2019)	Simulated estimation	Constrained μ	Constrained μ and X_0
μ (km^3/s^2)	8978.1383 ± 0.0003	8978.1352 ± 0.0043	8978.1383	8978.1383
k_2	0.616 ± 0.067	0.808 ± 0.103	0.632 ± 0.103	0.724 ± 0.068
$J_2 \times 10^6$	33.089 ± 0.609	30.524 ± 2.384	31.622 ± 2.384	31.048 ± 1.484
$C_{21} \times 10^6$	0.513 ± 0.215	0.617 ± 0.224	0.106 ± 0.221	0.953 ± 0.172
$S_{21} \times 10^6$	0.612 ± 0.359	-0.037 ± 0.516	1.667 ± 0.512	0.416 ± 0.282
$C_{22} \times 10^6$	10.385 ± 0.084	8.413 ± 0.976	10.135 ± 0.976	9.554 ± 0.637
$S_{22} \times 10^6$	-0.064 ± 0.066	-0.295 ± 0.142	-0.075 ± 0.142	-0.116 ± 0.088
$J_3 \times 10^6$	-0.179 ± 0.720	0.953 ± 0.885	-0.602 ± 0.883	-0.121 ± 0.634
$C_{31} \times 10^6$	1.481 ± 0.254	0.942 ± 0.291	1.806 ± 0.288	1.315 ± 0.209
$S_{31} \times 10^6$	0.811 ± 0.402	0.157 ± 0.592	2.734 ± 0.584	-0.084 ± 0.393
$C_{32} \times 10^6$	0.183 ± 0.153	0.224 ± 0.265	-0.124 ± 0.261	0.522 ± 0.149
$S_{32} \times 10^6$	-0.027 ± 0.099	-0.019 ± 0.161	0.013 ± 0.160	-0.184 ± 0.103
$C_{33} \times 10^6$	-0.222 ± 0.017	-0.273 ± 0.024	-0.248 ± 0.024	-0.199 ± 0.018
$S_{33} \times 10^6$	-0.226 ± 0.019	-0.248 ± 0.026	-0.268 ± 0.026	-0.208 ± 0.020
$J_4 \times 10^6$	-1.077 ± 1.844	-0.566 ± 2.183	2.253 ± 2.160	-3.563 ± 1.519
$C_{41} \times 10^6$	-0.842 ± 0.299	-0.360 ± 0.361	-0.889 ± 0.361	-1.124 ± 0.237
$S_{41} \times 10^6$	0.191 ± 0.717	0.041 ± 0.902	0.781 ± 0.898	-1.927 ± 0.588
$C_{42} \times 10^6$	0.183 ± 0.107	-0.041 ± 0.157	-0.027 ± 0.155	0.442 ± 0.101
$S_{42} \times 10^6$	0.198 ± 0.106	0.287 ± 0.130	0.335 ± 0.130	0.234 ± 0.083
$C_{43} \times 10^6$	-0.012 ± 0.039	0.030 ± 0.053	-0.084 ± 0.052	0.073 ± 0.037
$S_{43} \times 10^6$	-0.062 ± 0.033	0.004 ± 0.038	-0.116 ± 0.038	-0.174 ± 0.029
$C_{44} \times 10^6$	-0.014 ± 0.003	-0.017 ± 0.004	-0.013 ± 0.004	-0.022 ± 0.004
$S_{44} \times 10^6$	-0.012 ± 0.004	-0.025 ± 0.004	-0.013 ± 0.004	-0.009 ± 0.004
$J_5 \times 10^6$	1.118 ± 2.022	3.121 ± 2.498	1.441 ± 2.497	-0.022 ± 1.805
$C_{51} \times 10^6$	0.361 ± 0.406	0.492 ± 0.446	-0.208 ± 0.445	0.087 ± 0.515
$S_{51} \times 10^6$	0.267 ± 0.604	0.227 ± 0.688	-0.158 ± 0.688	0.267 ± 0.323
$C_{52} \times 10^6$	-0.097 ± 0.118	-0.013 ± 0.137	-0.198 ± 0.136	-0.140 ± 0.096
$S_{52} \times 10^6$	0.044 ± 0.094	0.171 ± 0.127	-0.064 ± 0.127	0.027 ± 0.093
$C_{53} \times 10^6$	-0.016 ± 0.019	-0.064 ± 0.024	-0.028 ± 0.024	0.005 ± 0.013
$S_{53} \times 10^6$	-0.004 ± 0.012	0.004 ± 0.017	-0.011 ± 0.017	-0.009 ± 0.017
$C_{54} \times 10^6$	0.007 ± 0.004	0.015 ± 0.005	-0.002 ± 0.005	-0.007 ± 0.004
$S_{54} \times 10^6$	-0.002 ± 0.004	0.008 ± 0.006	-0.008 ± 0.006	0.019 ± 0.004
$C_{55} \times 10^6$	0.000 ± 0.001	0.001 ± 0.001	-0.001 ± 0.001	-0.002 ± 0.001
$S_{55} \times 10^6$	0.000 ± 0.001	-0.001 ± 0.001	0.001 ± 0.001	-0.001 ± 0.001
RMS residuals	≈ 2.575 mHz	2.491 mHz	2.483 mHz	2.491 mHz

Table 19: Estimated values for the spherical harmonics coefficients when simulating analogous estimations to the one performed by Durante et al. (2019). The gravity field from that study was used to generate the data and the 2.5 mHz RMS of residuals from that study was used for the noise.

icantly larger than the ones reported by Durante et al. (2019), with the exception of k_2 which now shows almost the same uncertainty. It should be emphasised that the estimation analogue presented here is very optimistic, and any statistical uncertainties are considered for the Titan ephemeris, for those of the other astronomical bodies or for the DSN station coordinates. In addition, there is no drag, RTG thermal emissions or solar radiation pressure being simulated, thus less sources for uncertainties (to clear this last point out, the results are independent as the simulated data was generated without them and the simulated estimation would only likely perform worse by adding more parameters). As such, what could justify this disagreement would be the usage of some other constraint in that study which was not pointed out in the publication.

	μ	J_2	C_{21}	S_{21}	C_{22}	S_{22}	k_2
μ	1.0	0.02	0.159	0.124	0.016	-0.017	0.03
J_2	0.02	1.0	0.172	0.593	-0.942	-0.843	-0.956
C_{21}	0.159	0.172	1.0	0.03	-0.03	-0.27	-0.055
S_{21}	0.124	0.593	0.03	1.0	-0.472	-0.311	-0.464
C_{22}	0.016	-0.942	-0.03	-0.472	1.0	0.844	0.993
S_{22}	-0.017	-0.843	-0.27	-0.311	0.844	1.0	0.869
k_2	0.03	-0.956	-0.055	-0.464	0.993	0.869	1.0

Figure 30: Correlation matrix for the different Titan gravity field coefficients obtained in the degree and order five simulated estimation analogous to the one performed by Durante et al. (2019).

4.4 Impact of unaccounted relativistic effects

It can be recalled that when performing the verification tests of the GEODYN setup described in Chapter 3 it was hypothesised that a possible cause for the large signal observed in the residuals could be due to mismatches in how the relativistic effects were being accounted for when processing the data. It was concluded that they have an important impact in the solution. Here, having the possibility to simulate the entire estimation chain allows for testing that.

Tab. 20 shows the results when estimating the point-mass gravity of Titan when no relativistic corrections are being applied in the estimation model. In other words, the simulated data is being generated with all the relativistic effects turned on but they are disabled in the measurement model of the estimation filter. A 5 mHz Gaussian noise was also applied to the simulated observables. The variations in RMS of residuals of ∼100-200 mHz seen in Section 3.2 are not reproduced here (the change is of ∼300 mHz), meaning that the signal is absorbed by the parameters in a different manner in both setups. Nevertheless, large and unfeasible values for the coefficients are also obtained as the estimation filter fails to fit such a strong signal arising from the mismatch in models. The error in the estimated initial state is large as well: $\sim 10^4$ m in position and $\sim 10^3$ mm/s in velocity. This result confirms what was already discussed about the important role of the relativistic effects in Section 3.1 when studying and comparing the expected magnitude of the signal from some of the important spherical harmonics coefficients of Titan with that of the influence of relativity on the measurements.

As it can be seen in the residuals presented in Fig. 31, the gravity model is not capable of absorbing the relativistic signal. This is a good property of the problem, as it means that the signals do not correlate well and can be resolved. This behaviour also is attributable to the different nature and scope of the signals: the spherical harmonics only can manifest in the Doppler really close to Titan, while the relativistic effects are strong at all moments. As the spherical harmon-

Case	Null field	$J_2 = 30 \cdot 10^{-6}$	$C_{22} = 9 \cdot 10^{-6}$	$k_2 = 0.6$
	Values			Differences in coefficients
μ (km^3/s^2)	8974.8857 ± 0.0084	-0.0117	-0.0182	$+0.0101$
k_2	57.221 ± 0.059	-0.005	$+0.023$	$+0.548$
$J_2 \times 10^6$	-1233.612 ± 1.223	$+30.232$	$+0.001$	$+0.501$
$C_{21} \times 10^6$	-25.426 ± 0.116	-0.025	-0.063	-0.085
$S_{21} \times 10^6$	375.786 ± 0.224	-0.712	-0.038	-0.111
$C_{22} \times 10^6$	-591.842 ± 0.574	-0.008	$+8.733$	$+0.539$
$S_{22} \times 10^6$	-42.694 ± 0.083	$+0.029$	-0.084	$+0.001$
RMS residuals	364.680 mHz	364.730 mHz	364.690 mHz	364.636 mHz

Table 20: Estimated values for the spherical harmonics coefficients obtained from simulated estimations where the relativistic effects were not accounted for and with 5 mHz noise. Different simulated gravity fields where tested and the variations in coefficients are presented with respect to the case with a point-mass gravity.

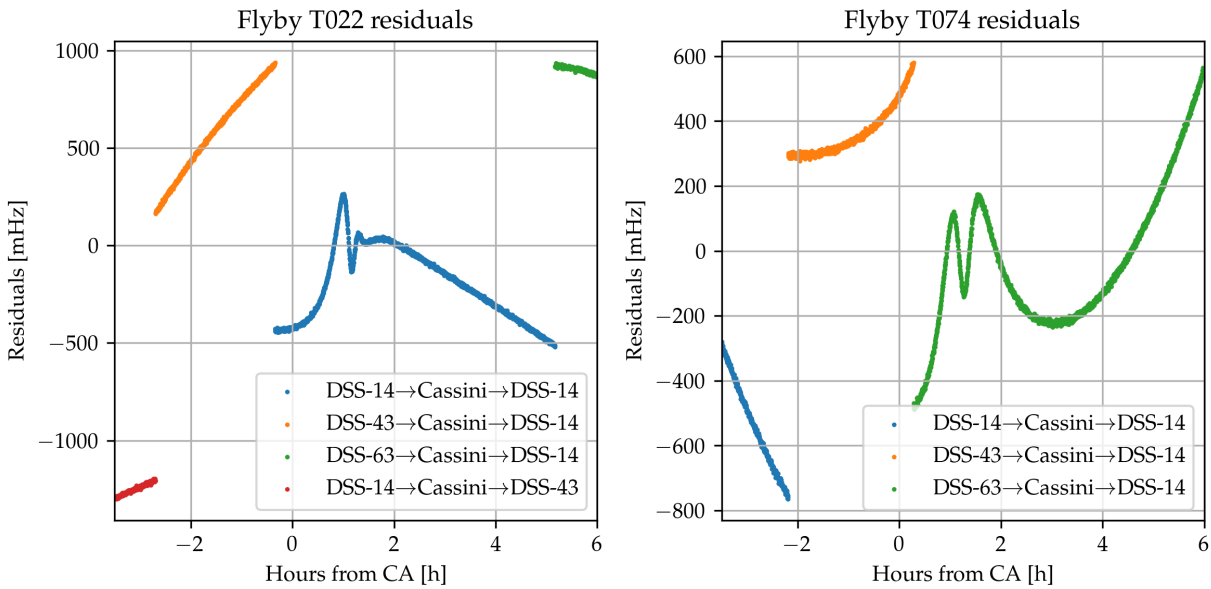

Figure 31: Residual plots of flybys T022 and T074 from the test where the relativistic effects were not accounted for and a point-mass gravity was considered for Titan.

ics can reduce the residuals just at the closest approach, any fault in the measurement modelling manifests as poor residuals when the spacecraft is far from the moon, so mistakes can be spotted more easily. Important jumps between different antennae can be seen, like observed with GEODYN with real and simulated data (for example, Figs. 4 and 17). Interestingly, as seen in the tests with GEODYN, despite the large residuals and radically different solution, the correlation matrix does not change much and shows similar features of high correlation between J_2, C_{22} and k_2. As mentioned several times before, this is another testament of both the intrinsic correlations in this problem and how linearly it behaves.

It has not been discussed yet that, similarly to what was done in Section 3.2.1 with GEODYN and the simulated data, the variation in estimated coefficients when changing the simulated grav-

	μ	J_2	C_{21}	S_{21}	C_{22}	S_{22}	k_2
μ	1.0	0.083	0.118	-0.01	0.091	0.002	0.098
J_2	0.083	1.0	-0.217	-0.312	0.946	-0.697	0.969
C_{21}	0.118	-0.217	1.0	0.139	-0.104	0.185	-0.144
S_{21}	-0.01	-0.312	0.139	1.0	-0.223	0.26	-0.266
C_{22}	0.091	0.946	-0.104	-0.223	1.0	-0.672	0.992
S_{22}	0.002	-0.697	0.185	0.26	-0.672	1.0	-0.701
k_2	0.098	0.969	-0.144	-0.266	0.992	-0.701	1.0

Figure 32: Correlation matrix for the different Titan gravity field coefficients obtained in the test where the relativistic effects were not accounted for and a point-mass gravity was considered for Titan.

ity field is presented in Tab. 20. Indeed, the same linear behaviour is replicated, where despite a large bias in the estimated coefficients because of the mismodelled signal, the variations in all the simulated field are captured quite well by the estimation filter. Just like in those tests, the change in the RMS of the residuals across the different cases is negligible, implying that the additional Doppler signal is correctly absorbed by its corresponding spherical harmonics coefficient.

4.5 Effects of unaccounted timing bias

A possible source for model mismatch that was not discussed much in Chapter 3 is improper timing. The influence of errors in the times used for the ephemeris in transmission, signal turnaround by Cassini (there could also be some transponder delay), and reception back at the Earth can lead to an enormous fictitious Doppler signal, its magnitude being related to the derivative of the Doppler shift times the incorrect timing bias.

Just as in the previous section, the null field was estimated and also the changes in coefficients when varying the simulated gravity field, but here with the mismatch being a +1 s error in the timestamps of the observed signal frequency by the receiver ground station. A 5 mHz Gaussian noise was also added to the Doppler shift. As argued when describing the new estimation filter, the reason behind just testing a bias in reception time instead of in transmission or turnaround is because it is considered to be enough for capturing the behaviour and consequences of timing problems in general and it was easy to implement in the estimation software.

As it can be observed in Tab. 21, the one-second error leads to a quite significant RMS of the residuals of around 80 mHz and a poor estimation of the gravity field coefficients. Again, the error in initial state is significant: $\sim 10^3$ m in position and $\sim 10^2$ mm/s in velocity. This illustrates how important is to get the timings correctly in a gravity determination problem. It is curious to see

Case	Null field	$J_2 = 30 \cdot 10^{-6}$	$C_{22} = 9 \cdot 10^{-6}$	$k_2 = 0.6$
	Values		Differences in coefficients	
μ (km^3/s^2)	8978.1414 ± 0.0081	-0.0035	$+0.0050$	$+0.0104$
k_2	-11.369 ± 0.059	-0.105	-0.109	$+0.379$
$J_2 \times 10^6$	183.940 ± 1.223	$+32.579$	$+3.020$	$+4.776$
$C_{21} \times 10^6$	2.646 ± 0.117	$+0.063$	$+0.083$	$+0.193$
$S_{21} \times 10^6$	71.283 ± 0.222	-0.461	-0.532	-0.427
$C_{22} \times 10^6$	114.563 ± 0.576	$+0.851$	$+10.037$	$+1.980$
$S_{22} \times 10^6$	-0.898 ± 0.083	$+0.109$	$+0.101$	$+0.303$
RMS residuals	80.781 mHz	80.756 mHz	80.802 mHz	80.842 mHz

Table 21: Estimated values for the spherical harmonics coefficients obtained from simulated estimations with a +1 s error in receiver timestamps and with 5 mHz noise. Various simulated gravity fields where tested and the changes in coefficients are presented with respect to the case with a point-mass gravity. Different seeds were used for the random number generator in each case.

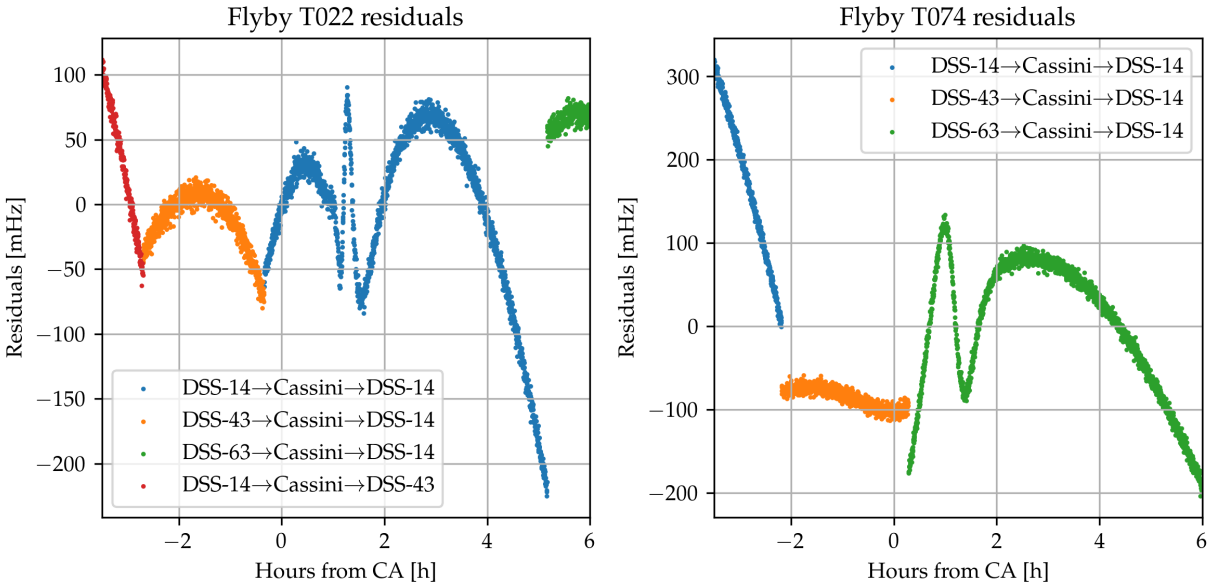

Figure 33: Residual plots of flybys T022 and T074 from the test with a +1 s error in receiver timestamps, 5 mHz noise and a simulated point-mass gravity for Titan.

how k_2 is large and positive when the relativistic effects are unaccounted and large and negative with a positive timing error. Looking at the residuals (Fig. 33), it can be noticed how they present a kind of curvy profile and the relative jumps between antennae combinations are much smaller compared to those seen in the residuals from test with the unaccounted relativistic effects. Also the correlation matrix, depicted in Fig. 34, looks like as all the previous ones with only small changes in the matrix elements.

As mentioned before, the procedure to check whether the differences in simulated gravity field are detected by the estimation loop was also applied to this case to check if the problem still behaved linearly when messing with timings. If that would not be the case, then the possibility that the large residuals seen in Section 3.2 could be attributed to some timing offset could be

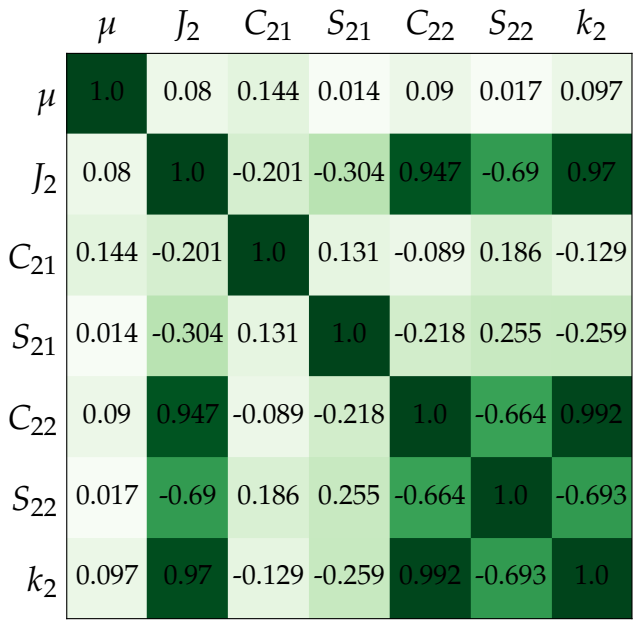

Figure 34: Correlation matrix for the different Titan gravity field coefficients obtained in the test with a +1 s error in receiver timestamps, 5 mHz noise and a simulated point-mass gravity for Titan.

discarded, as then the results in Section 3.2.1, where the changes in coefficients where captured with striking accuracy, should not be possible. In Tab. 21 the RMS of the residuals are almost the same in all cases, meaning that the difference in signal is absorbed. However, the changes in coefficients are not estimated so well, especially for k_2 (where a change of 0.379 is detected instead of the 0.6 one in the simulated field). With these results it can be tempting to assume that, in effect, the filter stops showing the strong linear behaviour when facing timing errors. But there is a catch in those results. The simulated data for the different cases was generated changing the seeds for the random number generator behind the normally distributed noise imposed on the Doppler observables. This means that there is some variability between the tests, where maybe on some of the important points end up in a more favourable value for a correct estimation than in others. This is just what was discussed in Section 4.3 about how uncertain can the solution be and the strong influence of the realization of the noise when the coefficients are so highly correlated.

In order to generate the Gaussian noise, NumPy's (Harris et al., 2020) normal distribution function was used with the PCG-64 random number generator algorithm (O'Neill, 2014). Instead of using different seeds each time, the estimations from Tab. 21 were re-run again but this time with the same numeric seeds (number forty two plus the flyby chronological count starting at zero to seed each flyby). The new results are displayed in Tab. 22 and it can be observed how the field variations are well detected now, demonstrating that the problem is also strongly linear in time, even with a considerable one-second timing error (thus, almost three million kilometres of light-path). What this implies is that timing errors cannot be discarded as one of the possible sources for the mismatches observed in the tests with GEODYN.

To finish this section, the impact of the timing bias on the solution was mapped by conducting a few more tests with 1 ms, 10 ms and 100 ms downlink delays. Looking at Tab. 23 it can be seen how the estimations with 1 ms and 10 ms are capable of reaching the noise level in the residuals (5 mHz), although already at 10 ms the true solution is outside the error intervals of the estimated values. The magnitude of the residuals is doubled when jumping to 100 ms and the offset in the

Case	Null field	$J_2 = 30 \cdot 10^{-6}$	$C_{22} = 9 \cdot 10^{-6}$	$k_2 = 0.6$
	Values			Differences in coefficients
μ (km^3/s^2)	8978.1436 ± 0.0081	$+0.0016$	$+0.0010$	$+0.0014$
k_2	-11.468 ± 0.059	-0.002	-0.003	$+0.597$
$J_2 \times 10^6$	186.818 ± 1.223	$+30.060$	$+0.074$	$+0.079$
$C_{21} \times 10^6$	3.038 ± 0.117	-0.001	$+0.000$	$+0.000$
$S_{21} \times 10^6$	70.281 ± 0.222	-0.017	-0.012	-0.014
$C_{22} \times 10^6$	115.346 ± 0.576	$+0.026$	$+9.033$	$+0.035$
$S_{22} \times 10^6$	-0.730 ± 0.083	-0.002	$+0.002$	$+0.000$
RMS residuals	80.820 mHz	80.821 mHz	80.820 mHz	80.821 mHz

Table 22: Estimated values for the spherical harmonics coefficients obtained from simulated estimations with a +1 s error in receiver timestamps and with 5 mHz noise. Various simulated gravity fields where tested and the changes in coefficients are presented with respect to the case with a point-mass gravity. The same seeds were used for the random number generator in each case.

estimated values for the dipole field is significantly large. All of these results prove the point that timing has a colossal influence in the estimation and, as such, it must be carefully controlled, at least up to the millisecond level.

Noise	1 ms	10 ms	100 ms
μ (km^3/s^2)	8978.1412 ± 0.0081	8978.1497 ± 0.0081	8978.1331 ± 0.0081
k_2	-0.050 ± 0.059	-0.258 ± 0.059	-1.192 ± 0.059
$J_2 \times 10^6$	1.330 ± 1.224	5.016 ± 1.224	19.501 ± 1.224
$C_{21} \times 10^6$	0.090 ± 0.117	0.270 ± 0.117	0.095 ± 0.117
$S_{21} \times 10^6$	-0.155 ± 0.222	0.206 ± 0.222	7.025 ± 0.222
$C_{22} \times 10^6$	0.365 ± 0.576	2.506 ± 0.576	12.032 ± 0.576
$S_{22} \times 10^6$	0.097 ± 0.083	0.062 ± 0.083	-0.108 ± 0.083
RMS residuals	5.024 mHz	5.046 mHz	9.554 mHz

Table 23: Estimated values for the spherical harmonics coefficients obtained from simulated estimations with 1 ms, 10 ms and 100 ms positive error in receiver timestamps, with 5 mHz noise and a simulated point-mass gravity field for Titan.

4.6 Estimation prospects with real data

After implementing and setting up a whole (basic) estimation loop, the question of why it was not tested with the real data is raised. The reason for this is that reading and preprocessing the raw frequency data binary files from the DSN stations is not a straightforward process. It must be noted that the data was stored in a format that ensured backwards compatibility with metric tracking data preprocessing software used at NASA (Moyer, 2005). It is certainly possible to feed

the real data to the estimation filter developed here and an attempt was made to do so for this project (following the guidelines in O'Dea and Bryant, 2015). However, this requires complex modelling of the ramp integrals, as the Doppler data from the DSN is ramped, which means that the transmitter frequency is linearly increased at intervals on purpose. The data processing also requires removing outliers and estimating frequency biases because, as it has been observed, even a mismatch of a few Hertz can be catastrophic for the estimation. Any possible path delays (interplanetary plasma, ionosphere, troposphere) and timing issues must also be computed.

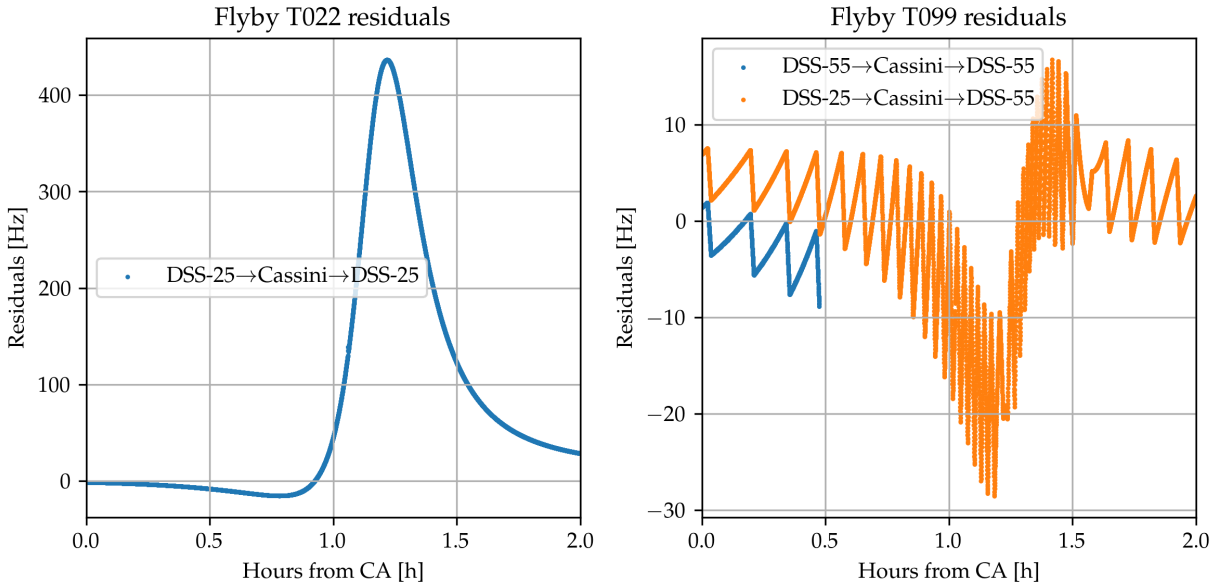

Figure 35: Residual plots of flybys T022 and T074 when feeding the real data to the estimation setup and performing one iteration, so the orbit is not updated, with the point-mass gravity of Titan as initial guess. Timing bias of -50 s was applied to manually reduce the signal in T099.

A few simple tests were made comparing the modelled Doppler signal for the point-mass gravity field of Titan with the real Doppler signal (running just one iteration of the estimation loop). The residuals were in the order of 10-100 Hz (Fig. 35), which at least demonstrates that the effort of making the real data compatible is going in the right direction, especially when considering that the received frequencies are in the order of 10^9 Hz and the total Doppler shift from a flyby is around 10^6 Hz (remember Fig. 7), but still it is insufficient for gravity determination. It must be pointed out that the residuals showed serious improvement when manually tuning timing biases for each flyby individually, but the estimation setup needs to be further developed to operate with the real data. For instance, the residuals for flyby T099 shown in Fig. 35 were significantly reduced from hundreds to tens of Herz by setting a -50 s receiver timing bias, but such bias did not work for other flybys like T022 in the figure, suggesting that the timing offsets would need to be determined individually for each of the flybys or even antennae combinations. The saw profile in the residuals of T099 also implies that the received Doppler signal is not properly matched with the ramped transmitter signal that gave rise to it. To solve this issue, the delays in uplink, turnaround and downlink would need to all be determined simultaneously. Also the data in reality consists of a Doppler cycle count compressed in one second time intervals, not an instantaneous frequency, and the impact of that distinction is yet to be determined (hence the need of implementing the ramp integrals when working with DSN observables).

Summarising this chapter, a new estimation setup was constructed over the functionalities for orbital trajectory propagation and variational equations provided by Tudat, as well as the software implementation done for this project for modelling the fully relativistic Doppler observables and a global inversion script for obtaining a multi-arc solution. A classical approximation for the two-way Doppler measurement partial derivatives was derived and tested, successfully driving

the estimation filter towards convergence in the true simulated values for the parameters. Simulated estimations have been performed with equivalent noise powers as those reported in the earlier works of Durante et al. (2019) and van Noort (2021), with the post-fit residuals showing no leftover signal but the estimated coefficients presenting large uncertainties. It has finally been proven that the high correlation within the dipole field between J_2, C_{22} and k_2 is inherent to the flyby geometry and available data. This strong coupling between parameters seems to be causing the solution to be very susceptible to noise. A few simulated estimations have been performed emulating the degree and order five gravity determination conducted by Durante et al. (2019). Some disagreement has been found in both the parameter 1-σ uncertainties and the observed prospects of obtaining a realistic solution up to such a high degree when facing the same noise standard deviation as the RMS of the residuals achieved in that work. Finally, the consequences of unaccounted relativistic effects and timing errors have been characterised and checked to be highly important. They show the same linear behaviour described in Chapter 3 and they can be part of what was causing the large residuals that were being obtained with the GEODYN setup.

5 Conclusion

In this study the problem of the determination of the gravity field of Titan from Cassini Doppler data has been reviewed following the previous estimations conducted by Durante et al. (2019) and van Noort (2021). The GEODYN setup used by van Noort (2021) was carefully tested with the real Cassini two and three-way X-band Doppler data from NASA's DSN to find ways of improving the solution. In his study, van Noort (2021) was not able to estimate the second degree Love number k_2. Here, that issue was replicated by checking how with the setup using GEODYN k_2 tends to unfeasible negative values. The usage of inequality constraints has been proposed and tested in the present work as a solution to such problem, as from theoretical considerations it is known as a fact that k_2 must be positive. These special constraints proved to work as intended, but they were unsuccessful in driving the solution away from such a strong attractor in the parameter space. This result can be explained by the widely linear behaviour of the problem that was later proved. The fact that, with this strong linearity, an unfeasible solution is obtained points out to the presence of some error in the model. The empirical accelerations were large, and without them the estimated k_2 became positive. However, in that situation the residuals were large and presented a linear trend which caused the estimated coefficients to be unrealistic. It was found that a strong correlation between the tidal coefficients J_2, C_{22} and k_2 existed when trying to estimate k_2.

In order to verify the GEODYN setup, a model was set up for simulating two-way Doppler observables which were then given as input data to the estimation filter in GEODYN. The setup was unable to correctly estimate the simulated coefficients. A large residual signal was again obtained when fitting the simulated data, in the order of 10^2 mHz. Different elements of the model, which included the position and reference frame of Titan, empirical accelerations, frequency biases, atmospheric effects, relativistic effects and the ephemeris of the relevant astronomical bodies, were tested. The most influential ones where empirical accelerations, measurement biases and relativistic corrections, affecting the residuals by an order of 10^2 mHz. Regarding the relativistic effects, their magnitude was calculated when generating the simulated data and compared to the expected signal from some of the most relevant gravity coefficients. These effects were checked to be certainly impactful for the estimation of the dipole field. Less important phenomena, yet relevant for future projects in which the greater mismatches are corrected, were the atmospheric corrections and the way the position of Titan was propagated, with a 1 mHz effect. Unfortunately, none of them could account for the large remaining residuals. These residuals were found to present strange features like an artificial dispersion of points consisting of inexplicable regular jumps that were tested to be not attributable to integration errors. Nevertheless, the estimation setup with GEODYN was able to capture accurately the differences in simulated field despite presenting a large offset in the estimated coefficients, demonstrating that, despite the mismodelling, the underlying estimation filter was performing well. This fact also serves as proof of the strongly linear behaviour of the problem. The orbits propagated with GEODYN and Tudat were compared and it was discovered that the GEODYN implementation was miscalculating the acceleration from Saturn when the routine to include its spherical harmonics was active. However, after disabling the Saturnian harmonics in both GEODYN and the Tudat model, erratic jumps in the acceleration calculated by GEODYN became apparent. In spite of the difference in acceleration being small enough to allow for the estimation of the second degree coefficients after the modifications, the attempts to reproduce the simulated gravity field with GEODYN ended in failure, suggesting that

there are mismatches in how the estimation is performed by the two models. Thus, if a future study is to be carried out using this GEODYN configuration, first the calculation of the spherical harmonics acceleration from Saturn should be fixed, and the cause for the discontinuities in acceleration should be cleared out. Then the estimation model must be reviewed, starting with the most relevant contributions to the residuals that have been found, that is to say, the definition of the empirical accelerations, measurement biases and relativistic corrections. It is suggested to compare them to their simulated effects for verifying them, much like it has been done in this study.

An new estimation filter was constructed so the fundamental behaviour of this gravity determination problem could be studied independently from the issues that were discovered in the GEODYN setup. This new setup is able to generate noisy simulated data and then propagate the orbit, simulate the measurements and perform the least-squares estimation of the arc and global parameters iteratively. It is based on the functionality provided by Tudat and the software for simulating the relativistic Doppler observables. The new estimation filter uses a non-relativistic approximation of the measurement partial derivatives which was tested to work excellently for this problem. Using this tool, different simulated estimations emulating the real determination problem were conducted. The results confirmed that the filter behaves very linearly and consistently reduces the residuals to the noise level even when employing poor initial guesses for Titan's gravitational parameter and the initial states for Cassini. Most importantly, it was finally proven that the strong correlation between the J_2, C_{22} and k_2 coefficients is inherent to the geometry of the ten flybys that were considered in both the Durante et al. (2019) and van Noort (2021) studies. An estimation was performed with a noise power similar to the RMS of the residuals achieved with the GEODYN setup used by van Noort (2021) and it was found that the k_2 Love number could be correctly estimated, unlike in the previous gravity determination with GEODYN. Nevertheless, it was observed that the uncertainties in the estimated coefficients were similar to those obtained by van Noort (2021) but quite large compared to those of Durante et al. (2019), especially for the J_2, C_{22} and k_2 coefficients, most likely because of the strong correlations. The estimation performed by Durante et al. (2019) was also simulated using the same gravity field, noise and estimating up to degree and order five. The results from those tests did not agree in terms of uncertainties, which were much larger than those reported in that study despite the emulated cases being very optimistic in terms of estimating a reduced set of parameters and with model variances. Also it was seen that, when estimating to such degrees and orders, the noise made it difficult to obtain a realistic solution. The impact on the solution caused by model mismatches like unaccounted relativistic effects and timing errors was studied. It was found that timing errors cannot be discarded as a possible cause for the mismatch found between the GEODYN and the simulated data models. Thus, if a new estimation effort is to be performed, it is strongly recommended to carefully check that the transmission, spacecraft turnaround and reception times are correct up to the level of at least 10 ms, as evaluated in this study. This could be attempted by estimating path delays both during uplink and downlink based on refraction models and measurements and/or on matching the changes in frequency ramp present in the Doppler measurements produced by the DSN. In any case, the sensibility of the solution to changes in timing should always be tested in order to assess the accuracy of the solution.

In conclusion, in order to improve over the previous gravity determination attempts, the models and constraints used for the estimation filters first need to be reviewed with great care. In particular, in the case of the GEODYN implementation, the orbit propagation with Saturn's spherical harmonics has to be inspected and the configuration for the empirical accelerations, measurement biases and relativistic corrections checked. For the estimation problem in general, correct timings in the measurement model have been found to be critical in order to obtain an accurate solution. It has been found that the problem as formulated is fundamentally quite unfavourable in nature for obtaining realistic values for the gravity field coefficients given the noises and uncertainties in the available Doppler data from Cassini. The only way then to reduce the uncertainties is though the

addition of constraints in the parameter space. It must be warned for future estimation attempts that these constraints have to be well grounded and handled with extreme care. This is because it was tested in the simulations that, for instance, even a small error in the a priori state, of a hundredth of its uncertainty, can severely disrupt the estimated values for the gravity coefficients. An example of what those constraints could consist of would be delving into geophysical considerations that could establish relationships between gravity coefficients (like the $k_2 > 0$ explored here) or constrain other parameters like the atmospheric density for drag. A way to further constrain the very influential and highly correlated k_2 could be through simulations of the tidal response of Titan using finite elements method models of the potential internal structures of the moon (some of which are explored in Grasset et al., 2000). Inconsistencies have been found when comparing the solutions from Durante et al. (2019) and van Noort (2021) to simulated data and complete simulated estimations. Those regard the small uncertainties given the reported noise level in the first study and the inability to estimate k_2 in the second one despite it being possible in the simulated estimations. A more profound revision of these inconsistencies is considered to be the necessary starting point for any future work that wants to attempt to obtain a more accurate solution to the gravity field of Titan. This research hopes to have provided indications about the parts of the model that are more relevant for inspection and a tool for verifying the estimation setup based on simulation. With this study, the power of performing simulations of the estimation procedure has been highlighted, as it can be really important to understand the limitations of the orbit determination problem being tackled. The methodologies and software used and developed here can be used for estimating gravity fields of other visited bodies in the Solar system. Another interesting possibility to explore in a future study is how the estimation can benefit from the use of a Kalman filter. As one last recommendation for future applications, the capability developed here to simulate gravity fields, flybys, measurements, and the estimation of coefficients can be used the other way around: instead of using it to assess the quality of existing data sets, it can guide the trajectory design of future gravity determination missions in order to obtain an optimal coverage of the body to be studied and maximise the scientific output. The ultimate goal of the knowledge of Titan's gravity field is not only for orbit propagation, but also to provide clues about its interior, the properties of an internal ocean, its formation, and the formation of the Solar system.

Bibliography

Acton, C. H. (1996). Ancillary data services of NASA's navigation and ancillary information facility. *Planetary and Space Science*, *44*(1), 65–70.

Andrade, L. G. (2018). Skimming through Saturn's Atmosphere: The Climax of the Cassini Grand Finale Mission. *2018 AIAA Guidance, Navigation, and Control Conference*, 2111.

Asmar, S. W., Armstrong, J. W., Iess, L., & Tortora, P. (2005). Spacecraft Doppler tracking: Noise budget and accuracy achievable in precision radio science observations. *Radio Science*, *40*(2).

Bertotti, B., Iess, L., & Tortora, P. (2003). A test of general relativity using radio links with the Cassini spacecraft. *Nature*, *425*(6956), 374–376.

Bocanegra-Bahamón, T., Calvés, G. M., Gurvits, L., Duev, D., Pogrebenko, S., Cimò, G., Dirkx, D., & Rosenblatt, P. (2018). Planetary radio interferometry and Doppler experiment (PRIDE) technique: a test case of the mars express phobos flyby-II. Doppler tracking: formulation of observed and computed values, and noise budget. *Astronomy & Astrophysics*, *609*, A59.

Boone, D., Bellerose, J., & Roth, D. (2017). Resolution of orbit determination prediction instabilities at Titan during Cassini's Solstice mission.

Boucher, C., Altamimi, Z., & Duhem, L. (1994). Results and analysis of the ITRF93. *IERS Technical note*, *18*, 1–313.

Corlies, P., Hayes, A. G., Birch, S. P. D., Lorenz, R., Stiles, B. W., Kirk, R., Poggiali, V., Zebker, H., & Iess, L. (2017). Titan's topography and shape at the end of the Cassini mission. *Geophysical Research Letters*, *44*(23), 11–754.

De Pater, I., & Lissauer, J. J. (2019). *Fundamental Planetary Science : physics, chemistry, and habitability*. Cambridge University Press.

Di Ruscio, A., Fienga, A., Durante, D., Iess, L., Laskar, J., & Gastineau, M. (2020). Analysis of Cassini radio tracking data for the construction of INPOP19a: A new estimate of the Kuiper belt mass. *Astronomy & Astrophysics*, *640*, A7.

Dirkx, D., Mooij, E., & Root, B. (2019). Propagation and estimation of the dynamical behaviour of gravitationally interacting rigid bodies. *Astrophysics and Space Science*, *364*(2), 1–22.

Durante, D., Hemingway, D. J., Racioppa, P., Iess, L., & Stevenson, D. J. (2019). Titan's gravity field and interior structure after Cassini. *Icarus*, *326*, 123–132.

Ermakov, A. I., Park, R. S., & Bills, B. G. (2018). Power laws of topography and gravity spectra of the solar system bodies. *Journal of Geophysical Research: Planets*, *123*(8), 2038–2064.

Feissel, M., & Mignard, F. (1998). The adoption of ICRS on 1 January 1998: meaning and consequences. *Astronomy and Astrophysics*, *331*, L33–L36.

Folkner, W. M., Williams, J. G., Boggs, D. H., Park, R. S., & Kuchynka, P. (2014). The Planetary and Lunar Ephemerides DE430 and DE431: IPN Progress Report 42-196. *Jet Propulsion Laboratory, California Institute of Technology, http://ipnpr.jpl.nasa.gov/progressreport/42-196C*, *196*.

Grasset, O., Sotin, C., & Deschamps, F. (2000). On the internal structure and dynamics of Titan. *Planetary and Space Science*, *48*(7), 617–636.

Harris, C. R., Millman, K. J., van der Walt, S. J., Gommers, R., Virtanen, P., Cournapeau, D., Wieser, E., Taylor, J., Berg, S., Smith, N. J., Kern, R., Picus, M., Hoyer, S., van Kerkwijk, M. H., Brett, M., Haldane, A., del Río, J. F., Wiebe, M., Peterson, P., … Oliphant, T. E. (2020). Array programming with NumPy. *Nature*, *585*(7825), 357–362.

Hubbard, W. B., & Anderson, J. D. (1978). Possible flyby measurements of Galilean satellite interior structure. *Icarus*, *33*(2), 336–341.

Hunten, D. M., Tomasko, M. G., Flasar, F. M., Samuelson, R. E., Strobel, D. F., & Stevenson, D. J. (1984). Titan. *Saturn*, 671–759.

Iess, L., Armstrong, J. W., Asmar, S. W., Di Benedetto, M., Graziani, A., Mackenzie, R., Racioppa, P., Rappaport, N., & Tortora, P. (2007). The determination of Titan gravity field from Doppler

tracking of the Cassini spacecraft. *Proceedings of the 20th International Symposium on Space Flight Dynamics*.

Iess, L., Jacobson, R. A., Ducci, M., Stevenson, D. J., Lunine, J. I., Armstrong, J. W., Asmar, S. W., Racioppa, P., Rappaport, N. J., & Tortora, P. (2012). The tides of Titan. *Science*, *337*(6093), 457–459.

Iess, L., Militzer, B., Kaspi, Y., Nicholson, P., Durante, D., Racioppa, P., Anabtawi, A., Galanti, E., Hubbard, W., Mariani, M. J., et al. (2019). Measurement and implications of Saturn's gravity field and ring mass. *Science*, *364*(6445).

Iess, L., Rappaport, N. J., Jacobson, R. A., Racioppa, P., Stevenson, D. J., Tortora, P., Armstrong, J. W., & Asmar, S. W. (2010). Gravity field, shape, and moment of inertia of Titan. *science*, *327*(5971), 1367–1369.

Jaumann, R., Brown, R. H., Stephan, K., Barnes, J. W., Soderblom, L. A., Sotin, C., Le Mouélic, S., Clark, R. N., Soderblom, J., Buratti, B. J., et al. (2008). Fluvial erosion and post-erosional processes on Titan. *Icarus*, *197*(2), 526–538.

Kaula, W. M. (2013). *Theory of satellite geodesy: applications of satellites to geodesy*. Dover Publications.

Kopeikin, S. M., & Schäfer, G. (1999). Lorentz covariant theory of light propagation in gravitational fields of arbitrary-moving bodies. *Physical Review D*, *60*(12), 124002.

Lemoine, F. G., Goossens, S., Sabaka, T. J., Nicholas, J. B., Mazarico, E., Rowlands, D. D., Loomis, B. D., Chinn, D. S., Neumann, G. A., Smith, D. E., et al. (2014). GRGM900C: A degree 900 lunar gravity model from GRAIL primary and extended mission data. *Geophysical research letters*, *41*(10), 3382–3389.

Love, A. E. H. (1906). *A Treatise on the Mathematical Theory of Elasticity*. Cambridge University Press.

McCarthy, J. J., Rowton, S., Moore, D., Pavlis, D. E., Luthcke, S., & S., T. L. (2015). *GEODYN II System Description Volume 1* (tech. rep.). NASA GSFC.

Mitrovica, J. X., Davis, J. L., & Shapiro, I. I. (1994). A spectral formalism for computing three-dimensional deformations due to surface loads: 1. Theory. *Journal of Geophysical Research: Solid Earth*, *99*(B4), 7057–7073.

Montenbruck, O., & Gill, E. (2001). *Satellite Orbits: Models, Methods and Applications*. Springer.

Moyer, T. D. (2005). *Formulation for observed and computed values of Deep Space Network data types for navigation*. John Wiley & Sons.

O'Dea, A., & Bryant, S. (2015). *TRK-2-34 DSN Tracking System Data Archival Format* (tech. rep.). Jet Propulsion Laboratory, California Institute of Technology.

O'Neill, M. E. (2014). PCG: A family of simple fast space-efficient statistically good algorithms for random number generation. *ACM Transactions on Mathematical Software*.

Rappaport, N., Bertotti, B., Giampieri, G., & Anderson, J. (1997). Doppler Measurements of the Quadrupole Moments of Titan. *Icarus*, *126*(2), 313–323.

Schutz, B., Tapley, B., & Born, G. (2004). *Statistical orbit determination*. Elsevier.

Shapiro, I. I., Ash, M. E., Ingalls, R. P., Smith, W. B., Campbell, D. B., Dyce, R. B., Jurgens, R. F., & Pettengill, G. H. (1971). Fourth test of general relativity: new radar result. *Physical Review Letters*, *26*(18), 1132.

Stauch, J. R., Antreasian, P., Bordi, J., Criddle, K., Ionasescu, R., Jacobson, R., Jones, J., Meek, M. C., Roth, D., & Roundhill, I. (2005). Preparing for the Huygens Probe Mission, Cassini orbit determination results for the first and second targeted Titan encounters.

Stofan, E. R., Elachi, C., Lunine, J. I., Lorenz, R. D., Stiles, B., Mitchell, K., Ostro, S., Soderblom, L., Wood, C., Zebker, H., et al. (2007). The lakes of Titan. *Nature*, *445*(7123), 61–64.

Taylor, J., Sakamoto, L., & Wong, C. (2002). Cassini Orbiter/Huygens Probe Telecommunications, Descanso Design and Performance Summary Series.

Vallado, D. A. (2001). *Fundamentals of astrodynamics and applications* (Vol. 12). Springer Science & Business Media.

van Noort, B. (2021). The Gravity of Titan: Analysis of Cassini's Doppler Tracking Data and Solar Radiation Pressure.

Weischede, F., Gill, E., Montenbruck, O., & Floberghagen, R. (1999). Lunar prospector orbit determination and gravity field modeling based on Weilheim 3-way Doppler measurements. *J. Brazilian Soc. Mech. Sci*, *21*, 280–286.

Yung, Y. L., Allen, M., & Pinto, J. P. (1984). Photochemistry of the atmosphere of Titan: Comparison between model and observations. *Astrophysical Journal Supplement Series*, *55*(3), 465–506.